Professur für Höchstfrequenztechnik
Department of Electrical and Computer Engineering
Technical University of Munich

Predictive Quantization for Staggered Synthetic Aperture Radar

Experiments with Real Airborne F-SAR Data

Jakob Giez

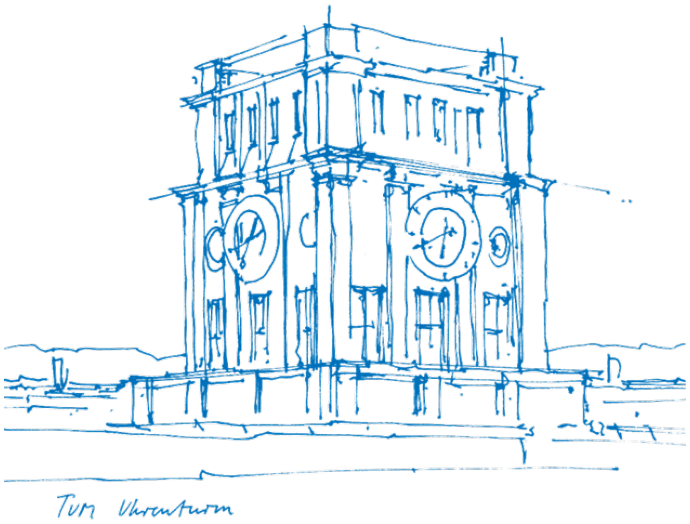

Predictive Quantization for Staggered Synthetic Aperture Radar

Experiments with Real Airborne F-SAR Data

Jakob Giez

Professur für Höchstfrequenztechnik
Department of Electrical and Computer Engineering
Technical University of Munich

Predictive Quantization for Staggered Synthetic Aperture Radar

Experiments with Real Airborne F-SAR Data

Jakob Giez

Thesis for the attainment of the academic degree

Master of Science (M.Sc.)

at the Department of Electrical and Computer Engineering of the Technical University of Munich.

Examiner:
Univ.-Prof. Dr.-Ing. Erwin Biebl

Supervisor:
Nicola Gollin, Michele Martone

Submitted:
Landsberg a. Lech, 30.09.2021

I hereby declare that this thesis is entirely the result of my own work except where otherwise indicated. I have only used the resources given in the list of references.

Landsberg a. Lech, 30.09.2021 Jakob Giez

Acknowledgments

This thesis represents the results of six months of research at the Microwave and Radar Institute of the German Aerospace Center (DLR) in Oberpfaffenhofen. I wanted to specially thank my supervisors Nicola Gollin and Michele Martone, who made this thesis possible by guiding me with their experience and spend their time to answer my questions. A special thank must also go to Rolf Scheiber, who assisted me in performing the final SAR focusing steps to produce the SAR images. I also wanted to thank the whole System Performance group, who always provided help when needed and created a nice working climate, despite the complicated Covid-19 situation.

Landsberg am Lech, September 2021
Jakob Giez

Abstract

Nowadays, there is a constant development of new synthetic aperture radar (SAR) systems and acquisition modes for present and next generation spaceborne SAR missions, which have to be capable of processing large bandwidths, multiple channels and polarizations, as well as imaging wide swaths on ground with high spatial resolution. An example for such a next generation system is the satellite SAR mission proposal Tandem-L, which was recently developed by the German Aerospace Center (DLR). The system comprises two twin SAR satellites operating at L band and is foreseen to acquire data in the so-called *Staggered SAR* mode, which allows for wide swath acquisitions covering the full range of possible observation angles, while maintaining high spatial resolutions. The large swaths, along with the fine resolution, can be realized by constantly imaging the target area with varying Pulse Repetition Intervals (PRI), which ultimately results in data gaps within the acquired raw data. During the processing phase, a gap-free SAR signal can then be reconstrutcted at a uniform sampling rate. In order to do so, a certain autocorrelation between neighbouring samples is necessary. The constant monitoring capabilities and the high data oversampling rate of this method lead to the generation of large data volumes that need to be stored on board and downlinked to the ground. This represents a challenging trade-off between the limited onboard resources in spaceborne system in terms of both computational power and storage memory. Therefore, this new acquisition method is only feasible if combined with an effective onboard signal quantization, which aims at providing high data reduction rates together with a satistfying image quality, while keeping the system complexity at a low level, in order to meet the requirements of the satellite SAR system. Furthermore, such a method for data reduction requires the ability to cope with the presence of blind gaps in the SAR raw data.

Predictive coding for data reduction on real SAR data, comprising its direct application to SAR raw data as well as range focused data, has been proposed by DLR as a possible quantization scheme to tackle the staggered SAR paradigm. Up to now, the achievable performance of such a quantization method, called *Dynamic Predictive - Block Adaptive Quantization*, has been only evaluated from a theoretical point of view. Its implementation and testing on real SAR data represents therefore a key aspect for consolidating its architecture and veryfing its potential.

In this thesis work, the performance of this new predictive quantization method is investigated for the first time with respect to real Staggered SAR data. The quantizer exploits the correlation between adjacent SAR samples using Linear Predictive Coding in combination with a state-of-the-art-quantizer for data reduction, based on block adaptive quantizaiton (BAQ). Since no spaceborne real SAR data, acquired in Staggered SAR mode, are avilable yet, the analyzed data set was generated from highly oversampled airborne SAR data, acquired by the DLR FSAR airborne SAR system, according to the Tandem-L system parameters. The results of the analysis confermed the theoretical prediction and proved the full functionality of the predictive quantizer for a spaceborne Tandem-L-like system, showing an additional data reduction of up to $20 - 25\%$ on Staggered SAR data, with respect to conventional quantization methods. Morevoer, thanks to the linear structure of the predictor, the computational effort of the new quantizer is increased only marginally, with respect to standard BAQ, making it an attactive solution for future SAR missions.

List of Symbols

List of constants

constant	explanation	value
c_0	speed of light in vacuum	$2.99792458 \cdot 10^8$ m/s
π	pi constant	3.14159265
k_B	Boltzmann constant	$1.38064852 \cdot 10^{-23}$ J/K

List of Mathematical Operators, Notations, Functions

constant	explanation
$*$	complex conjugate
$\circledast$	convolution operator
$\lvert \cdot \rvert$	absolute value
$\lvert\lvert \cdot \rvert\rvert$	euclidean norm
$\int$	integration operator
$\in$	element-of operator
$\sum$	summation operator
$\Im\cdot$	denoting imaginary part
$\Re\cdot$	denoting real part
$\cos(\cdot)$	cosine function
$\exp(\cdot)$	exponential function
$\mathbb{E}[\cdot]$	Expectation operator
$\mathscr{F}^{-1}(\cdot)$	inverse Fourrier transformation
$\log_x(\cdot)$	logarithmic function to the base of x
$\sin(\cdot)$	sinus function
$\mathrm{sinc}(\cdot)$	sinus cardinalis function

List of Latin Symbols

constant	unit	explanation
A		Attenuation of emitted signal
B_τ	1/s	chirp bandwidth
B_D	1/s	Doppler bandwidth
$B_\perp$	m	baseline between master and slave sensor
B_R	1/s	bandwidth of power spectral density function
C		bit rate-dependent constant for BAQ
$\mathcal{D}$		signal difference represented as random process
$\boldsymbol{C}$		covariance matrix for LPC
d_{az}		azimuth distance
d_i		decision intervals
d_{rg}		range distance
E		exponent for BAQ
$e[n]$		error term at the discrete time instance n for LPC
E_{max}		maximum exponent for BAQ

f	Hz	Doppler frequency
f_0	Hz	carrier frequency of chirp signal
f_q		transfer function for quantization
$f_D(t)$		time dependent Doppler shift
F_N		noise figure
$f_x(x)$		probability density function of x
G_p		antenna gain at p polatization (transmit)
G_P		coding gain
G_{proc}		processor gain
G_q		antenna gain at q polatization (receive)
$G(\Phi_{az})$		azimuth antenna pattern
$G(\Psi_a, \Psi_r)$		planar antenna pattern
h_s	m	sensor altitude
$\bar{I}$		intensity
$I_{n,ADC}$		real part of signal after ADC quantization
$I_{n,BAQ}$		real part of signal after BAQ quantization
$\bar{I}_n$		scaled real part of BAQ input value
j		imaginary constant in complex signal
$K_{I,i}$		Bit value of real sample part after BAQ quantization
$K_{Q,i}$		Bit value of imaginary sample part after BAQ quantization
K_s		radar gain term for calibration
k_τ		chirp rate
k_{tot}		Loss term
L_a	m	antenna length in azimuth direction
L_{BAQ}		BAQ block length
L_{chirp}		chirp length
L_s	m	radar footprint extension
M		Length of quantization alphabet
$M_{I,ADC,i}$		bit representation of real part after ADC quantization
M_{max}		maximum mantissa for BAQ
$M_{Q,ADC,i}$		bit representation of imaginary part after ADC quantization
N_b	bits/sample	Number of bits
n_{BAQ}	bits/sample	Number of bits for BAQ quantization
$n(t)$		time dependent noise contribution
P_q^r	W	received power at q polatization
P_q^t	W	transmitted power at q polatization
$p_q(q)$		probability density function of quantization error
$p_x(x)$		probability density function of input signal
PRI_{min}		minimum Pulse Repetition Interval
q		quantization error
$Q_{n,ADC}$		imaginary part of signal after ADC quantization
$Q_{n,BAQ}$		imaginary part of signal after BAQ quantization
$\bar{Q}_n$		scaled imaginary part of BAQ input value
$R(t)$	m	time dependent slant range
R_0	m	slant range
R_E	m	Earth radius
R_g	m	ground range
r_{clip}		reconstruction level for clipping value
r_k		reconstruction level
R_{S_1}	m	slant range master sensor
R_{S_2}	m	slant range slave sensor

$r(t)$		time dependent reflected signal for point target
s		input signal
$s(t)$		time dependent emitted signal
S_1		first sensor (master)
S_12		second sensor (slave)
$s[n]$		signal at discrete time instance n
$\hat{s}[n]$		reconstructed signal at discrete time instance n
$\tilde{s}[n]$		predicted signal at discrete time instance n
$s_a(t)$		azimuth reference function
s_{BAQ}		signal quantized by BAQ
$s_{BAQ,f}$		focused signal quantized by BAQ
$s_d[n]$		signal difference at discrete time instance n for DPCM and LPC
$\hat{s_d}[n]$		reconstructed prediction error at discrete time instance n for DP-BAQ
s_{DPBAQ}		signal quantized by DP-BAQ
$s_{DPBAQ,f}$		focused signal quantized by DP-BAQ
s_f		SAR focused signal
s_n		input sample
$s_{n,q}$		quantized sample
s_q		quantized signal
$s_{qd}[n]$		quantized prediction error at discrete time instance n for DP-BAQ
SNR		Signal to Noise Ratio of quantization process (DP-BAQ)
$SQNR_{dB}$		Signal to Quantization Noise Ratio in dB
$s_{staggered}$		input signal with staggered PRI
t	s	slow time (azimuth time)
t_{int}	s	integration time
T_r	℃	receiver Temperature
v_g	m/s	ground speed
V_{clip}		clipping range
v_s	m/s	sensor velocity
W	m	antenna length in range direction
W_g	m	radar swath width
$\mathcal{X}$		input signal represented as random process
$\mathcal{Y}$		predicted signal represented as random process

List of Greek Symbols

constant	**unit**	**explanation**
α		scaling factor
α_L	°	looking angle
α_n		scaling factor for discrete time instance n (DP-BAQ)
$\boldsymbol{\beta}$		vector with prediction weights for LPC
β_i		prediction weight for i-th preceding sample in LPC
$\chi(t)$		chirp after matched filtering
Δ		step size
$\delta_{a_{RAR}}$	m	azimuth resolution for Real Aperture Radar
δ_a	m	azimuth resolution for Synthetic Aperture Radar
$\Delta_{ac,min}$		minimum deviation between two autocorrelation values
Δ_{error}		error ratio
Δ_{Φ_n}		phase error for n-th sample
$\Delta\Phi_{int}$	°	interferometric phase

$\delta_{r_{rect}}$	m	range resolution for rectangular pulse
δ_r	m	range resolution for chirp pulse
Δ_r	m	travel path distance for InSAR
δ_{r_g}	m	ground range resolution for chirp pulse
Δ_{SQNR}		absolute gain
δ_t	s	signal delay at time instance t
γ		interferometric coherence
γ_{Az}		loss contribution of relative Doppler shift spectra
γ_{clip}		Signal-to-clipping ratio
γ_{Quant}		quantization coherence
γ_{Rg}		loss contribution of ambiguity decorrelation
γ_{SNR}		loss contribution of limited SNR
γ_{Temp}		loss contribution of temperature decorrelation
γ_{Vol}		loss contribution of volume decorrelation
λ	m	radar wavelength
μ_x		mean of input signal
Φ	°	azimuth angle
Φ_0	°	phase of chirp signal
$\Phi[j]$		Autocorrelation for discrete time signal
Φ_n	°	Phase of n-th sample
$\Phi_{n,q}$	°	Phase of n-th sample after quantization
Φ_s	°	scattering phase
Φ_{x_a,y_a}	°	phase of point a
Φ_{x_b,y_b}	°	phase of point b
Ψ_a	°	off-center angle in azimuth direction
$\Psi_{a,3dB}$	°	half power beamwidth angle in azimuth direction
Ψ_r	°	off-center angle in range direction
$\Psi_{r,3dB}$	°	half power beamwidth angle in range direction
ρ		autocorrelation
$\boldsymbol{\rho}$		vector with correlation values for LPC
ρ_τ		autocorrelation at time delay τ
σ_0		Radar cross section
σ_d		standard deviation of the prediction error
σ_d^2		variance of the prediction error
σ_e		standard deviation of the error term (LPC)
σ_e^2		variance of the error term (LPC)
σ_f		oversampling factor
σ_{inI}		standard deviation of real part of input signal
σ_{inI}^2		variance of real part of input signal
σ_{inQ}		standard deviation of imaginary part of input signal
σ_{inQ}^2		variance of imaginary part of input signal
σ_{pq}		Radar cross section for p and q polarization
σ_q		standard deviation of quantized signal
σ_q^2		variance of quantized signal
σ_x		standard deviation of input signal
σ_x^2		variance of input signal
σ_y		standard deviation of predicted signal
σ_y^2		variance of predicted signal
τ	s	fast time (range time)
τ_{new}	s	new time values for signal resampling
τ_p	s	pulse duration

Θ_i	°	local incidence angle
ξ_i		input intervals

List of Acronyms

constant	**explanation**
ADC	Analogue to Digital Converter
ARF	Azimuth Reference Function
BAQ	Block Adaptive Quantizer
DLR	Deutsches Zentrum für Luft und Raumfahrt (German Aerospace Center)
CLT	Central Limit Theorem
DP-BAQ	Dynamic Predictive - Block Adaptive Quantizer
DPCM	Differential Pulse Code Modulation
ESA	European Space Agency
HoA	Height of Ambiguity
I	In-phase component
InSAR	Interferometric SAR
LPC	Linear Predictive Coding
MSE	Mean Square Error
NESZ	Noise Equivalent Sigma Zero
PRF	Pulse Repetition Frequency
PRI	Pulse Repetition Interval
Q	Quadrature Component
RCS	Radar Cross Section
RAR	Real Aperture Radar
SAR	Synthetic Aperture Radar
SCORE	Scan on Receive
SNR	Signal to Noise Ratio
SQNR	Signal to Quantization Noise Ratio
TDL	Tandem-L

List of Figures

List of Tables

Contents

1 Introduction

Over the last decades, Synthetic Aperture Radar (SAR) has developed into a reliable remote sensing technique for Earth observation, due to to its high performing system parameters and the ability to install the respective antenna on different platforms like aircraft, or satellites. Especially the latter option provides a stable system orientation, which enables high resolution imaging and precise long term monitoring. Furthermore, SAR represents an active remote sensing technique, which allows imaging independent of weather and sunlight. Over the last years the performance of SAR systems has constantly increased, by using multiple polarization, high sampling rates, growing bandwidths and larger swath widths, all of these resulting in the acquisition of higher data volumes. Thus, methods for efficient onboard data reduction have gained great interest, especially since they define the final image quality and the required computational effort onboard.
As stated before, the high stability and weather independent operation of SAR provide the ideal conditions for long term applications, like ocean surface current predictions, or deforestation, biomass and glacier monitoring. The German Aerospace Centre (DLR) is investigating on new spaceborne SAR systems for these applications, which provide high image resolution and wide swaths. An example is the actual proposal for the innovative single-pass interferometric Tandem-L system. The system is operated in L-band and will be equipped with new acquisition modes, like *Staggered SAR* which exploits the wide bandwidth and high Pulse Repetition Frequencies (PRF) of this system in order to generate high resolving images, while maintaining large swath widths. This can be achieved by constantly monitoring the target with pulses of varying length over a wide range of observation angles. Due to the fact, that the sensors are not able to send and receive at the same time, the raw data contains so called blind ranges, which require a sufficient oversampling in azimuth direction in order to reconstruct a complete data set. Due to this oversampling, the method results in a huge amount of data, which requires effective onboard quantization, especially since storage space is rather limited in spaceborne systems. There have been several approaches for data reduction, some of them relying on complex algorithms, which proved high effectiveness in the reduction rate. Since energy in spaceborne SAR systems is limited, those techniques did not prove to be applicable for a real spaceborne implementation. In order to serve the problem, DLR developed a new technique, which is combining Linear Predictive Coding (LPC) with a state-of-the-art quantization method. This method exploits the autocorrelation of the SAR signal in order to generate a signal of reduced dynamic range. The reduced dynamic can then be exploited by a quantizer to represent the signal in a smaller signal space, while maintaining a good image quality. Up to now, all simulations of this technique were based on synthetic SAR data and demonstrated data reduction of up to $10 - 15\%$ while maintaining the same image quality, compared to conventional state of the art quantizer. Being only simulations of synthetic data, these tests were not able to provide information on special scenarios in real SAR images, like the effects of the quantization on low backscatter areas, high variations in the signal amplitude, or possible errors, which are only visible after full SAR focusing. This thesis work will investigate the performance of this new method on real SAR data with a focus on the Staggered SAR acquisition method for a Tandem-L-like scenario. All data sets analyzed are based on real SAR images acquired by the airborne F-SAR system of DLR, which has been designed for testing new SAR acquisition methods due to highly oversampled data and the capability to record at different frequencies and polarizations. The quantization method is tested for different preliminary scenarios, including the general performance, the performance on F-SAR data and the performance on data for a spaceborne SAR system. The final analysis is then conducted for spaceborne Staggered SAR and takes time variant pulse rates and gaps into account. All results are analyzed in terms of image quality for different data rates and compared to conventional state of

the art quantization methods.
In chapter 2 the thesis will introduce to the theoretical background of SAR imaging, including the SAR geometry, SAR image formation, as well as SAR focusing and important radar parameters. The chapter also provides information about possible error sources, the calibration of the SAR system and SAR acquisition with multiple polarizations. Furthermore, the *Staggered SAR* acquisition technique is introduced. The following chapter 3 will present the general functionality of quantization, as well as common error sources and most important parameters for performance evaluation. A state of the art quantizer will be explained and finally the new quantization technique, based on LPC will be described, as well as their implementation on Staggered SAR data. The airborne F-SAR system, which was used for generating the Staggered SAR data set, is introduced in chapter 4. The following chapter 5 will show the results of the previously mentioned tests with real SAR data in terms of image quality. Furthermore, those results are compared to the quantizer in chapter 3, which was described in chapter 3. In the last chapter 6, the results and observations of this thesis will be summarized and possible further investigation steps will be discussed.

2 Theoretical Background

2.1 Synthetic Aperture Radar

Sensor	Lifetime	Frequency Band	Institution, Country
Seasat	1978	L	NASA/JPL, USA
SIR-A/B	1981/1984	L	NASA/JPL, USA
ERS-1/2	1991-2000 1995-2011	C	ESA, Europe
JERS-1	1992-1998	L	JAXA, Japan
SIR-C/X-SAR	1994	L/C/X	NASA/JPL, USA DLR, Germany ASI, Italy
RADARSAT-1 RADARSAT-2	1995-2013 2007-today	C	CSA, CANADA
SRTM	2000	C/X	NASA/JPL, USA DLR, Germany ASI, Italy
ENVISAT/ASAR	2002-2012	C	ESA, Europe
ALOS/PalSAR	2006-2011	L	JAXA, Japan
TerraSAR-X TanDEM-X	2007-today 2010-today	X	DLR/Airbus, Germany
COSMO-SkyMed-1/4	2007. . . 2010-today	X	ASI/Italian MoD, Italy
RISAT-1	2012-today	C	ISRO, India
HJ-1C	2012-today	S	CRESDA/CAST/ NRSCC , China
Kompsat-5	2013-today	X	KARI, South Korea
Sentinel-1a/1b	2014/2016-today	C	ESA, Europe
ALOS-2	2014-today	L	JAXA, Japan
PAZ	2018-today	X	CDTI, Spain
NovaSAR-1	2018-today	S	SSTL/Airbus/UKSA, UK
SAOCOM-1a SAOCOM-1b	2018-today 2020-today	L	CONAE, Argentina
ICEYE Constellation	2018/2019-today	X	Iceye Oy, Finland
RCM	2019-today	C	CSA, Canada

Table 2.1 Past and current satellite based SAR missions with corresponding time of operation, frequency band and the operating institution.

Synthetic Aperture Radar (SAR) is a widely used remote sensing technology for Earth observation, which comes with a variety of operational modes and application fields. A SAR antenna can

be mounted on spaceborne and airborne vehicles and be operated at different microwave frequency bands, e.g. X and L band, which correspond to wavelengths of $\lambda_X \approx 3\text{cm}$ and $\lambda_L \approx 23\text{cm}$. To overcome the physical limitations of a Real Aperture Radar (RAR) in terms of resolution and swath width, it exploits the constant movement of the mounting platform to enlarge its antenna by creating a synthetic aperture. With a proper selection of the sampling rate and time of aperture, a SAR system is capable of imaging wide areas at fine resolutions without the need for a physical long antenna. These properties, alongside with its capability of monitoring independently from weather and sunlight, makes it ideal for a variety of applications, like oceanography, cartography, soil moisture estimation, forest parameters assessment, and digital elevation model (DEM) generation with interferometric methods. A list of current SAR missions can be found in Table 2.1

This chapters will briefly introduce in the basic principles of SAR geometry, image formation and imaging modes, as well as radiometric and geometric distortions [26], [27], [3], [4], [5], [29].

2.1.1 SAR Geometry

The reference SAR geometry for air- and spaceborne SAR can be seen in Figure 2.1. The SAR antenna moves along the radar track in the azimuth direction with velocity v_s at an altitude h_s over the nadir-track, which describes the projection of the flight track on the surface. In a general SAR acquisition model, the antenna emits a pulsed radar signal perpendicular to the azimuth direction, which is called range direction. The area on ground, which is irradiated by the radar signal is called antenna footprint, whose dimensions represent two key parameter of a SAR system and are known as the swath width W_g and the azimuth footprint extension L_s, where

$$W_g = \frac{\lambda R_0}{W \cos \Theta_i} \quad \text{and} \quad L_s = \frac{\lambda R_0}{L_a} \ . \tag{2.1}$$

In the above equation L_a describes the length of the antenna in azimuth direction, W the corresponding antenna dimension in range, Θ_i the incidence angle on ground and λ the radar wavelength. The last parameter R_0 describes the shortest distance (i.e. at zero Doppler) between the emitter and the target on ground and is called *slant range*, whereas the corresponding projection on

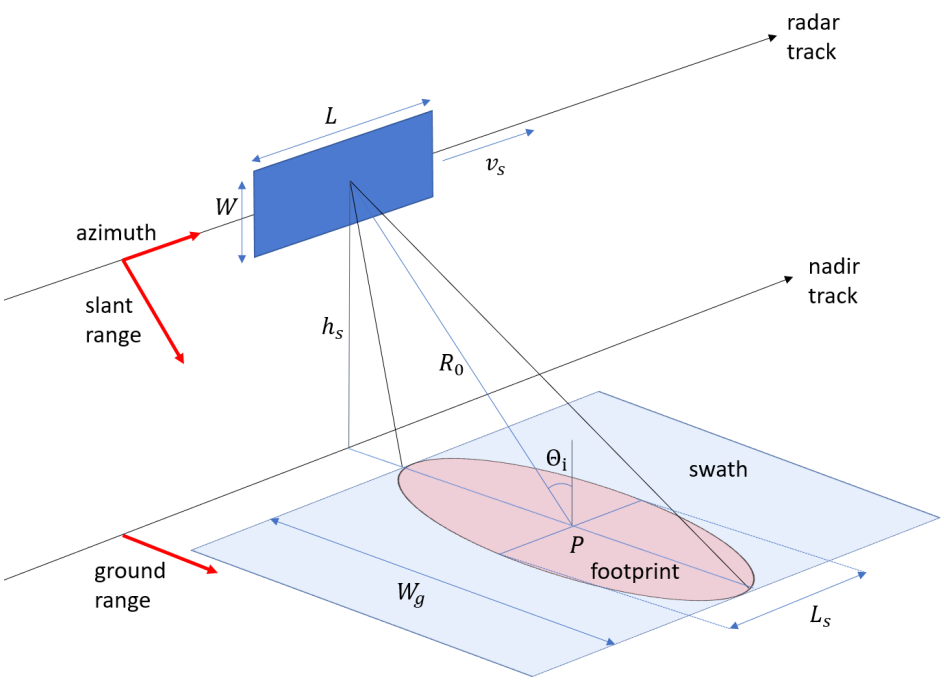

Figure 2.1 SAR geometry.

ground originating from the nadir track is called *ground range*. The blue area in Figure 2.1 describes the total area covered by the antenna footprint over the full acquisition time and is called *swath*. SAR imaging is an active acquisition method, which means that the antenna emits electromagnetic pulses directed to the target area on ground. The radar wave interacts with the targets illuminated within the antenna footprint and a fraction of its power is reflected back toward the SAR sensor. After each transmission the antenna receives the backscattered signal at a delay δ_t

$$\delta t = \frac{2 \cdot R_0}{c_0}, \tag{2.2}$$

being c_0 the speed of light in free space. Moreover, SAR is a coherence acquisition method in the sense that the sensor tracks the echos both in amplitude and phase, acquiring information about the footprints physical and dielectric properties, like distance and reflectivity. Each illuminated target in the antenna footprint reflects the signal of the radar beam, which can be tracked to retrieve information on the distance to each scatterer. Since the antenna has different transmission and reception properties depending on the angle of the emitted and incoming signal, the signal needs to be weighted with the antenna pattern during transmission and reception. The antenna pattern defines the angular distribution of the emitted power by the antenna and can be described for a planar antenna as

$$G(\Psi_a, \Psi_r) = \mathrm{sinc}^2\left(\frac{L_a}{\lambda}\Psi_a\right)\mathrm{sinc}^2\left(\frac{W}{\lambda}\Psi_r\right). \tag{2.3}$$

with Ψ_a describing the off-center azimuth angle and Ψ_r the off-center angle in range direction. In the upper equation the sinc function describes the typical signal response of a planar antenna and is defined as

$$\mathrm{sinc}(x) = \frac{\sin(x)}{x}. \tag{2.4}$$

The antenna pattern equation appears in (2.3) in squared form, since the antenna pattern is considering both, the transmission and reception of the signal.
To achieve the best attainable results, the antenna footprint is normally kept within the main lobe of the antenna pattern, or half power beam width, which can be approximated for a sinc^2 pattern in terms of the corresponding angles in elevation and azimuth dimension, ($\Psi_{r,3dB}$ and $\Psi_{a,3dB}$) by

$$\begin{aligned} \Psi_{r,3dB} &\approx 0.886\tfrac{\lambda}{W}, \\ \Psi_{a,3dB} &\approx 0.886\tfrac{\lambda}{L_a}. \end{aligned} \tag{2.5}$$

For a proper weighting of the transmitted and received SAR signal, precise knowledge about the *local incidence angle* Θ_i is required. The local incidence angle is defined as the angle between the slant range vector and the vector perpendicular to the surface where the radar beam hits the target on ground. In the flat earth model of Figure 2.1 this angle was assumed to be equal to the *looking angle* α_L, which corresponds to the angle between the slant range and the closest connection between sensor and ground. This assumption holds for most airborne systems, since the range distances are small enough to neglect the Earths curvature. For a spaceborne SAR in contrary, this simplification does not hold any more and the angles differ from each other, which can be seen in Figure 2.2.
As a consequence of the the change in the looking angle estimation, a curved earth model also influences the calculation of the azimuth angle for the moving sensor, which pictured in Figure 2.3. The following steps describe the calculation steps necessary to acquire the correct azimuth angle in a curved Earth model.
While the signal travels from the antenna to the ground and back, the satellite will have moved by a distance $d = v_s t$. The satellite, however, moves on ground at speed v_g, which is defined by

$$v_g \cong v_s \frac{R_E}{R_E + h_s}. \tag{2.6}$$

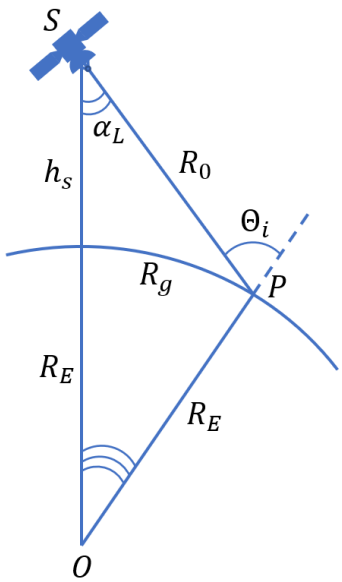

Figure 2.2 SAR geometry using a spherical model for a satellite S and a point scatterer P. The Earth center is labeled as O.

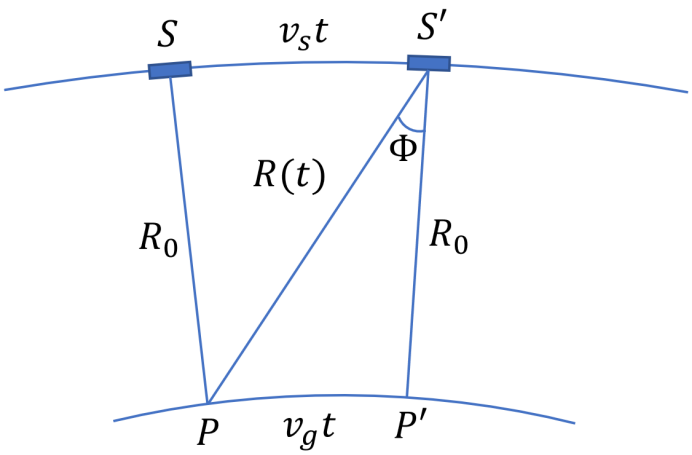

Figure 2.3 SAR geometry using a spherical model for a satellite S, moving on its radar track and a point scatterer P.

The slant range between antenna and point target can be calculated from

$$R(t) \cong \sqrt{R_0^2 + (v_r t)^2} \cong R_0 + \frac{(v_r t)^2}{2R_0}, \tag{2.7}$$

with v_r defining the relative movement between ground and satellite speed as the geometric mean

$$v_r = \sqrt{v_s v_g}. \tag{2.8}$$

Using the ground speed v_g one can calculate the azimuth angle Φ at time t as

$$\tan \Phi = \frac{v_g t}{R_0}. \tag{2.9}$$

2.1.2 SAR Image Formation

A SAR sensor images the swath on ground by repeatedly sending pulses to the target area, while travelling along azimuth direction. The received echoes are saved in a two dimensional grid called *raw data matrix*, which is mapped by the pulse number and the time delay, corresponding to azimuth and slant range. Each grid point contains the echoes reflected by many scatterers on ground within the illuminated footprint, forming a noisy superimposition, which can be modeled as complex zero-mean Gaussian stationary and independent process for the In-phase (I) and Quadrature (Q) component. While the sensor moves along the azimuth dimension, it sends the radar pulses at a certain Pulse Repetition Frequency (PRF), which is usually set for spaceborne SAR at a few thousand Hertz. During each Pulse Repetition Interval (PRI), which is the inverse of the PRF, the SAR sensor transmits and receives the signal and the reflected echoes.
The time in azimuth direction is usually known as the *slow* time t in SAR geometry, since the SAR observation usually takes place over several seconds, while the range time on the other hand is called *fast* time τ due to sampling rates in the millisecond domain and usual range sampling times in the order of nanoseconds. As mentioned earlier, the received echo gives information about the geometric and radiometric properties of the observed area. The information can be obtained by measuring phase and amplitude of the signal. The corresponding values of the amplitude and phase at the time instance t can be calculated from $R(t)$ (2.7) and Φ (2.9).
The SAR raw data need to be properly converted into interpretable information to be exploited for further applications. In the first step of the data processing, the received signal is amplified, transferred into baseband and discretized in range and time. Consequently, the time discrete raw data is quantized on board and downlinked from the satellite to the ground. After reception, the raw data matrix is reconstructed and focused using matched filters, which are further described in the following sections and are displayed for a general overview through the processing steps in Figure 2.4. Subsequent to the SAR focusing, in a final step of the SAR image formation the acquired data needs to be georeferenced to an exact location on Earth. In addition to the the processing steps necessary

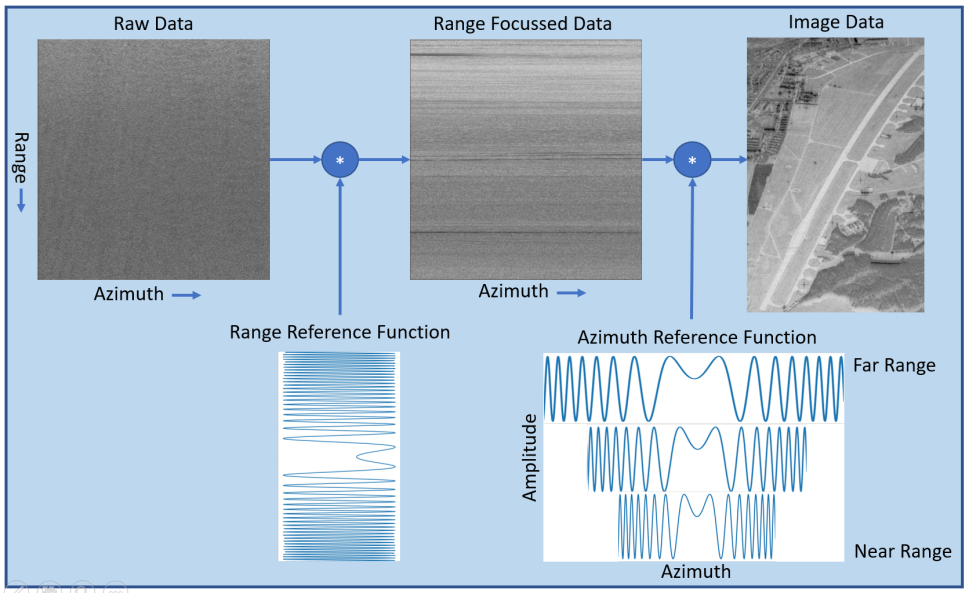

Figure 2.4 SAR image formation steps with real F-SAR data.

to create a usable SAR image, the system needs to be calibrated and corrected for deviations [6] in order to keep the received data at a high level of precision.

Range Focusing

The first step in the processing of the received data is the reconstruction of the information in range direction, which is also called *range focusing*. The reflected signal $r(t)$ from a point-like target on ground can be modeled as a phase-shifted, delayed, and attenuated version of the emitted signal $s(t)$ with a noise contribution $n(t)$

$$r(t) = As\left(t - \frac{2R_0}{c_0}\right)\exp\left(-j\frac{4\pi R_0}{\lambda}\right) + n(t). \tag{2.10}$$

In the above equation, A describes the attenuation of the emitted signal and j is the imaginary constant for its complex part. When looking at the raw SAR data in Figure 2.4, it becomes apparent, that the reflected signal needs to be further processed and corrected for a proper extraction of the information. This processing step is called SAR focusing and is accomplished, by filtering each range line with its "matched filter" $h(t)$. The matched filter represents the optimal filter which maximizes the Signal-to-Noise Ratio (SNR) and is expressed as the complex conjugate '*' of the transmitted signal [3], [27]

$$h(t) = s^*(-t). \tag{2.11}$$

Filtering a SAR signal is normally done by a convolution of the echo with the corresponding matched filter, which is defined for a general convolution process $\circledast$ as

$$r \circledast h = \int_{-\infty}^{+\infty} r(\tau)h(t-\tau)d\tau \tag{2.12}$$

To save resources and achieve a better performance, the signal is converted in the frequency domain by using a Fourier Transformation (FT), which simplifies the convolution to a multiplication.
An important factor in the SAR image quality is the range resolution, describing the minimum distance for scatterers to be distinguishable. For a rectangular pulse of duration τ_p the range resolution can be simply described as

$$\delta_{r_{rect}} = \frac{c_0\tau_p}{2}. \tag{2.13}$$

By analyzing (2.13) it gets clear, that the resolution improves with a shorter pulse length, which, on the other hand, degrades the SNR, due to the smaller energy of the emitted signal. To solve this problem, conventional SAR systems emit a linear frequency shifted signal, which is called *chirp* and can be modelled as

$$g(t) = \cos\left[\Phi_0 + s\pi\left(f_0 t + \frac{k_\tau t^2}{2}\right)\right] + j \cdot \sin\left[\Phi_0 + s\pi\left(f_0 t + \frac{k_\tau t^2}{2}\right)\right]. \tag{2.14}$$

In the upper equation, f_0 and Φ_0 describe the carrier frequency and phase of the signal. The factor k_τ describes the chirp rate, which defines the linear variation of the chirps frequency over time by $f_i = k_\tau t$ and the chirps Bandwidth $B_\tau = k_\tau \tau$. When applying the matched filter to a chirp signal the output can be expected to have the form of a sinc function and is defined as

$$\chi(t) = \mathrm{sinc}\left(\frac{2B_\tau}{c_0}R\right), \tag{2.15}$$

with a minimal slant range resolution of

$$\delta_r = \frac{c_0}{2B_\tau}. \tag{2.16}$$

Because of the inverse proportionality to the chirps bandwidth, it becomes clear, that the resolution of a chirp signal increases by using a longer chirp duration, which also ensures a higher SNR. While

the slant range resolution is completely independent of geometrical parameters, the ground range resolution is defined as

$$\delta_{r_g} = \frac{\delta_r}{\sin(\Theta_i)}. \tag{2.17}$$

This plays an important role in the processing of airborne SAR data, where the incidence angle Θ_i changes over multiple tens of degree in the swath due to the smaller sensor altitude.

Azimuth Focusing

The focusing in the azimuth dimension is done in the same way as in the range dimension. The signal is filtered in azimuth dimension by convolving it with its matched filter. The expected response of a point scatterer on ground is called the Azimuth Reference Function (ARF) and is defined as [2]

$$s_a(t) = A\sqrt{\sigma_0}e^{i\Phi_s}e^{-\frac{4\pi}{\lambda}R(t)}. \tag{2.18}$$

In the above equation σ_0 represents the Radar Cross Section (RCS), Φ_s the scattering phase and $R(t)$ the slant range defined in (2.7). In (2.18) the term $-\frac{4\pi}{\lambda}R(t)$ identifies the azimuth phase history, describing the effect of the changing range distance on the phase. As for the range dimension, the resolution in the azimuth domain represents a key parameter of the SAR system. In a Real Aperture Radar (RAR) the resolution corresponds to the azimuth antenna footprint and is defined as

$$\delta_{a_{RAR}} = L_s = \frac{\lambda R_0}{L_a}. \tag{2.19}$$

For typical SAR systems $\delta_{a_{RAR}}$ ranges from several tens of meters up to kilometers, and is therefore rather limited. As presented in (2.19) the only options to improve the azimuth resolution are to minimize the distance to the target, use a higher frequency, or increase the antenna length. Especially for spaceborne systems, those parameters can be hardly changed after launch. SAR provides a solution to those restrictions by virtually elongating the antenna length. By exploiting the systems stable and constant movement and, it becomes possible to observe the target in several consecutive pulses, as pictured in Figure 2.5, which can then be combined to get a finer resolution. A non-moving target P is staying in the radar beam for the time

$$t_{int} = \frac{L_s}{v_s} = \frac{\lambda R_0}{L_a v_s}, \tag{2.20}$$

which is known as the integration time t_{int}. Hence, the length of the virtual antenna corresponds to the length of the track, that the SAR sensor travels during the integration time. Each scatterer from a point target on ground returns a version of the originally emitted signal, translated in frequency with a Doppler frequency shift according to the targets azimuth angle. This Doppler shift can be derived, and under the small angle assumption, further simplified to

$$f_D(t) = \frac{2v_s \sin\left(\Psi(t)\right)}{\lambda} \cong \frac{2v_s a(t)}{\lambda R_0} = -\frac{2v_s^2}{\lambda R_0}t. \tag{2.21}$$

The Doppler shift resolution δf_D of the system is equal to the inverse of the integration time in (2.20). By substituting (2.20) into (2.21) the azimuth resolution can be finally expressed as

$$\delta_a = \frac{L_a}{2}. \tag{2.22}$$

From the above equation it becomes clear, that smaller antennas achieve a finer azimuth resolution, thanks to the linear dependency on the physical antenna length. Furthermore, the resolution is independent of other geometrical parameters like the range distance or the azimuth angle. The Doppler bandwidth of the system can be defined as in (2.16), by taking the reciprocal of the time it

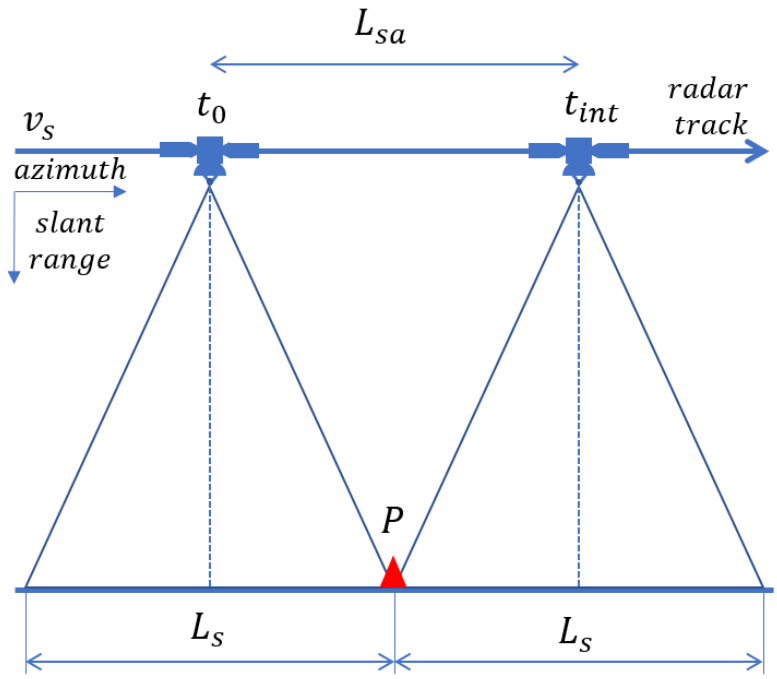

Figure 2.5 Synthetic aperture L_{sa} and antenna footprint L_s of the same length.

takes the sensor to travel through a resolution cell, which can be also expressed by the Doppler rate k_D

$$B_D = \frac{v_s}{\delta_a} = |k_D| t_{int} = \frac{2v_s}{L_a}. \tag{2.23}$$

This leads to an alternative definition of the azimuth resolution as

$$\delta_a = \frac{v_s}{B_D}. \tag{2.24}$$

By analyzing the above equations, it becomes clear, that the azimuth resolution improves for higher integration times. Nevertheless, when designing a SAR system the well known Shannon sampling theorem must be met to avoid the increase of azimuth ambiguities. When selecting the sampling rate in the azimuth dimension, which corresponds to the systems PRF, each PRI has to be small enough to meet the maximum attainable azimuth resolution. Those terms lead to the restrictions of

$$PRF \geq B_D \quad \text{or} \quad v_s \cdot PRI \leq \tfrac{L_a}{2}. \tag{2.25}$$

In order to fulfill the requirements of those constraints, the receive echo window has to be held short to enable a high sampling rate. This, however, implies that a shorter swath width is achieved by the system. Consequently, the design of a SAR system has to always considered a trade of between a large swath width and a sufficiently fine azimuth resolution. During the last years there have been several developments to overcome those restrictions, like multichannel SAR, Scan on Receive (SCORE), or Staggered SAR [7], [17], [8]. The latter will also be further explained in the upcoming sections, since an approach for data volume reduction for staggered SAR systems is investigated in this thesis work.

2.1.3 SAR Imaging Modes

Thanks to its capability to have a non-fixed synthetic antenna and the possibility of adjusting the antenna pattern during the data take, SAR comes with a variety of operational modes. Each mode

has its own advantages and can be selected to address the specific goals of the mission. They provide the possibility to generate high precision images of small regions, or, if needed, a wide swath width to cover a bigger area, when the resolution is not the highest priority. In the following, the three most common modes are introduced:

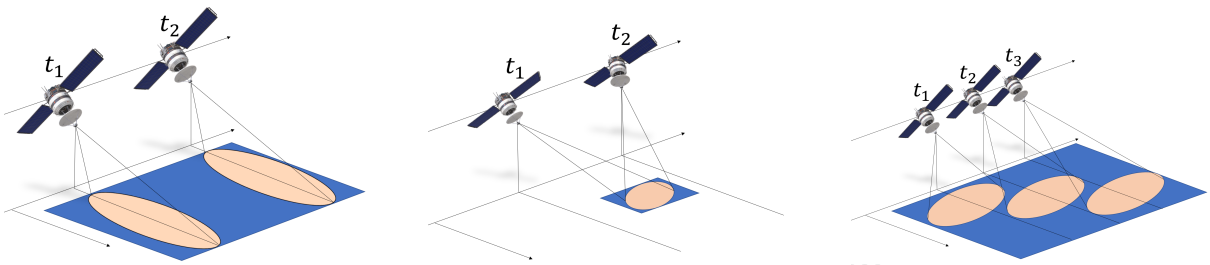

(a) Stripmap mode **(b)** Spotlight mode **(c)** Scan-SAR mode

Figure 2.6 SAR Imaging modes

- **Stripmap:**The formulas and figures presented so far were all referring to the standard stripmap mode, which is shown in Figure 2.6a. When operating in stripmap, the SAR antenna is set to a fixed elevation angle and illuminates one single swath. Because of the constant imaging of the area along the swath, this imaging mode is known as a continuous observation mode, meaning that the observation has theoretically no limit in azimuth direction.

- **Spotlight:** In Spotlight mode (Figure 2.6b), the sensor achieves finer azimuth resolution by steering the antenna pattern along the azimuth angle to target a fixed area over the image period. The finer azimuth dimension comes at the cost of a reduced swath width of a few kilometers. In contrast to the other two operation modes, spotlight represents the only *non-continuous* mode in this list as the azimuth scene extension is limited by the antenna steering operation.

- **ScanSAR:** In ScanSAR (Figure 2.6c) mode, the antenna cyclically varies its pattern over the elevation angle, i.e. over the slant range. For each angle, the sensor bursts a shorter set of radar pulses down to the target. This method allows for a much larger swath width after fully processing of the acquired data. The swath usually achieves several hundreds of kilometers and results in a degraded azimuth resolution. This method is also known as continuous observation mode.

2.2 Radar Parameters

SAR is characterized by a number of parameters, which have to be considered during the processing of the radar signal and for properly calibrating the system. Those parameters concern the radiometric as well as geometric properties of the system. The most significant parameters and processing steps, which are needed for the understanding of this thesis work, are addressed in the upcoming sections.

2.2.1 Radar backscatter and speckle

The recorded backscatter of a SAR image resolution cell always consists of the coherent contribution of many targets on ground. The scatterers can be classified in two main types, “point scatterers” and “distributed scatterers”. The first represents the dominant energy contributor of a single resolution cell, which means that most of the reflected energy is comming from this target. The reflected energy

of a point target illuminated by a radar wave at polarization q can be modeled by the point target radar equation

$$P_q^r = \frac{P_q^t G_p G_q \lambda^2}{(4\pi)^3 R^4} \sigma_{pq}. \tag{2.26}$$

P_q^t hereby denotes the transmitted power at polarization q, p represents the polarization used by the radar system in transmission, G_p and G_q the antenna gain in transmission and reception, and σ_{pq} the antenna cross-section, defining the ratio between the actual reflected intensity at the target and the intensity of the emitted signal that reaches the target.

Distributed targets, on the other hand, represent the case where non-dominant scatterers contributing all in the same way to the signal intensity of a resolution cell. Due to the Central-Limit Theorem (CLT) they can be modeled as Gaussian random variables with a probability density function of

$$f_x(x) = \frac{1}{\pi \bar{I}} \exp\left(\frac{Re(x)^2 + Im(x)^2}{\bar{I}}\right). \tag{2.27}$$

In the above equation $\bar{I}$ describes the Intensity of the complex signal $f_x(x)$, while the imaginary and real part are normally assumed to be uncorrelated, allowing the magnitude and phase to be independent from each other. Since a single resolution cell always contains multiple scatters, the cells amplitude and phase can be seen as the coherent summation of all of them. Due to the averaging of the amplitudes and phases, the single reflections are no longer distinguishable and significant variations can occur for neighbouring cells. This spatial fluctuation of the resolution cells is called *speckle* and mostly appears in areas with a surface roughness comparable to the radar wavelength. Speckle is also naturally reduced for systems with high resolution, due to low numbers of scatterers per cell. In order to get a more informative SAR image, speckle must be sufficiently reduced. This, however, can not be simply done by increasing the signal intensity, since its variance increases with the transmitted power [26]. An efficient method to reduce speckle in the radar image is called *multi-looking* [27]. It can be described as the averaging of the amplitudes and phases of pixels in the same region, which leads to a decrease of the backscatter standard deviation of the backscatter and consequently to an improvement of the radiometric resolution and interpretability, at the cost of a decreased image resolution. The multi-looking process can be carried out in different domains:

- *Spatial domain*: Contiguous pixels in a fixed area are averaged together.
- *Time domain*: Splitting of the synthetic aperture into several smaller sub apertures, resulting into separately processed images of the same area with lower resolution.
- *Frequency domain*: Like in the time approach, the Doppler-bandwidth is separated in several sub-bands and separately processed.

2.2.2 Noise Equivalent Sigma Zero

The Noise Equivalent Sigma Zero (NESZ) is a key parameter for determining the performance of a SAR system and describes the systems sensitivity (i.e. noise floor). The NESZ can be calculated as the backscatter coefficient σ_0 for a Signal-to-Noise Ratio (SNR) equal to one

$$SNR = \frac{\sigma_0}{NESZ} = 1. \tag{2.28}$$

The value itself describes the systems noise and is composed of many contributers, which are defined in

$$NESZ_{pq} = \frac{4^4 \pi^3 R^3 v_s \sin(\eta) k_B T_r B_{rg} F_N L_{tot}}{P_p^t G_q G_p \lambda^3 c_0 \tau_p PRF}, \tag{2.29}$$

for a pq-polarized SAR signal. In the above equation k_B represents the Boltzmann constant, T_r the receiver temperature describing the thermal noise, F_N is the noise figure, G_p and G_q describe the transmit and receive antenna gains and L_{tot} stands for all remaining loss factors like system, atmosphere and data quantization. During performance analysis, the NESZ is normally measured in regions with low backscatter, like seas, or calm water in general, where almost the complete signal is reflected in specular direction and only a negligible power fraction of the emitted pulse is reflected back to the sensor. Thus, the signal can be assumed to be below the system noise [3], [22].

2.2.3 Absolute Calibration

After focusing the data from the received radar echoes in range and azimuth, the resulting SAR image represents the radar reflectivity of the acquired area. For a proper interpretation, the data need to be calibrated. Calibration of a SAR system can be divided into two main tasks: Firstly the internal calibration, which is done by compensating for the radar gain term K_s i.e. setting it to 1[6]

$$K_s = \frac{P_p^t G_q G_p \lambda^2 G_q^e G_{proc}}{(4\pi)^3 R^4 L_s L_a}. \tag{2.30}$$

K_s describes all possible error terms like the antenna gain in transmit and receive G_p and G_q, the transmit power P_p^t, the processor Gain G_{proc}, the electronic gain in the radar receiver G_q^e, possible attenuation by the atmosphere L_a and a general system loss term L_s. The parameters R and λ represent the range delay to the target and signal wavelength. The compensation term is calculated and adjusted pre- and in-flight by multiple internal feedback loops. Secondly, the external calibration, which is required since not all parameters can be sufficiently exact determined by internal calibration. The calibration is done by targeting reflectors with known scattering characteristics, like corner reflectors or specially designed transponders to compensate for the errors and is further detailed explained in [6].

2.2.4 Geometric Distortions and Geocoding

In a last step the image needs to be georeferenced. Hereby, the image is geographically mapped, by using points of precisely known location in the scene. Nevertheless, due to the transformation of three-dimensional SAR data into a two-dimensional space, a few geometrical distortions can occur, typically in scenarios, where big height differences and slopes are present in the scene under observation. The main distortions are shown in Figure 2.7 and can be summarized under consideration of the slope α and the elevation angle Θ_e:

- *Shadowing*: Shadowing represents the effect of areas hidden from the Radar view, due to higher terrain in front of it. It appears in regions with $\alpha < 0$ and $\frac{\pi}{2} - |\alpha| < \Theta_e$.An example can be seen in Figure 2.7a, where the area CB is shadowed by C.

- *Layover*: A layover is observed if the the terrain slope alpha is bigger than the elevation angle $(\alpha > \Theta_e)$. The SAR receiver observes a point inversion of targets on the bottom side of the elevated area versus a target on top of it, as it is shown in Figure 2.7b.

- *Foreshortening*: Appears for a positive slope $(\alpha > 0)$ facing towards the transmitter. The SAR antenna observes a falsely reduced distance between targets in front and on top of the elevated region versus targets behind the elevated region (Figure 2.7c).

These geometrical distortions can be minimized by selecting a proper elevation angle for the observed area. Typically, incidence angles between 30° and 50° offer a good compromise between the occurrence of geometric distortions and resulting SNR. Furthermore, foreshortening can be corrected during data processing, and specifically during geocoding.

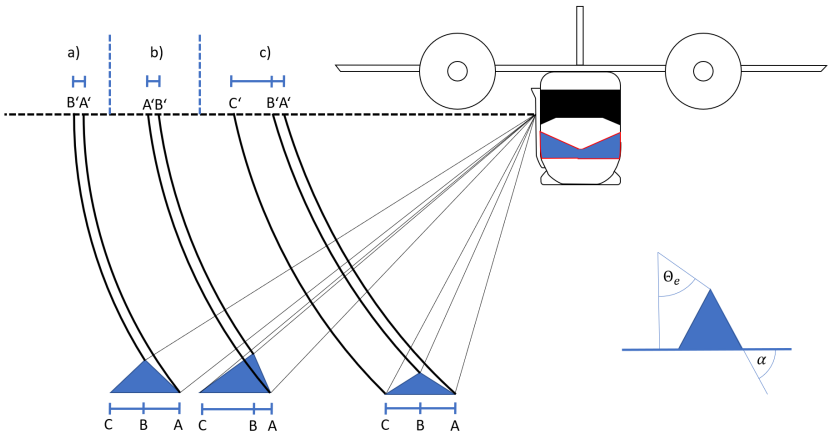

Figure 2.7 Geometric Distortions: a) Shadowing, b) Layover, c) Foreshortening.

2.3 Interferometric SAR (InSAR)

As already mentioned a SAR system retrieves its information by analyzing the backscattered signal and its scattering properties. Interferometric SAR (InSAR) expands this acquisition method by considering measurements from different receivers, which are separated in time and space. These measurements are usually gained from the phase and can be separated in two main information sources, the *propagation phase* and the *backscattered phase*. The first type was already mentioned earlier and gives information about the distance between sensor and the scatterer on ground. The latter, on the other hand, gives information about the contribution of phase difference due to the properties of the observed area. Those measurements can be used to retrieve information about the geophysical properties of the surface, like elevation models (i.e. Digital Elevation Models (DEMs)), surface movements (i.e. glacier movements or ocean currents) and ground deformations, and can reach a precision up to a few centimetres, or even millimeters.

2.3.1 InSAR Acquisition Modes

Since InSAR represents a multi-static, or at least bi-static acquisition technique, the sensors for the data acquisition are separated in time and space. The acquisition modes separated in time can be differentiated into two modes:

- **single pass mode:** The time lag between the two receiving antennas is equal to zero, which is the case if the satellite is featured with two, or more receiving antennas.
- **repeat pass mode:** The time lag between both antennas is nor equal to zero, i.e. if the sensor has to revisit the observed area at a later time instance.

The different operation modes for the separation in space can be combined with the time modes and are listed below:

- **along track interferometry:** The sensors are aligned along track for the data acquisition. This operation mode yields ideal properties for monitoring surface movements and is usually operated in single pass mode to minimize the time lag in order to monitor fast changing movements, like ocean currents.
- **across track interferometry:** The sensors are aligned perpendicular to the orbit track. This mode is ideal for DEM generation in both time modes.

Since the InSAR measurements rely on the combination of SAR images acquired by at least two satellites called *master* and multiple *slave*, the data generated by the Sensors must be synchronized. The synchronization takes place in form of a interpolation where all slave images are interpolated to fit on the georeferenced data grid of one selected master image. The interferometric phase difference between two sensors S_1 and S_2 can be expressed by

$$\Delta\Phi_{int} = \frac{4\pi}{\lambda}\Delta_r, \tag{2.31}$$

where Δ_r represents the travel path difference between the two signals. Figure 2.8 shows an

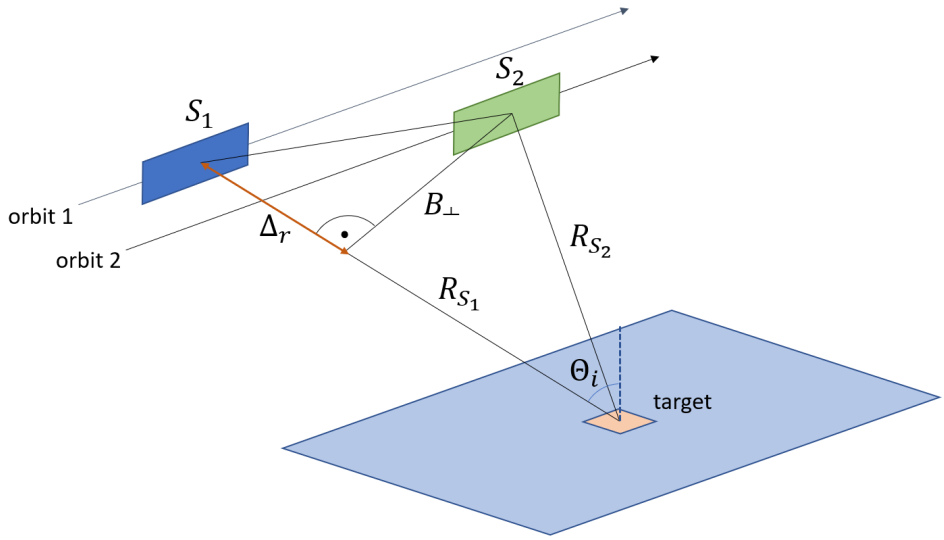

Figure 2.8 InSAR geometry for across-track interferometry by two sensors and a flat earth model: S1 as master and S2 as slave.

exemplary model for the InSAR geometry with all important parameters. The travel path difference for single pass mode is defined as $\Delta_r = 2(R_{S_1} - R_{S_2})$, while the concerning parameter for the repeat pass mode defines as $\Delta_r = R_{S_1} - R_{S_2}$. The height of ambiguity (HoA) for the system can be defined as

$$HoA = \frac{\lambda \cdot R_{S_1} \cdot \sin(\Theta_i)}{2B_\perp}, \tag{2.32}$$

and is defined as a full 2π shift of the interferometric phase. The parameters for (2.32) can be seen in Figure 2.8, which shows the general InSAR geometry for a flat earth model, with R_{S_1} being the distance between S_1 and the target, Θ_i the incidence angle and $B_\perp$ the baseline between both receivers perpendicular to the line of sight.

2.3.2 Interferometric Coherence and Noise

For evaluating the quality of InSAR products, the key parameter, which gives information about the amount of noise in the interferogram, is the interferometric coherence γ. It represents the normalized complex correlation coefficient between the master S_1 and its slave S_2 and can be calculated from

$$\gamma = |\gamma|e^{j\Phi} = \frac{\mathbb{E}[S_1 \cdot S_2^*]}{\sqrt{\mathbb{E}[|S_1|^2]} \cdot \sqrt{\mathbb{E}[|S_1|^2]}}, \tag{2.33}$$

where $\mathbb{E}[\cdot]$ is the expected value. The coherence γ ranges from 0 to 1 describing the correlation of both images, with 1 corresponding to full correlation and 0 to no correlation. The interferometric coherence can be seen as the multiplication of different error sources, which form the final coherence factor γ[35]. Contributers are for example the coherence loss due to the limited SNR γ_{SNR}, the loss

due to the relative Doppler shift spectra γ_{Az}, the loss due to ambiguity decorrelation γ_{Rg}, γ_{Vol} as the loss due to volume decorrelation, γ_{Temp} represents the temporal decorrelation and the coherence loss in raw data quantization γ_{Quant}, which will be further explained in section 3.3

$$\gamma = \gamma_{SNR} \cdot \gamma_{Az} \cdot \gamma_{Rg} \cdot \gamma_{Vol} \cdot \gamma_{Temp} \cdot \gamma_{Quant}. \tag{2.34}$$

The contributer with the most imapct is the coherence loss due to the limited SNR γ_{SNR}, which can be calculated from

$$\gamma_{SNR} = \frac{1}{\sqrt{(1 + SNR_1^{-1}) \cdot (1 + SNR_2^{-1})}}, \tag{2.35}$$

with $SNR_{1/2}$ describing the SNR for the master and slave channel. The SNR of the single channels can be calculated from

$$SNR = \frac{\sigma_0^{\Theta_i}}{NESZ_{1,2}^{\Theta_i}}, \tag{2.36}$$

with σ_0 describing the normalized backscattering coefficient and $NESZ$ the noise equivalent sigma zero from (2.29), both as function of the incidence angle Θ_i.

2.4 Staggered SAR

Conventional SAR observations always come with the constraint of having a fine azimuth resolution or wide swath width. The former requires a sufficiently low PRF in order to match the Shannon sampling theorem described in (2.25) and have at least one receive window during a PRI. Hence, the PRF decreases for wider swaths, since the chirp duration increases and the PRI as well. The latter, on the other hand, improves with increasing Doppler Bandwidth, which increases with higher PRF. In order to guarantee a uniform sampled data stream the PRF has to hold

$$PRF = \frac{2v_{sat}}{L_{az}}, \tag{2.37}$$

with v_{sat} as the satellite speed and L_{az} representing the azimuth antenna length. Over the years, several new techniques have been developed to widen the swath, without decreasing the azimuth resolution further. Those methods are using Multiple Azimuth Channels (MAC) and Digital Beam Forming (DBF) in elevation to continuously scan a wide swath, for the implementation of the so called Scan on Receive (SCORE). Despite the advantages, this method brings the problem of blind spots in the acquisition, since the antennas are only able to either transmit or receive. By using a constant PRI, those blind spots always align in the same range distance, creating blind strips in the final image. Staggered SAR is solving this drawback by using a cyclically changing PRI, to vary the location of the missing spots. The idea of changing the PRI to vary the blind spot location was first independently developed in [11] and [16] and later further developed to the concept of Staggered SAR [31].

There are different ways to distribute the location of the blind spots. One option is to randomly distribute them over the image. If a significantly small percentage of pixels is missing, the resolution of the acquisition only slightly degrades and can be focused without significant performance loss [28]. The resulting image, however, shows high sidelobes, which potentially shadow bordering pixels with lower amplitude. High sidelobes can be avoided by the varying PRI in a way, such that two consecutive azimuth samples are never missed. An example of a staggered SAR like PRI sequence can be seen in Figure 2.9. Together with a high azimuth oversampling the missing spots can then be reconstructed by interpolating the non-linear sampled acquisition on an equally spaced grid. This method provides a continuous and large swath up to 350 km without the use of multiple sub-swaths or a large antenna. During the design of the PRI sequence the minimum PRI must be chosen in consideration of the Shannon theorem (2.25) to ensure a proper azimuth sampling. The maximum PRI,

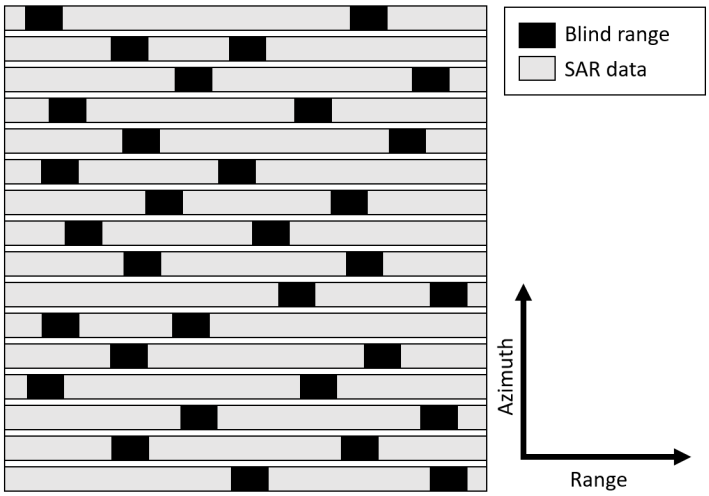

Figure 2.9 Blind range locations for staggered SAR with changing PRI

on the other hand, is restricted by the maximum gap width of the system. After the signal acquisition, in order to reconstruct the gaps and for simpler focusing, the signal needs to be translated from the non-uniform PRI on a uniformly sampled raw data grid. Best Linear Interpolation (BLU) [32] represents a reliable interpolation method, since it uses the correlation between subsequent samples to estimate the new samples. For an adequate reconstruction using BLU, a sufficient oversampling (i.e. correlation) of data in azimuth direction is required. The high oversampling also means a lot data to be stored on board, which is strictly limited for spaceborne SAR. Thus, staggered SAR requires an almost instant downlink of the acquired data.

3 SAR Raw Data Quantization

Quantization is a process where an input value is mapped on the closest value of a fixed set of output values. Quantization can be performed on time discrete as well as time-continuous signals after a proper sampling and is mainly used to digitize signals, coming from a continuous time source. Under the right conditions the process leads to less data consumption with the drawback of a lower resolution in the data representation. In signal processing, as well in SAR systems the discretization of the analogue time continuous signal is an essential step before further processing steps and is generally performed using a Analogue to Digital Converter (ADC). After the quantization with the ADC, which will be further explained in the upcoming section, the time and value discrete signal is stored in the onboard memory and down-linked to the ground segment for reconstruction. This quantization process (as well as all quantization methods in this thesis) is a lossy process, which means that the original signal can not be fully recovered from the quantized signal. The quantization error represents a key parameter, when evaluating the quantization process, since it gives direct information about the similarity of the quantized signal to its original. Generally applies, that the smaller the quantization, the better the reconstruction and therefore the final SAR image quality. Therefore, it is important to keep the error as small as possible, which can be done by increasing the set of output values. On the other hand one has to consider the data consumption, which makes it mandatory to find the optimal balance between a sufficiently good image quality after reconstruction and a good data reduction. The quantizer in the following sections are all treated as Cartesian quantizer, which means that the imaginary and real part of the complex SAR signal are processed separately, due to their uncorrelated properties according to the Central Limit Theorem (CLT). In the following sections, a basic introduction on quantization is given, as well as the impact of quantization errors and an overview over the most important parameters during the quantization according to [9][14][34]. In the last sections of this chapter, two state of the art quantizers, the Block Adaptive Quantizer (BAQ) and the Dynamic Predictive BAQ (DP-BAQ) [23] are presented.

3.1 Quantization Basics

As already stated in the previous section it is required to discretize, i.e. quantize, a time continuous signal, like the backscattered pulses during a SAR acquisition, before applying further processing steps. For a generic SAR system the quantization starts by sampling the analogue signal in time. Subsequently, all amplitudes of the resampled signal are mapped from the infinite set of analogue values to the matching one in a fixed set of output values. This can be done by firstly assigning each input value of the analogue signal to input intervals ξ_i, which are defined by the *decision levels* d_i. Secondly, all values of one input interval are mapped to the same *reconstruction level* r_i, which is assigned to that specific interval. The set of possible reconstruction levels is called the *alphabet* of the quantizer and far less complex than the range of input values. Its length depends on the number of bits N_b representing a single output value. In case of a binary system the alphabet length is defined as

$$M = 2^{N_b}. \tag{3.1}$$

As already mentioned, the decision levels describe the boundaries of the input intervals ξ, which are defined as M intervals in a defined input range $[+/-V_{clip}]$. By dividing the full input dynamics into intervals, each of the analogue samples can be represented by the interval covering him.

$$x \in \xi_i \quad \text{,with} \quad \xi_i = [d_i, d_{i+1}], \quad i = 1, 2, \ldots, M. \tag{3.2}$$

Values that outreach the maximum value i.e. $|x| > V_{clip}$ are automatically "clipped", i.e. set to the maximum valued input interval according to its sign. The translation from input value to output one is defined by the quantizers characteristic transfer function f_q, which also defines the type of the quantizer itself. Depending on the position of the decision boundaries, it is possible to define two main quantizer types. The first type is called *midtread* quantizer , since it allows for a reconstruction level at the value of zero. Its transfer function can be seen in Figure 3.1a. The second type on the other hand is named *midrise* quantizer. It has a step in the transfer function placed directly on the zero reconstruction value, which allows the quantizer to always consider the sign of the input signal in the output, since they never become zero as it can be seen in Figure 3.1b. Due to the sign consideration during the reconstruction, the midrise is typically used in SAR systems as well as in this thesis for further calculation.

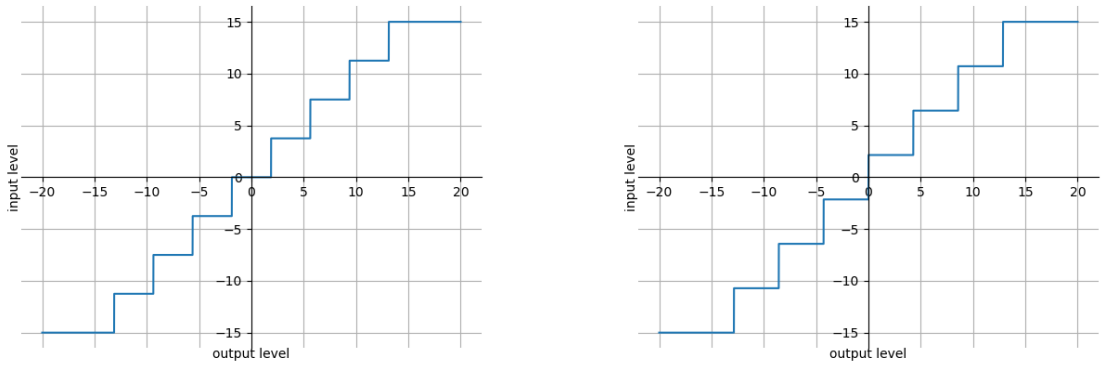

(a) Transfer function of a uniform midtread quantizer with $V_{clip} = 15$ and $N_b = 3$.

(b) Transfer function of a uniform midrise quantizer with $V_{clip} = 15$ and $N_b = 3$.

Figure 3.1 Transfer functions for uniform quantizer.

Assuming a zero mean random distributed signal, the transfer function of a linear distributed midrise quantizer can be formulated as

$$s_{q,n} = \frac{s_n}{\|s_n\|} \cdot \Delta \cdot \left(\left\lfloor \frac{\|s_n\|}{\Delta} \right\rfloor + \frac{1}{2} \right), \tag{3.3}$$

for the n-th sample of the quantized signal. In the upper equation, s_n describes the n-th sample of the input signal and $\lfloor \cdot \rfloor$ the "floor" function, which limits the value to the next integer less or equal to itself. Δ is called step size, which is defined as the distance between two decision levels and describes the resolution of the quantizer. The placing of the decision levels along the input signal space is a key parameter during the quantization design. The levels can have uniform and non-uniform spacing to optimally fit the signal statistics. For a Gaussian input, such as SAR raw data, a uniform quantizer is used. For an uniform sampled transfer function the reconstruction levels are equally distributed between $[+/-V_{clip}]$ in the center of the input intervals ξ and can be therefore defined as

$$\Delta = \frac{2V_{clip}}{2^{N_b} - 1}. \tag{3.4}$$

3.2 Quantization Errors

As mentioned in the previous sections, quantization is a lossy process, which means that the quantized signal can not be fully reconstructed. The resulting distortion of the signal is represented in the

quantization error q, which identifies the difference between the original signal s and the quantized signal s_q by

$$q = s - s_q. \tag{3.5}$$

Alongside errors caused by the quantizer, like the *granular* and *clipping error*, there are also those, which are caused by the SAR acquisition itself, like the *low scatter suppression* and *phase error*. All these errors will be introduced in the following.

3.2.1 Granular and Clipping Error

Based on the CLT, a SAR signal can be assumed to be a random distributed, zero mean signal x with a variance σ_x^2 and a probability density function (pdf) of

$$\sigma_x^2 = \mathbb{E}[X]^2 = \int_{-\infty}^{+\infty} x p_x(x) dx. \tag{3.6}$$

Due to the random nature of the input signal x and since the quantized signal is based on the same process, the quantized signal x_q has also random properties. Therefore, the quantization error q, which is according to (3.5) directly dependent on both variables, can be assumed as a zero-mean random variable with a pdf $p_Q(q)$ of

$$\sigma_Q^2 = \mathbb{E}[Q]^2 = \int_{-\infty}^{\infty} [x - f_q(x)]^2 p_X(x) dx. \tag{3.7}$$

The quantization error can be split into two main components, which are here further explained:

- *clipping error*: The clipping error describes the values falling out of the input window between $[+/-V_{clip}]$ and is named after the process of clipping all values above/below that level to the maximum/minimum reconstruction value r_{clip}. This introduces a distortion to the quantization process, since the clipped values can not be correctly reconstructed. Its pdf is defined as

$$\sigma_{qc}^2 = \int_{-\infty}^{-V_{clip}} (x + r_{clip})^2 p_X(x) dx + \int_{+V_{clip}}^{+\infty} (x - r_{clip})^2 p_X(x) dx. \tag{3.8}$$

- *granular error*: This error considers the error within the single decision levels, thus describes the precision of the quantizer. During the quantization, many input values of different amplitudes are mapped to the same decision interval, which is then represented by only one specific reconstruction value. Consequently, after their transformation they can not be completely reconstructed, which results in the granular error. Under consideration of the M decision levels from (3.2), its pdf is defined as

$$\sigma_{qg}^2 = \sum_{k=2}^{M-1} \int_{d_k}^{d_k+1} (x - r_k)^2 p_X(x) dx. \tag{3.9}$$

  In case the decision levels are sufficiently sampled, the *high rate approximation* holds and the granular error can be assumed to be uniformly distributed. Its pdf simplifies to

$$p_Q(q) = \begin{cases} \frac{1}{\Delta} & \text{if } |q| \leq \frac{\Delta}{2}, \\ 0 & \text{otherwise,} \end{cases} \tag{3.10}$$

  and the variance of the quantization noise can be expressed by

$$\sigma_Q^2 = \frac{\Delta^2}{12} = \frac{1}{3} V_{clip}^2 2^{-2N_b}. \tag{3.11}$$

The error contributions can be influenced by setting the signal dynamic. Therefore, the system parameter have to be carefully chosen to minimize the quantization error. In general, the granular error increases when enlarging the dynamic range of the signal. This happens, if the clipping value V_{clip} is set too high, or the signal-to-clipping ratio γ_{clip}, which will be further explained in section 3.3, too low. If, on the other hand, the clipping is set too low for the signal, the amount of samples being set to V_{clip} increases and the clipping error with it. In order to minimize the quantization error, the right balance for the right signal dynamic has to be found, which will be discussed in section 3.3.

3.2.2 Low Amplitude and Low Scatterer Suppression

Granular and clipping error are the biggest contributers to the quantization error, both depending on the quantization parameters, and are not influenced differently for higher or lower amplitudes. When investigating the phase error introduced by the quantization process on the other hand, a strong relation between the error and the signal amplitude can be seen. Figure 3.2 shows two complex input samples x_i and x_j and their corresponding quantized versions y_i and y_j. Even though the amount of granular error e_g is equivalent, the phase differs much more for the low amplitude value. This implies a more imprecise sensitivity of the quantizer at low amplitudes, resulting in much higher phase errors, worsening the performance of the Cartesian quantizer. The maximum possible phase error Δ_Φ occurs for low amplitude values and is bounded to $45\ °$, according to

$$|\Delta_\Phi|_{max} = \frac{|\Theta_{x_a,y_a} - \Theta_{x_b,y_b}|}{2}. \tag{3.12}$$

Another error that occurs during the quantization is caused by the superposition of high and low backscatter intensities. In particular, if two scatterers with different backscatter properties lie close to each other, i.e. the azimuth distance between both targets in azimuth d_{az} is significantly smaller than the synthetic aperture length L_s and, in range, d_{rg} is smaller than the chirp length L_{chirp}

$$d_{az} \ll L_s = \lambda \frac{R_0}{L_a} \quad \text{and} \quad d_{rg} \ll L_{chirp} = \frac{c_0 \tau_p}{2}, \tag{3.13}$$

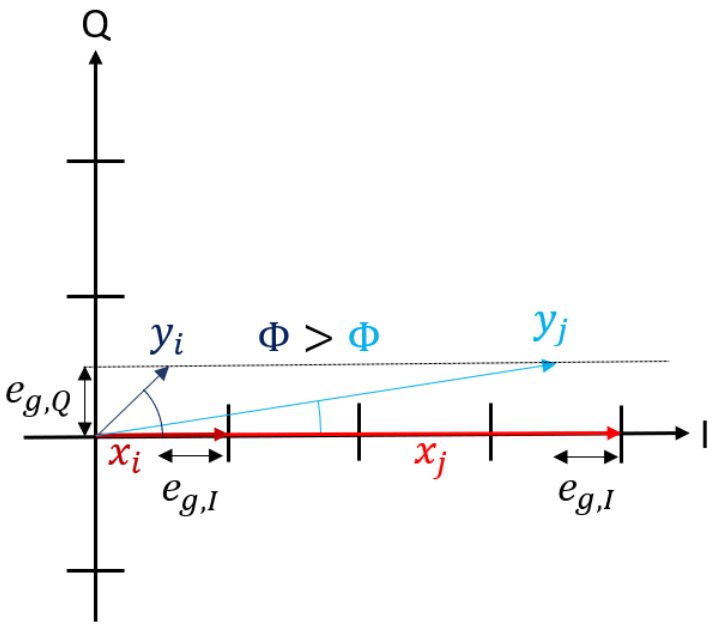

Figure 3.2 Example plot for the phase error: The input values are shown in light and dark red and the output values correspondingly in light and dark blue. While the granular error is the same for both samples, the phase error for the low amplitude sample is higher.

both targets are overlapping and the stronger backscatter shadows the lower one, which is called *low scatter suppression*. Since a Max-Lloyd quantizer, which will be further explained in section 3.4, adapts to the mean signal power, the stronger scatter is well represented thanks to its higher amplitude, while the low backscatter can not use the full dynamic of decision levels, resulting in a coarser representation.

3.3 Quantization Parameters

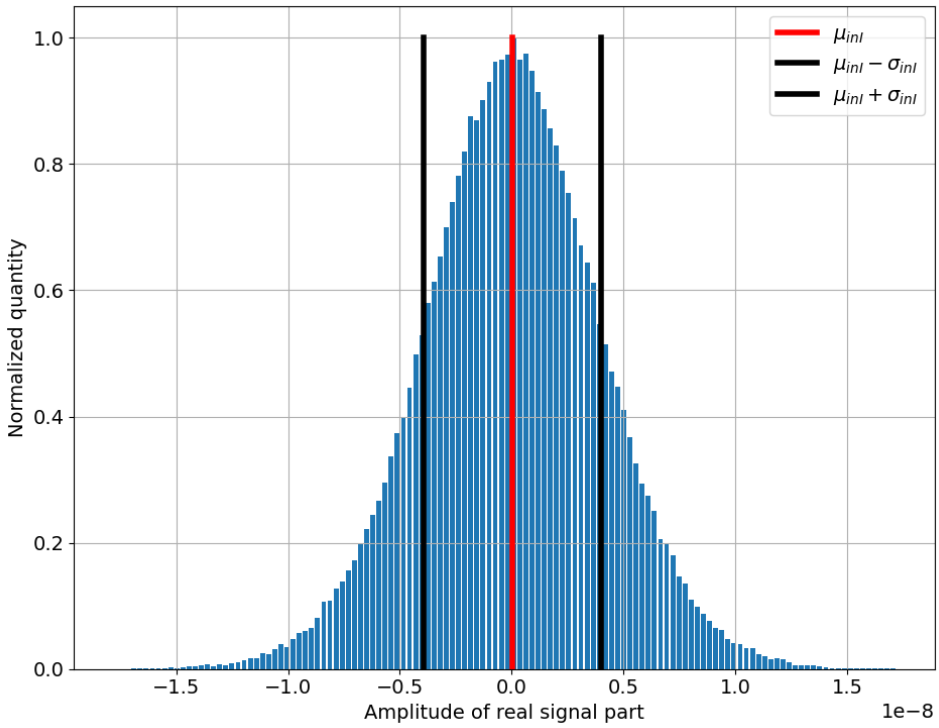

Figure 3.3 Histogram of the real part of a SAR image acquired by real SAR data. Additionally to the histogram, the plot shows the standard deviation of the image and its mean value.

3.3.1 Signal to Quantization Noise Ratio

The Signal to Quantization Noise Ratio (SQNR) is the general measurement for the quality of the quantization process. It can be described as the difference between the variance of the input signal σ_X^2 and the variance of the quantization error σ_Q^2

$$SQNR = \frac{\sigma_X^2}{\sigma_Q^2}. \tag{3.14}$$

If a complex signal is considered, the SQNR can either be calculated separately with (3.15) or, due to their uncorrelated property, by means of a cumulative representation:

$$SQNR = \frac{\sum_{i=1}^{N} |x_i|^2}{\sum_{i=1}^{N} |q_i|^2}, \tag{3.15}$$

where i is the sample number, x the input signal and q the quantization error defined in (3.5). As already stated in the previous sections, the error variance strongly depends on the number of bits N_b used for the quantization. When investigating the direct effect of the bit rate on the performance

of a quantizer, like an optimal ADC, it is possible to derive an expression for the approximate gain, by substituting (3.11) into (3.14)

$$SQNR_{dB} = 10 \cdot log_{10} 2^{2N_b} \approx 6 \cdot N_b dB. \tag{3.16}$$

3.3.2 Signal-to-Clipping Ratio

In order to achieve the best attainable quantization performance, the signal statistics must be taken into account when defining properly adapted quantization parameters. The best way to evaluate the chosen parameters is to analyse the Signal-to-Clipping ratio γ_{clip}, which rates the actual fitting of the quantization space on the input signal. The corresponding relation is derived from the ratio of the maximum input V_{clip} and the input signals standard deviation σ_x, which is visible for the real part in Figure 3.3

$$\gamma_{clip} = \frac{\sigma_x}{V_{clip}} = \frac{\sqrt{\sigma_{inI}^2 + \sigma_{inQ}^2}}{V_{clip}}. \tag{3.17}$$

$$\gamma_{clip} = \frac{\sqrt{\sigma_{inI}^2 + \sigma_{inQ}^2}}{V_{clip}}, \tag{3.18}$$

with σ_{inI} and σ_{inQ} describing the standard deviation of the real and imaginary part, respectively. Under the assumption that the two independent processes have the same standard deviation, (3.18) simplifies to

$$\gamma_{clip} = \sqrt{2} \cdot \frac{\sigma_{inI}}{V_{clip}}. \tag{3.19}$$

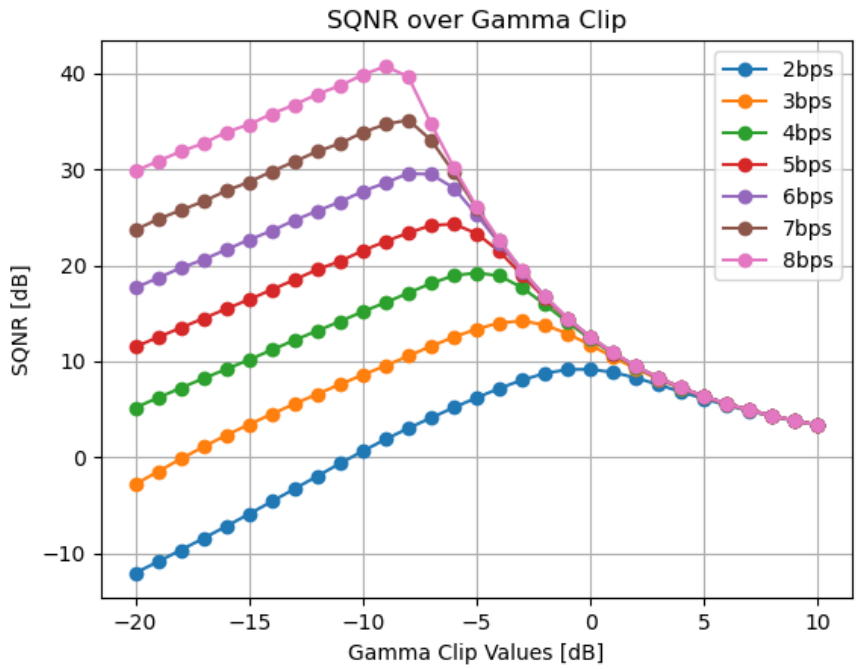

Figure 3.4 SQNR plot in dB of a uniform midrise ADC for different bitrates (bps) over different γ_{clip}, with $V_{clip} = 127.5$.

In order to control and adapt the signal dynamic, the value of γ_{clip} is usually set to a fixed value that brings maximum performance and is then used to scale the input signal accordingly to the desired range. The scaling factor α can be calculated from (3.19)

$$\alpha = \frac{\gamma_{clip} \cdot V_{clip}}{\sqrt{2} \cdot \sigma_{inI}}. \tag{3.20}$$

Figure 3.4 shows the influence of the clipping factor γ_{clip} on the quantization performance. The plot shows the SQNR values in dB, as reference for the quality of the quantization, of an ideal ADC at different bit rates. The performance was hereby tested for different values of γ_{quant} on the quantizer and analyzed to find the optimal value for controlling the signal dynamic.

The left side of the plot shows the effect of a high signal dynamic, which compromises the performance, featuring granular error. When increasing the scaling factor, the SQNR of the quantized signal constantly improves until a value close to -10 dB. After that value the second effect, which describes the effect of the clipping error, can be seen. Due to the insufficient scaling of the signal it gets distorted during the quantization and the performance drops.

3.3.3 Quantization Coherence

As already mentioned in chapter 2.3.2, the quantization coherence is also a contributer to the coherence factor γ of an InSAR system [36]. The quantization coherence describes the effect of the quantization process on a SAR interferogram and is therefore an important and informative factor for evaluating the quantization performance. The value of γ_{Quant} can be calculated solely from the SQNR as

$$\gamma_{Quant} = \frac{1}{1 + SQNR^{-1}} = \frac{SQNR}{SQNR + 1}. \tag{3.21}$$

3.4 Block Adaptive Quantization (BAQ)

The raw SAR signal after reception usually shows strong variations in the backscatter intensity of several dB, due to the properties of the observed surface. Under such circumstances, a common ADC quantizer with fixed decision levels d_i and clipping values V_{clip} is only applicable to a SAR signal by using high bitrates ($N_b = 8$). This performance would come at the cost of a high storage usage, which is not suitable for spaceborn systems with limited memory and downlink capacity. Block Adaptive Quantization (BAQ) is a reliable Max-Lloyd quantizer, that has proven itself to be very effective in the quantization of SAR raw data [18][22][19]. Its flow chart can be seen in Figure 3.5.

The concept of the Max-Lloyd quantizer presents a more effective option than an ADC to quantize

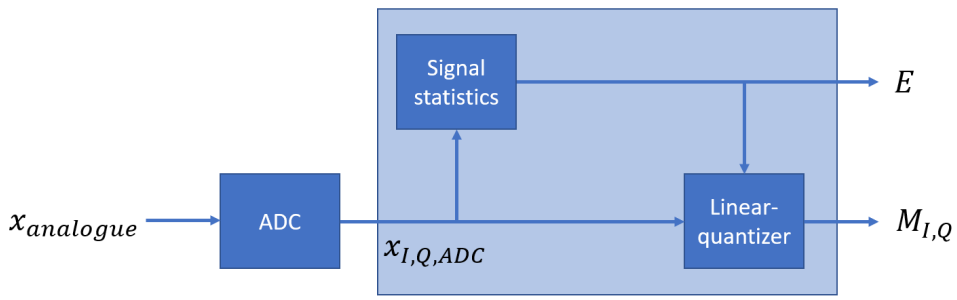

Figure 3.5 Flow chart for BAQ quantizer, with input x, ADC quantized signal $x_{q,ADC}$, exponent E, mantissa M and quantized signal x_q.

a strongly varying signal. The key behind this type of quantizer is to adapt the decision levels

to the signal by separating the signal in smaller subsets and fitting the parameters on the signal statistics of the smaller segments. The goal is to minimize the quantization noise power σ_q^2, or equivalently the SQNR of the quantization. Ideal decision levels are derived from the quantization noise power [24] and are placed directly between subsequent reconstruction levels r_i, whereas the reconstruction levels are placed at the maximum of the intervals pdf. The quantizer, which minimizes the mean square error (MSE) resulting from those problems is called *Max-Lloyd Quantizer*. In case of a uniform distributed signal, the Max-Lloyd quantizer results in a uniform quantizer, whereas all other distributed signals result in a non-uniform distributed quantizer. Due to the adaptation of the quantizer to the signal dynamic, the quantization error for each decision interval has zero mean properties. Furthermore, the error variance of each decision interval ξ_i is the same, even when increasing the stepsize Δ [14]. The adaptivity of the quantizer to the signal dynamic is usually done by scaling the input signal before the quantization and rescaling it before the reconstruction, respectively.
The realization of a Max-Lloyd quantizer on SAR data can be implemented by a cartesian BAQ, which means that the the In-phase (I) and Quadrature (Q) components are processed separately, due to the statistically independent characteristics of the complex SAR signal. In a first step the analogue SAR signal is clipped and converted to a digital signal using an ADC at a high bitrate ($N_b = 8$) and a clipping voltage of $V_{clip} = +/-127.5$. The resulting signal can then be represented by 8 bits for each I- and Q-sample

$$I_{n,ADC} = -1^s \left(\frac{1}{2} + \sum_{i=0}^{6} M_{I,ADC,i} 2^i \right), \tag{3.22}$$

and

$$Q_{n,ADC} = -1^s \left(\frac{1}{2} + \sum_{i=0}^{6} M_{Q,ADC,i} 2^i \right), \tag{3.23}$$

with n referring to the n-th sample of the signal, i to the i-th bit correspondingly, s to the sign bit and M representing the corresponding value of the i-th bit. After the conversion by the ADC, the signal is separated along range direction into blocks of equal length L_{BAQ} and forwarded to the quantizer. The block length is hereby chosen, that the signal dynamic within the blocks is sufficiently small to properly adapt the quantization parameters.
The quantization process applied on each range line is described as follows [19]:

Compression rate, n_{BAQ}	C	E_{max}	M_{max}
8:2	2.20374	24	1
8:3	5.28038	20	3
8:4	8.50475	16	7
8:5	11.8188	12	15
8:6	15.2549	8	31

Table 3.1 Parameters for BAQ encoding, depending on the compression rate.

- ***Step 1:*** The $I_{n,ADC}$ and $Q_{n,ADC}$ components of each range line are separated into blocks of length $L_{BAQ} = 128$.
- ***Step 2:*** According to the chosen compression rate the quantizer selects the corresponding value of C from Table 3.1.
- ***Step 3:*** The C value is used to calculate the exponent according to

$$E_1 = 4 \cdot log_2 \left(1 + \frac{1}{L_{BAQ}} \sum_{n=1}^{L_{BAQ}} (\|I_n\| + \|Q_n\|) \right) - C. \tag{3.24}$$

- ***Step 4:*** The Exponent of the preceding step is rounded off to the next biggest integer less or equal to itself and compared to the maximum exponent E_{max} from Table 3.1

$$E = \min\{E_{max}, \lfloor E_1 \rfloor\}. \tag{3.25}$$

- ***Step 5:*** Using the exponent E from the prior step, the input values $I_{n,ADC}$ and $Q_{n,ADC}$ can now be scaled to $\bar{I}_n$ and $\bar{Q}_n$

$$\bar{I}_n = \frac{I_n}{2^{E/4}}, \text{ and } \bar{Q}_n = \frac{Q_n}{2^{E/4}}, \tag{3.26}$$

- ***Step 6:*** The value of each sample is compared to the maximum mantissa M_{max} from Table 3.1 and limited to it if the value exceeds the limit

$$I_{BAQ,n} = \frac{\bar{I}_n}{\|\bar{I}_n\|} \cdot \min\{\|I_n\|, M_{max}\}, \text{ and } Q_{BAQ,n} = \frac{\bar{Q}_n}{\|\bar{Q}_n\|} \cdot \min\{\|Q_n\|, M_{max}\}. \tag{3.27}$$

- ***Step 7:*** In the final step the resulting mantissa is quantized using a uniform quantizer (3.3) between $[-M_{max} - 0.5, M_{max} + 0.5]$ at a bit rate of n_{BAQ}.

The quantized mantissa alongside with the exponent E from step 4 are then transmitted on-ground. Both values are then used to reconstruct the transmitted signal according to

$$I_{n,BAQ} = -1^s \cdot \left(\frac{1}{2} + \sum_{i=0}^{n_{BAQ}-1} K_{I,i} \cdot 2^i\right) \cdot 2^{E/4}, \tag{3.28}$$

$$Q_{n,BAQ} = -1^s \cdot \left(\frac{1}{2} + \sum_{i=0}^{n_{BAQ}-1} K_{Q,i} \cdot 2^i\right) \cdot 2^{E/4}. \tag{3.29}$$

Here, K refers to the value of the i-th bit (either 0 or 1) and s to the value of the sign bit. Figure 3.6 shows the performance in terms of SQNR, for a BAQ compared to an ADC, both calculated on two dimensional simulated SAR data and a planar antenna pattern. The SQNR values of the BAQ show constantly better performance when increasing the bitrate. The BAQ even reaches a SQNR value of 9.2 dB at a bitrate of only 2 bps, which is higher than the performance of the ADC at a bitrate of 3 bps. Thus, providing a better quantization performance with less memory usage, due to its adaptivity.

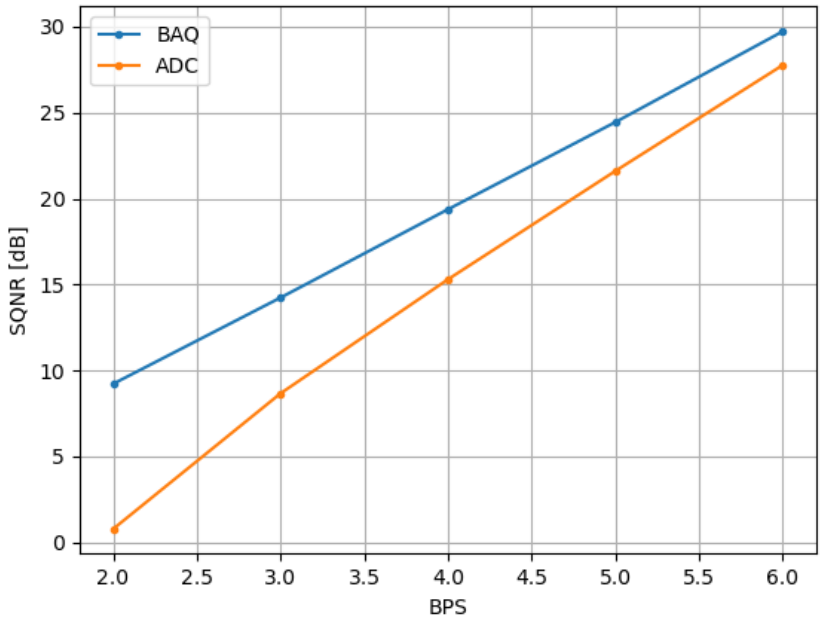

Figure 3.6 Signal to Quantization Noise Ratio (SQNR) of a BAQ compared to an ADC for all possible bitrates (bps)

3.5 Dynamic-Predictive Block Adaptive Quanitzation (DP-BAQ)

SAR acquisitions come with the generation of an huge amount of data. Especially in new acquisition methods, capable of imaging wide swath at high spatial resolutions, like staggered SAR, the amount of data increases even more. Due to the limitations in terms of processing and storage, the data need to be transferred to the ground in almost real time, which requires maximum compression of the data at the cost of minimal computational effort. There have been several approaches, using predictive coding for data reduction, which investigated on the performance on raw SAR data as well as range focused SAR data [21], [13]. In this section a new quantization method, developed at DLR, is introduced, which combines the benefits in signal dynamic reduction from Linear Predictive Coding (LPC) of different prediction orders, specially fitted on the SAR signal statistics, with the well known quantization technique of BAQ. Additionally, this new technique is specially designed for handling Staggered SAR and its varying PRI as well as blind ranges, using dynamic bit allocation and adapted handling of the prediction order in gap vicinity.

3.5.1 Linear Predictive Coding

Linear Predictive Coding (LPC), which evolved from the well known Differential Pulse Code Modulation (DPCM)[14], offers a method to significantly reduce the dynamic in signals with strong varying amplitudes. The principle of DPCM is to harness the correlation, i.e. similarity, between subsequent samples to generate a signal with lower dynamics by calculating the difference $s_d[n]$ between the original sample $s[n]$ and its predecessor $s[n-1]$

$$s_d[n] = s[n] - s[n-1]. \tag{3.30}$$

The original signal can later be reconstructed by simply inverting the procedure in (3.30).
As it becomes clear, the dynamic reduction of DPCM is only dependent on the similarity of the subtracted signal to the original one, which is limited at some point. LPC, on the other hand, exploits the correlation between subsequent samples to estimate the prediction of the current sample, which is in general more similar to the original sample than the preceding one is. Thus this method generates a signal with less signal dynamic than DPCM, by subtracting the prediction from the original

sample. The prediction is calculated from the combination of N preceding samples, each weighted by the corresponding prediction weight. The weights are calculated from the correlation values of the signal and represent the relation between the original sample and the samples, that are used for the prediction. Therefore, the prediction $\tilde{s}[n]$ can be calculated from the summation on N preceding samples $s[n-i]$, weighted by the prediction weights β_i according to

$$\tilde{s}[n] = \sum_{i=1}^{N} \beta_i \Big(s[n-i] + e[n-i] \Big), \tag{3.31}$$

where e describes the error term of the prediction process, i refers to the i-th sample before the predicted one, and N to the prediction order.
Since the prediction consists of a single linear combination, the computational requirements are not significantly increased, thus making it suitable for onboard implementation. An overview over all prediction steps can be seen in Figure 3.7. After predicting a sample from prior ones, the resulting signal can be used to calculate the difference for the upcoming sample according to

$$s_d[n] = s[n] - \tilde{s}[n]. \tag{3.32}$$

By considering the scheme in Figure 3.7, equation (3.33) can now be reformulate to express the prediction process by substituting (3.32) into (3.31), leading to

$$\tilde{s}[n] = \sum_{i=1}^{N} (s_d[n-i] + \tilde{s}[n-i]) \beta_i. \tag{3.33}$$

As can be seen, the prediction of the current sample requires the saving of only N preceding prediction errors. The errors are also used for the reconstruction of the original sample, as described by the model in Figure 3.8. By analyzing these schemes, it becomes clear that the reconstruction is the inverse process of the encoding. After initializing the prediction process, by providing the first sample as original to the reconstructor, i.e. setting the first prediction to zero, both sides hold the same information and use the same predictor to estimate the upcoming sample. Thus, possible error sources can be significantly minimized. The reconstruction process at time instance n can now be expressed under consideration of the flow chart as

$$\hat{s}[n] = s_d[n] + \tilde{s}[n]. \tag{3.34}$$

As already stated, the prediction weights are the key parameters for the design of the predictor they define the relation between prior samples and the predicted one and can be pre-calculated if the signal statistics are known.

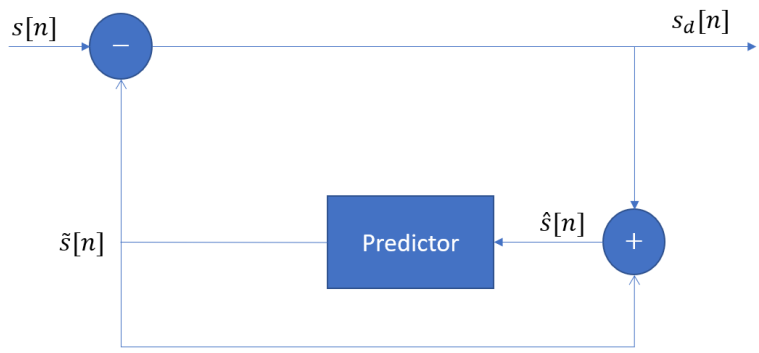

Figure 3.7 Flow chart for 1st order Predictor.

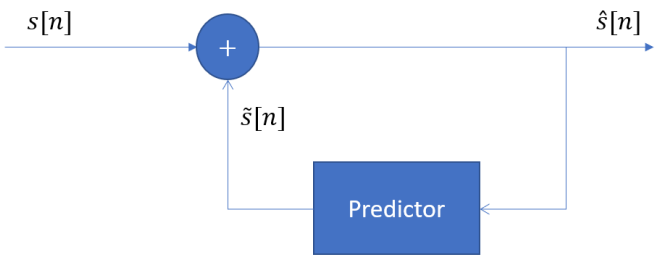

Figure 3.8 Flow chart for 1st order Reconstructor.

The weights are calculated to maximize the outcome of the quantization, which means providing the best attainable dynamic reduction. In case of LPC a low signal dynamic is directly dependent on the prediction error $s_d[n]$. The weights can be therefore calculated by minimizing the Mean Square Error (MSE) for the variance of the prediction error derived from (3.32) as [23]

$$\begin{aligned} \sigma_d^2 &= \mathbb{E}[s_d^2[n]] = \mathbb{E}[(s[n] - \tilde{s}[n])^2] \\ &= \mathbb{E}\left[\left(s[n] - \textstyle\sum_{i=1}^{N} \beta_i \cdots [n-i] - \sum_{i=1}^{N} \beta_i \cdot e[n-i]\right)^2\right], \end{aligned} \tag{3.35}$$

where $e[n-i]$ is the error term describing the quantization error after the prediction. Since the quantization error is also affected by the predictor, it must be weighted by β_i as well. In order to solve the MSE, i.e. to find the minimum of the variance, the derivative of (3.35) for a set of β_j, with $1 \leq j \leq N$, is set to 0

$$\frac{d\sigma_d^2}{d\beta_j} = -2\mathbb{E}\left[s[n] - \sum_{i=1}^{N} \beta_i (s[n-i] + e[n-i]) \cdot (s[n-j] + e[n-j])\right] \stackrel{!}{=} 0, \tag{3.36}$$

which simplifies to

$$\mathbb{E}[(s[n] - \tilde{s}[n])\hat{s}[n-j]] = \mathbb{E}[s_d[n] \cdot \hat{s}[n-j]] = 0, 1 \leq j \leq N. \tag{3.37}$$

By expanding (3.37)and substituting (3.32) the equation can be further simplified, considering that the quantization error $e[n]$ is independent from the input signal $s[n]$, to

$$\Phi[j] = \sum_{i=1}^{N} \beta_i (\Phi[j-k] + \sigma_e^2 \delta[j-i]), 1 \leq j \leq N. \tag{3.38}$$

In the above equation $\Phi[j]$ represents the autocorrelation of $s[n]$ and is defined at any discrete time instance n as

$$\rho[j] = \frac{\Phi[j]}{\sigma_x^2} = \sum_{i=1}^{N} \beta_i \left(\rho[j-k] + \frac{\sigma_e^2}{\sigma_x^2} \delta[j-i]\right), 1 \leq j \leq N. \tag{3.39}$$

The above equation can be represented in matrix form as

$$\boldsymbol{\rho} = \boldsymbol{C}\boldsymbol{\beta}, \tag{3.40}$$

where the single vectors and matrices are defined as follows:

$$\boldsymbol{\rho} = \begin{bmatrix} \rho[1] \\ \rho[2] \\ \rho[3] \\ \vdots \\ \rho[N] \end{bmatrix}, \boldsymbol{\beta} = \begin{bmatrix} \beta_1 \\ \beta_2 \\ \beta_3 \\ \vdots \\ \beta_N \end{bmatrix}, \boldsymbol{C} = \begin{bmatrix} 1 & \rho[1] & \rho[2] & \dots & \rho[N-1] \\ \rho[1] & 1 & \rho[1] & \dots & \rho[N-2] \\ \rho[2] & \rho[1] & 1 & \dots & \rho[N-3] \\ \vdots & \vdots & \vdots & \ddots & \vdots \\ \rho[N-1] & \rho[N-2] & \rho[N-3] & \dots & 1 \end{bmatrix}. \tag{3.41}$$

Here, the vector $\boldsymbol{\rho}$ contains the correlations of the samples used for the prediction and the estimated sample, $\boldsymbol{\beta}$ contains the prediction weights and $\boldsymbol{C}$ represents the relation between all samples used during the prediction, containing the corresponding correlation values. In order to calculate the prediction weights, equation (3.41) can be solved with respect to $\boldsymbol{\beta}$

$$\boldsymbol{\beta} = \boldsymbol{C}^{-1}\boldsymbol{\rho}. \tag{3.42}$$

3.5.2 Autocorrelation

For a proper prediction, or in particular for the calculation of the concerning weights, knowledge about the signal statistics, i.e. the autocorreation, which defines how similar subsequent samples of a data set are, is required. While this thesis work contains the analysis of multiple systems, the general derivation of the autocorrelation will be introduced, assuming a planar antenna for a Tandem-L-like system [25].
Since the quantization takes part on the raw data level, raw SAR data is considered for the derivation. As already known the complex SAR signal can be assumed as a random normal distributed process, weighted by the squared antenna pattern to represent transmission and reception properties adequately. The antenna pattern of a planar spaceborne antenna was already introduced in the planar antenna model (2.3) , which provided sufficient accuracy for this simulation. Under consideration of the independence of imaginary and real part, the SAR raw data can be defined along the azimuth dimension as circular complex signal s with a variance of σ^2 for both real and imaginary part

$$r = |G(\Phi_{az})|^2 e^{-4\pi j \frac{R}{\lambda}} \circledast s \quad \text{where} \quad \begin{matrix} \Re s \sim \mathcal{N}(0, \sigma^2) \\ \Im s \sim \mathcal{N}(0, \sigma^2), \end{matrix} \tag{3.43}$$

with $G(\Phi_{az})$ representing the azimuth antenna pattern for the planar antenna SAR system. The autocorrelation ρ_τ of the SAR raw data can then be considered as the inverse Fourrier transform of the signals power spectral density, which is defined for the planar antenna model as

$$\rho_\tau = \mathscr{F}^{-1}\left\{ \sin^4\left(\pi \frac{L_a}{2v_s} f\right) \Big/ \left(\pi \frac{L_a}{2v_s} f\right)^4 \right\}, \tag{3.44}$$

where L_a represents the antenna azimuth length, v_s the satellite velocity, and f the Doppler frequency. By performing the inverse Fourrier transformation separately on both sinc^2 functions, the autocorrelation can be derived as

$$\rho_\tau = \begin{cases} \frac{3}{4}(B_R \cdot \tau)^3 - \frac{3}{2}(B_R \cdot \tau)^2 + 1 & 0 \leq \tau \leq \frac{1}{B_R}, \\ -\frac{1}{4}(B_R \cdot \tau - 2)^3 & \frac{1}{B_R} \leq \tau \leq \frac{2}{B_R}, \\ 0 & \text{elsewhere.} \end{cases} \tag{3.45}$$

In the above equation τ stands for the time delay between the samples and B_R represents the bandwidth of the spectral power density function, which is defined as

$$B_R = \frac{2v_s}{L_a}. \tag{3.46}$$

When analysing (3.46) and (3.45) one can clearly see, that a larger antenna emits a more directive beam and can be seen, due to the reduced bandwidth as a narrower low-pass filter in the Doppler-domain. A lower velocity, on the other hand, causes a wider correlation time, since two targets will be more overlapped for a given time lag, i.e. more samples will be recorded for the same area on ground, assuming the same PRF.
Additionally, the sampling rate of the SAR image in azimuth direction (PRF) has an impact on the correlation of subsequent samples. An example for the direct impact of the PRF for a Tandem-L-like scenario can be seen in Figure 3.9, which shows the correlation values for the first six samples of the autocorrelation, depending on different sampling rates. As can be seen, the correlation values strongly decrease for lower PRF, which correspond to higher PRI and therefore higher time lags between subsequent samples.

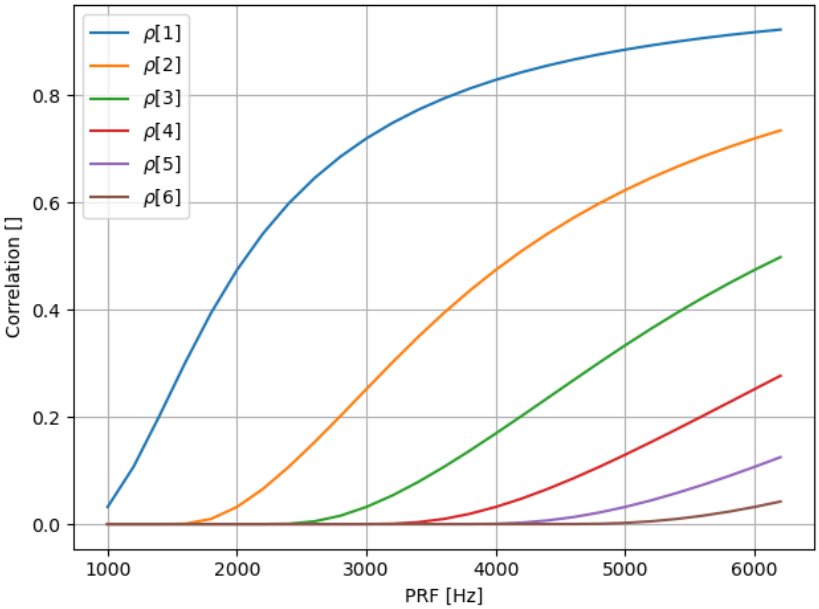

Figure 3.9 Correlation values over different sampling frequencies (PRF).

3.5.3 Coding Gain

Linear Predictive Coding uses the similarity of the predicted signal to the original signal for reducing the signal dynamic, i.e. improving the quantization process. The coding gain G_P represents the actual dynamic reduction achieved by the prediction process without the effects of the quantizer, by comparing the input dynamic, i.e. its variance σ_x^2 with the prediction errors variance σ_d^2.
The coding gain can be derived from the Signal-to-Noise ratio (SNR), which reduces coherently with the coding gain and is defined by the ratio between the power of the input signal s_d and the introduced error e as

$$SNR = \frac{\mathbb{E}[s^2[n]]}{\mathbb{E}[e^2[n]]}. \tag{3.47}$$

The SNR of the above equation can be split and reformulated by considering that the introduced error depends on both the prediction process and the quantization process as

$$SNR = \frac{\sigma_x^2}{\sigma_d^2} \cdot \frac{\sigma_d^2}{\sigma_e^2} = G_P \cdot SNR_Q. \tag{3.48}$$

The latter part in the above equation represents the SNR of the quantization process, whereas the first part describes the coding gain introduced by the predictor

$$G_P = \frac{\sigma_x^2}{\sigma_d^2}. \tag{3.49}$$

Figure 3.10 shows the coding Gain for the first four prediction orders over different sampling rates of the TerraSAR-X [33], the Tandem-L [25] and the FSAR system, which will be further explained in chapter 4. The most system parameters used for the plots can be seen in Table 3.2 A general

Parameter	Tandem-L	TerraSAR-X	F-SAR
Orbit height	745 km	514 km	<6.1 km
Carrier frequency, f_c	1.25 GHz (L band)	9.65 GHz (X band)	1.325 GHz (L band)
Range bandwidth	< 84 MHz	< 150 MHz	< 150 MHz
Mean (staggered) PRF	2700 Hz	3000 Hz	2500 Hz
Reflector diameter	15 m	10 m	0.65 m
looking angle	25°	25°	50,4°
sensor velocity	$7480\mathrm{m/s}$	$7600\mathrm{m/s}$	$90.1\mathrm{m/s}$

Table 3.2 System parameters of the Tandem-L, TerraSAR-X and F-SAR system

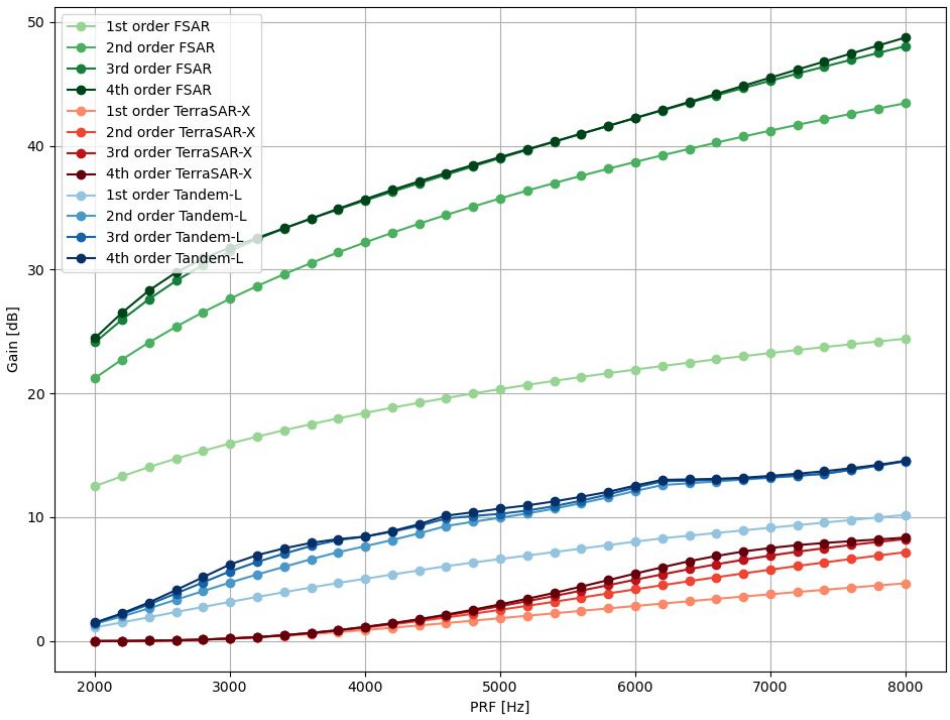

Figure 3.10 Coding gain of the TerraSAR-X system, a Tandem-L-like system, and the FSAR system for the first four prediction orders, over different sampling rates (PRF).

observation for all system is the increase of the coding gain with higher sampling rates, which can be explained by the higher similarity between subsequent samples for smaller time delays leading to more precise predictions and, therefore, to less dynamic in the prediction error. As can be seen in the plot, the FSAR system yields for much higher coding gain than the spaceborn systems, due to the higher oversampling, i.e. correlation, between the samples, caused by the reduced moving

speed. When comparing spaceborne systems the TerraSAR-X provides less gain, than the Tandem-L system, which can be explained by (3.45) and (3.46), i.e. the smaller antenna of TerraSAR-X causes a faster decrease of the correlation and results in smaller correlation values at a similar PRF. An observation for all systems, on the other hand, is, that the gain steps between the prediction orders become smaller for higher prediction orders, which can be seen as a kind of saturation where the predictor yields the maximum possible precision of the available data. Any higher order does not bring significant gain and is therefore not shown in this plot. The non-linear growth of the Tandem-L system gain for higher orders can be explained by the matrix inversion of C in the weights derivation, which shows high sensibility to zeroes, present in the correlation values.

3.5.4 DP-BAQ implementation

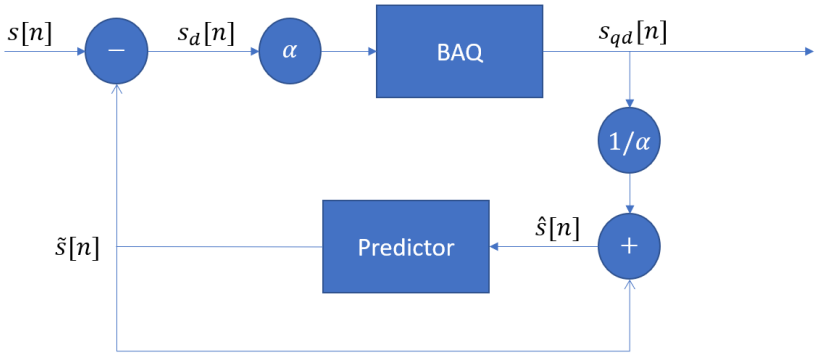

Figure 3.11 Flow chart for 1st-th order Predictive quantizer.

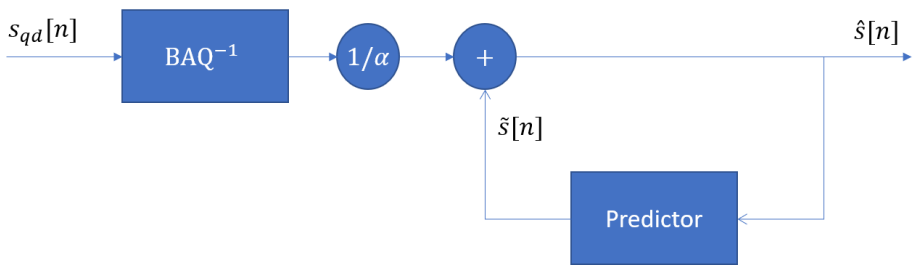

Figure 3.12 Flow chart for 1st-th order Reconstructor.

The Dynamic Predictive BAQ (DP-BAQ) is the combination of LPC and a BAQ, with prediction and quantization parameters specially adapted to the SAR signal properties. This section summarizes the results of the preceding sections in order to introduce to the processing steps necessary to implement a DP-BAQ, which are schematically recalled in Figures 3.11 and 3.12.
In preparation for the quantization, the autocorrelation for the system needs to be calculated according to section 3.5.2, since the signal characteristics are not known during the calculation. The autocorrelation is then used to calculate the prediction weights β_i according to the formulas in section 3.5.1, which are then stored in the onboard memory.
As for the BAQ, the signal is divided into range blocks of 128 bit in order to keep the signal length as short as possible for optimal signal dynamic reduction. Those blocks are then processed separately

by the DP-BAQ along the azimuth direction according to [23].
The quantization starts with the first range line being quantized by a normal BAQ, since no previous data is available for a prediction. Therefore, the range line is scaled, under consideration of the blocks variance according to (3.20), by the factor α to reduce the signal dynamic. Consequently the scaled block is forwarded to the BAQ and the quantized signal is down linked to the ground for reconstruction and additionally stored on board for the prediction of the next block. The prediction of the first range block "as is" ensures that both predictors in the encryption and decryption hold the same information base. After the first block being quantized, the predictor has information for one prior step at hand, which can be used for a first order prediction of the next sample, following this logic the prediction order increases after each quantized signal until the maximum order is reached, which makes the assignment of the prediction error a dynamic process. As already mentioned, beginning from the processing of the second range block, LPC is included to the quantization. This means that the DP-BAQ no longer quantizes the original signal, but the prediction error instead, which has much less signal dynamic, i.e. less error contribution in combination with a quantizer. Nevertheless, a BAQ is still a lossy process, which means that the quantization error remains in the resulting signal. In order to keep the outcome of the estimation process in the predictor and the reconstructor as close as possible, the quantization error is considered in both processing steps by using the quantized signal as input.
The following description explains the single processing steps of the predictive part of the DP-BAQ, which are repeatedly applied on each range block $s[n]$, with n referring to the index of the block in azimuth direction:

1. In a first step the last preceding prediction error quantized by the BAQ $s_{qd}[n]$ is reconstructed according to (3.28) and (3.29) and stored on board as $\hat{s}_d[n-i]$.

2. Subsequently, the predictor calculates the prediction $\tilde{s}$ based on the pre-calculated prediction weights β_i and the preceding samples according to

$$\tilde{s}[n] = \sum_{i=1}^{N} \left(\frac{\hat{s}_d[n-i]}{\alpha_{n-i}} + \tilde{s}[n-i] \right) \beta_i. \tag{3.50}$$

3. The prediction of the current sample $\tilde{s}$ is then used, together with its original $s[n]$, to calculate the prediction error $s_d[n]$ as

$$s_d[n] = s[n] - \tilde{s}[n]. \tag{3.51}$$

4. Before forwarding the difference $s_d[n]$ to the BAQ, the dynamic of the signal is adapted by multiplying it with the scaling factor α as described for the BAQ sample.

5. The BAQ is then applied on the scaled prediction error and the resulting quantized version $s_{qd}[n]$ is downlinked to the ground and stored onboard for the next prediction step.

6. On ground, the received signal is reconstructed from the quantized signal to $\hat{s}_d[n]$ according to (3.28) and (3.29) and used to calculate the reconstructed range block $\hat{s}[n]$ of the original signal as

$$\hat{s}[n] = \frac{\hat{s}_d[n]}{\alpha_n} + \tilde{s}[n]. \tag{3.52}$$

As mentioned before, the prediction order changes during the "starting"-phase of the predictor and stays constant as soon as the maximum level is reached. This model only holds for continuous signals, i.e. a data set without gaps in the SAR raw data, which is not the case for Staggered SAR as stated in section 2.4. The constant transmission and reception of Staggered SAR results in gaps, i.e. blind ranges, in the generated SAR raw data matrix. For the DP-BAQ this has two effects: firstly, there is no data to be quantized in the gap position and, secondly, the data can not be used for the prediction of succeeding samples.

Since the position of the gaps is known a priori, the quantizer can adapt to this situation [23].
A gap in the SAR image is treated by the DP-BAQ like a restart of the whole quantizer. The first sample after the gap is therefore quantized using a non predictive BAQ and the subsequent ones are quantized using a DP-BAQ with step-wise increasing prediction order, until the maximum prediction order N is reached, as can be seen in in Figure 3.13. When reaching the maximum, the quantizer stays at that order until the next gap sequence.
Except from the dynamic adaption of the quantizers prediction order, which is necessary due to the missing data, the gaps are also adapted with regard to the quality of the reconstructed signal. Because of the high oversampling, the neighboring samples of a gap can be used to reconstruct the missing ones, which can be further improved by providing more accuracy for the samples forming the base for the reconstruction. During transmission, the SAR system would normally waste valuable

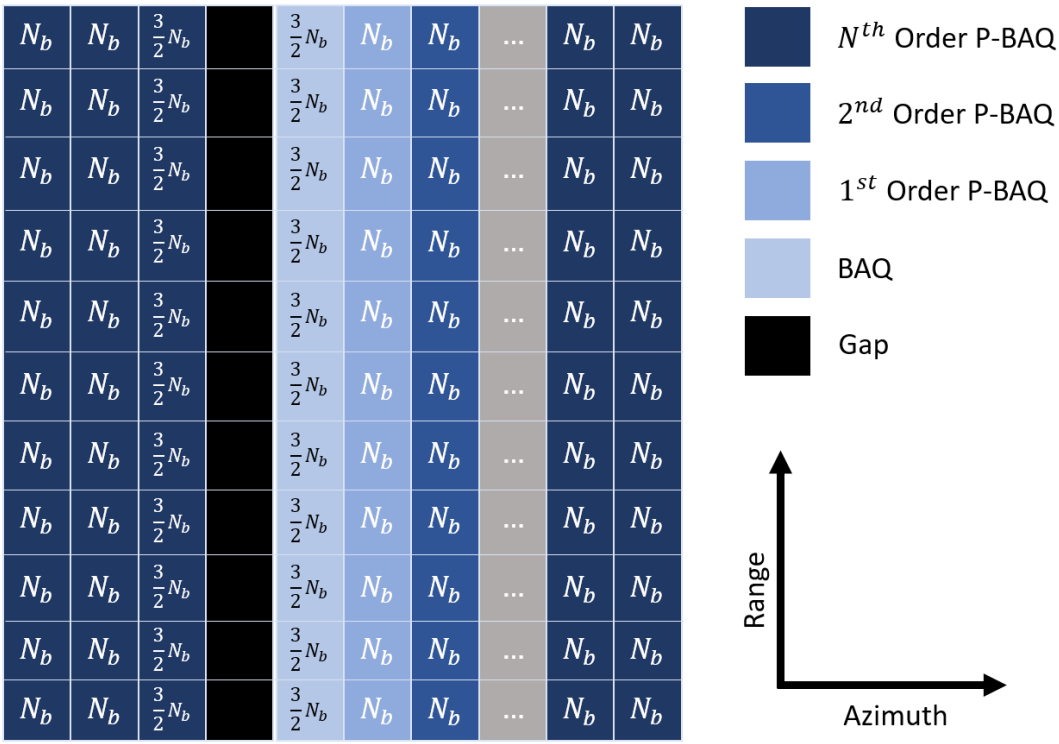

Figure 3.13 Example raw data matrix with gaps and the corresponding prediction order and bitrate. N_b represents the average bitrate and the color of each matrix cell corresponds to the used prediction order.

space in the downlink by sending the gap data as “empty” bits. Thus, the space, which would be normally used for transmitting the gap content, can be used to improve the sample quality in gap proximity. By using the a priory information about the location of the gaps, the bits can be dynamically assigned to send additionally data for the bordering samples. Figure 3.13 shows an exemplary two-dimensional scheme for Staggered SAR data with gaps, as well as the bitrate used for the quantization of each sample close to the gap. As can be seen, the samples close to the gaps are quantized at a bitrate of $\frac{3}{2}N_b$ instead of the normal average bitrate of N_b. The $\frac{3}{2}N_b$ bits correspond to the normally available bits for transmission and the additionally distributed ones from the gap sample. Table 3.3 shows the exact bit allocation for different bit rates close to the gap. The variation in the amount of samples that are quantized in a higher bit rate can be explained by the distribution of $\frac{N_b}{2}$. Since only a limited set of bit rates is available, the additional bits must be distributed on multiple samples.

bit rate	before cell	on gap	1st after gap	2nd after gap	3rd after gap
2	3	0	3	2	2
3	4	0	4	4	3
4	6	0	6	4	4
6	8	0	8	8	6

Table 3.3 Variable bit allocation before and after the gap for different bitrates.

Analytical Derivation for Gaussian inputs

The upcoming section will present a mathematical general mathematical derivation for the coding gain. Under the assumption of a normal distributed signal, which is the case for SAR (as visible in Figure 3.3), the variance of the prediction error can be expressed as the variance of the difference between two random distributed signals

$$\mathcal{D} \triangleq \mathcal{X} - \mathcal{Y} \sim \mathcal{N}(0, \sigma_x^2 + \sigma_y^2 - 2\sigma_{xy}) \quad \text{where} \quad \begin{array}{c} \mathcal{X} \sim \mathcal{N}(0, \sigma_x^2) \\ \mathcal{Y} \sim \mathcal{N}(0, \sigma_y^2). \\ \sigma_{xy} = \sigma_x \sigma_y \rho \end{array} \tag{3.53}$$

σ_x^2 and σ_y^2 in the above equation represent the variance of both random processes and σ_{xy} the covariance between both variables, which can be calculated by the multiplication of both variances times the correlation between them. Since the prediction is calculated on the original sample, both variances depend on the same process and can be therefore assumed to be equal according to the stationary hypothesis ($\sigma_x = \sigma_y$). Despite the equality of both variances the only known parameter of (3.53) is the correlation between both samples. The exact mathematical derivation for the weights and gain of the first four prediction orders will be presented in the Appendix.

4 F-SAR

F-SAR is an airborne SAR system, which is operated by the German Aerospace Center (DLR) [1], [12] and has its main purpose is the development and testing of SAR technologies as well as the generation of common SAR products. The SAR system is mounted on a Dornier DO228-212, which is also run by the DLR and was used for the DLR E-SAR system before. The plane is capable of reaching altitudes up to 6100 m and flying at a velocity of $90\mathrm{m/s}$, with an altitude variation below 2 m during the SAR acquisition, which can last up to 2.75 to 4.75 hours, depending on the instrumental configuration.

The speciality of F-SAR is the ability of operating acquisitions at different polarizations and wave-

Figure 4.1 Research airplane Dornier Do228-212, with mounted F-SAR carrier (back) and P-band antenna (bottom).

lengths simultaneously, while providing a high range resolution, which makes it ideal to test and develop new SAR technologies. The high range resolution is provided by the large system bandwidth (2.24), which is spacing from 50 MHz at L-band up to 760 MHz for X-band and can be seen along with the supported frequency bands as well as the corresponding system parameters in Table 4.1.

The antennas for the different frequency bands, which are all pointing to the area on the right hand side of the plane, i.e. right-looking SAR, can be installed and removed according to the mission requirements. F-SAR provides space for up to seven different antennas, which is shown in Figure 4.2.

The three X-band antennas are highlighted in blue, the two S-band antennas in orange, the C-band antenna in green and one L-band antenna purple, which is placed separately under the front of the airplane due to its size. A general overview of the available antenna configurations can be seen in Table 4.2 along with the maximum endurance and the band-specific center frequency.

The acquisition modes, available for each frequency band depends on the number of antennas and their placement. While repeat pass Polarimetric Interferometric SAR (repeat pass PolInSAR) is available for any frequency band, single pass PolInSAR is restricted to a limited set of frequencies, since multiple antennas are only available for X- and S-band. The interferometric constellation are thereby available as across track (XTI) measurements for X- and S-band, with a baseline of ~ 1.6

	X	C	S	L	P
RF [GHz]	9.60	5.30	3.25	1.325	0.435
Bandwidth [MHz]	760	384	300	150	50
PRF [kHz]	5	5	5	10	10
P_T [kWpeak]	2.5	2.2	2.2	0.9	0.9
Rg. resolution [m]	0.3	0.6	0.75	1.5	2.25
Az. resolution [m]	0.2	0.3	0.35	0.4	1.5
Flight altitude range	from 2000 ft above ground to 22000 ft above mean sea level.				
Off-Nadir angle range	Nominal from 25° to 60°.				
Ground range coverage	From 600 m up to 6 km according to the flight altitude.				
Sampling	8 bit real; 1GS/500MS selectable; max number of samples 64k per range line; four recording channels.				

Table 4.1 Technical parameters of the F-SAR system.

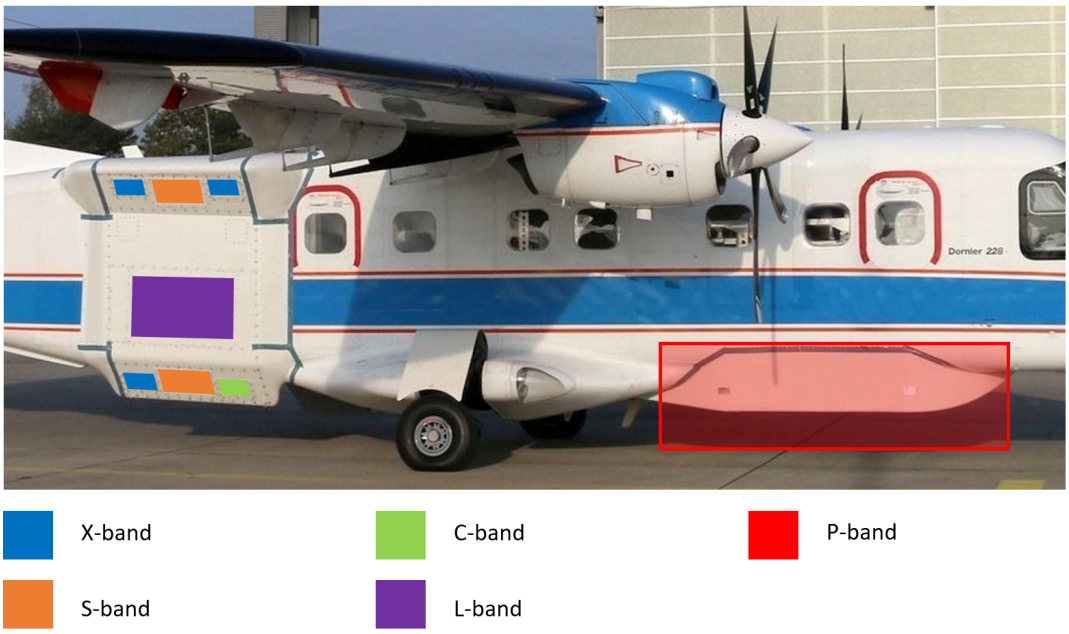

Figure 4.2 Antenna configuration of a fully equipped F-SAR system.

m and along track (ATI) for X-band with a baseline of ~ 0.85 m.
In order to keep the system at a sufficient performance the F-SAR has high standards for stability and precision. This requires a highly precise reference systems concerning the timing, i.e. for sampling, synchronization, and positioning. Furthermore, the system is constantly calibrated using different methods [15]:

Configuration	X	C	S	L	P	Endurance
F-SAR X-C-S-L	9.600 GHz	5.300 GHz	3.250 GHz	1.325 GHz	—	3.75-4.25 h
F-SAR P	—	—	—	—	0.435 GHz	4.0-4.5 h
F-SAR L	—	—	—	1.325 GHz	—	4.25-4.75 h
F-SAR L-P	—	—	—	1.325 GHz	0.435 GHz	3.5-4.0 h
F-SAR X-C-S-L-P	9.600 GHz	5.300 GHz	3.250 GHz	1.325 GHz	0.435 GHz	2.75-3.25 h

Table 4.2 possible F-SAR configurations with maximum endurance and operating center frequency f_0.

- The system uses the calibration test site in Kaufbeuren with the addition of 14 corner reflectors to calibrate the range- and azimuth positioning, as well as the resolution, the radar cross section and the polarimetric phase. The calibration process is repeated at least after each change in the antenna configuration, or after the de-/installation of an antenna.
- The system records a copy of the emitted signal before and after the mission for internal calibrations and to track possible changes in the antenna behaviour.
- The antennas can be calibrated in an indoor facility at DLR, called Compact Test Range (CTR), to record the antenna transfer functions from all angles and under consideration of possible surrounding conditions [20].

Exemplary missions for the variable utilization of F-SAR are amongst the generation of DEMs the *ARCTIC* mission (2015), where F-SAR was used over Greenland to investigate SAR capabilities in security applications and tested new methods for the snow parameter extraction, in addition. Another example of developing new techniques is the *AfriSAR* mission of 2016, where F-SAR contributed to develop the forest structure and biomass retrieval algorithms over the rainforest of Gabon for the BIOMASS mission, which is operated by the European Space Agency (ESA) and started in 2020. Additionally, thanks to its high flexibility, F-SAR was utilized in this mission to evaluate the capabilites of a satellite based SAR system in L- and P-band for future SAR mission concepts, i.e. the Tandem-L mission. The results in this thesis can be also listed under the development of new remote sensing methods, where F-SAR provided ideal capabilities to simulate a Staggered SAR like scenario, due to its high oversampling in azimuth direction.

5 Analysis and Results

In this section the performance of the DP-BAQ is analyzed for different SAR configurations. The goal is to validate the results from prior synthetic simulations and to evaluate the capabilities and functionality of the DP-BAQ on real Staggered SAR data. Since no present SAR system is capable of Staggered SAR acquisition the data had to be emulated with real airborne F-SAR data, which provides ideal conditions for a precise downsampling, due to its high oversampling. In order to ensure full functionality in the final analysis, three different configurations were tested as preparation: The results in the first section (5.1) focused on the verification of the results from Gollin [10] and the proof of a proper functionality of the algorithms on synthetic data. The quantization was evaluated by analyzing the resulting the image quality in terms of the SQNR. In the second scenario (section 5.2), the DP-BAQ was tested for the first time on real airborne SAR data, generated by the F-SAR system of DLR. In the last scenario in section 5.3, the oversampled F-SAR data was used in a preliminary test to create a more realistic spaceborne scenario and prove the full functionality of the DP-BAQ under spaceborne conditions with uniform sampling. Subsequently, the predictive quantizer was tested for its initial purpose in a Tandem-L-like scenario with non-uniform PRI and gaps in the raw data to prove the full functionality in a Staggered SAR-like scenario under realistic circumstances.

5.1 Synthetic scenario

The first test scenario included the analysis of the DP-BAQ, which was implemented according to the descriptions in chapter 3.5.4,applied on synthetic SAR data. The SAR signal was generated by multiplying the two way planar antenna pattern, which was calculated using the Tandem-L system parameters, with the azimuth angle dependent phase history. Subsequently, the resulting signal was convolved separately with both complex components of a normal distributed Gaussian noise according to (3.43). The real and imaginary part of the signal could be therefore assumed to be uncorrelated. An overview of the Tandem-L parameters can be seen in Table 5.1.

Parameter	Value
Orbit height	745 km (@ equator)
Carrier frequency, f_c	1.25 GHz (L band)
Range bandwidth	up to 84 MHz
Mean (staggered) PRF	2700 Hz
Doppler bandwidth, PBW	1130 Hz
Azimuth resolution	7 m
Swath width	175 km (quad) . . . 350 km (single/dual)
Raw data quantization	BAQ @ 4 bits per sample (bps)
Downlink capacity	~ 8 Terabyte/day
Reflector diameter	15 m

Table 5.1 Tandem-L system parameters.

The prediction weights for the LPC were calculated based on the planar antenna pattern of the Tandem-L system according to the calculation steps in section 3.5.2 and sampled at the PRF of 2700 Hz. The resulting autocorrelation curve, with the correlation of two subsequent samples marked in red, can be seen in Figure 5.1. The DP-BAQ was implemented according to the processing steps,

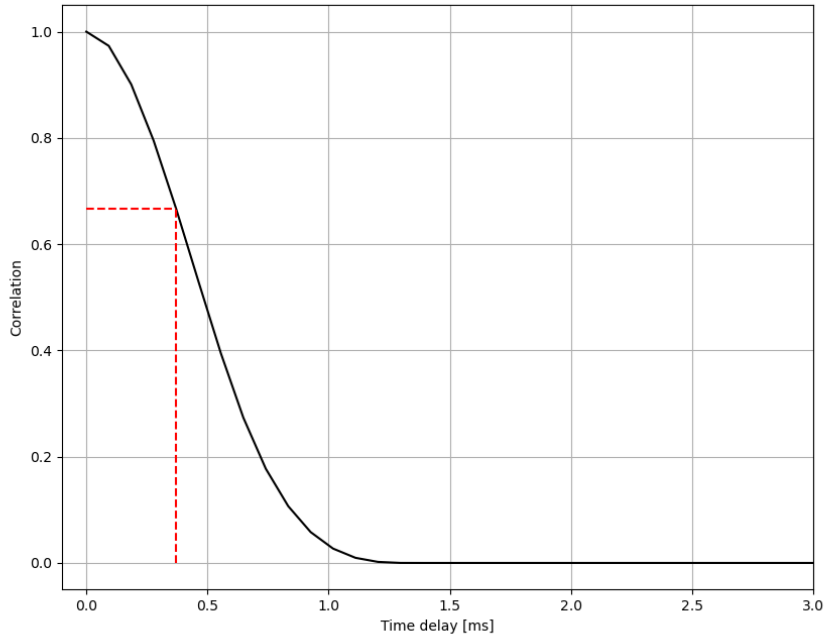

Figure 5.1 Autocorrelation for the Tandem-L system with an sampling rate of 2700 Hz. The value for the correlation between two subsequent samples ρ_1 is marked in red and corresponds to 0.667.

described in chapter 3.5.4, with a clipping value V_{clip} of 127.5 and -10 dB for the signal-to-clipping range γ_{clip}. Because of the uncorrelated properties of the SAR signals real and imaginary part, a cartesian quantizer was implemented, meaning that both complex parts were processed separately. The predictive quantizer was implemented for the first four prediction orders, according to the results of the analysis on the coding gain (3.49), which indicated no significant gain after the fourth order. The performance of the predictive quantizer was evaluated at different bit rates and compared to the corresponding results of a direct quantizer, i.e. a BAQ, to show the possibilities in data reduction. An overview of the implemented processing steps can be seen in Figure 5.2. As in the analysis of

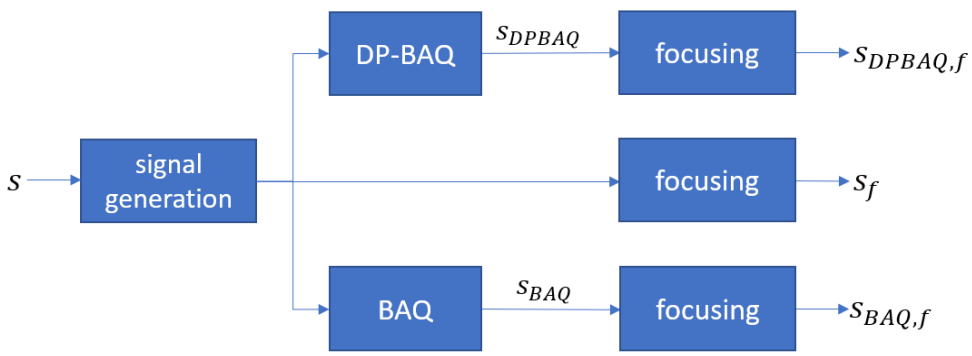

Figure 5.2 Process chain for Tandem-L scenario with simulated data.

the BAQ and ADC (Figure 3.6), the SQNR was taken as reference for the quality of the quantized

signal and calculated according to the formula in (3.15). For a better visualization of the results, the SQNR values were converted into dB according to

$$SQNR_{dB} = 10 \cdot \log_{10}\left(\frac{\sum_{i=1}^{N} |x_i|^2}{\sum_{i=1}^{N} |q_i|^2}\right), \tag{5.1}$$

with the quantization error $q_i = x_i - x_{q,i}$ calculated on the difference between each sample x_i of the original signal and the corresponding reconstructed one $x_{q,i}$. The SQNR plots for the first four orders, calculated on raw data can be seen in Figure 5.3, 5.4, 5.5 and 5.6. In order to visualize the actual gain that was introduced by the Linear Predictive Coding (LPC), the SQNR values of the DP-BAQ ($SQNR_{DP-BAQ}$) were directly compared to the BAQ values ($SQNR_{BAQ}$) in the absolute gain, which was calculated according to

$$\Delta_{SQNR} = SQNR_{DP-BAQ} - SQNR_{BAQ}. \tag{5.2}$$

Like the results in [10], the BAQ showed a constant behaviour over the changing sampling rate and introduced a gain of approximate 6 dB for each additional bit used in the quantization. The values of the SQNR for the DP-BAQ on the other hand, which are represented by the triangular marked lines, show an increase coherent with the increasing PRF, which validates the assumed better performance at higher correlation. Both values show consistent behaviour compared to the values of the work from Gollin [10], which proves the functionality of the predictors with simulated SAR data.
The plots for the absolute Gain of the DP-BAQ compared to the BAQ for the synthetic data can be seen in the Figures 5.7, 5.8, 5.9 and 5.10. All four plots show matching results with respect to the expected theoretical Gain in Figure 3.10, with the exception of the 2 bit sample.

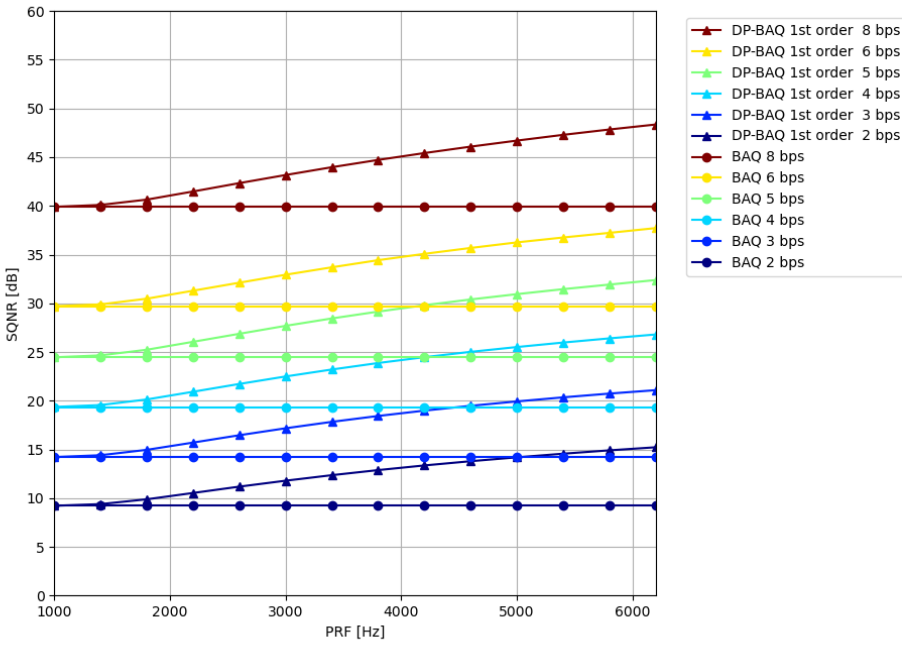

Figure 5.3 SQNR plot in dB of the first-order DP-BAQ and the corresponding BAQ for every bit-rate over different sampling rates (PRF).

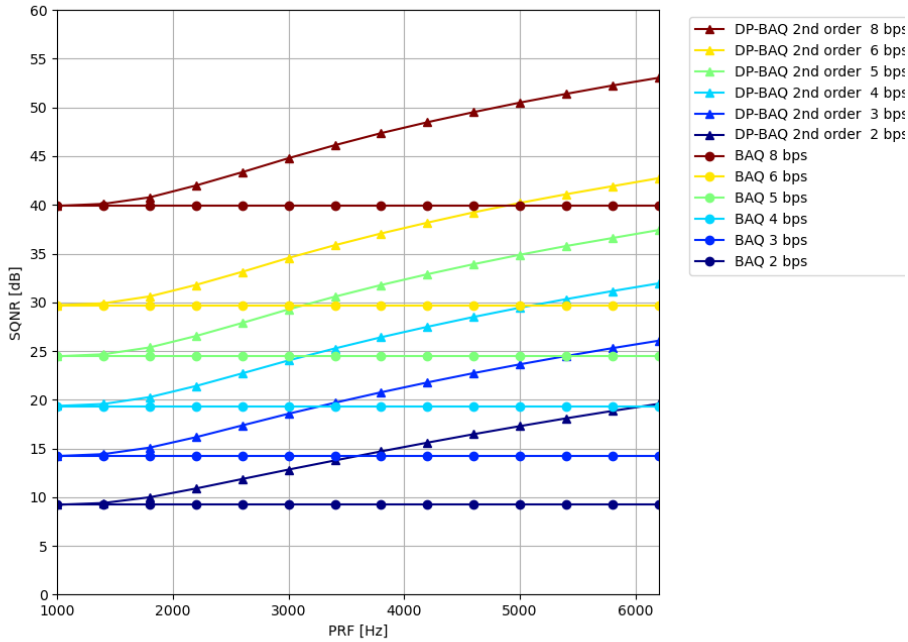

Figure 5.4 SQNR plot in dB of the second-order DP-BAQ and the corresponding BAQ for every bit-rate over different sampling rates (PRF).

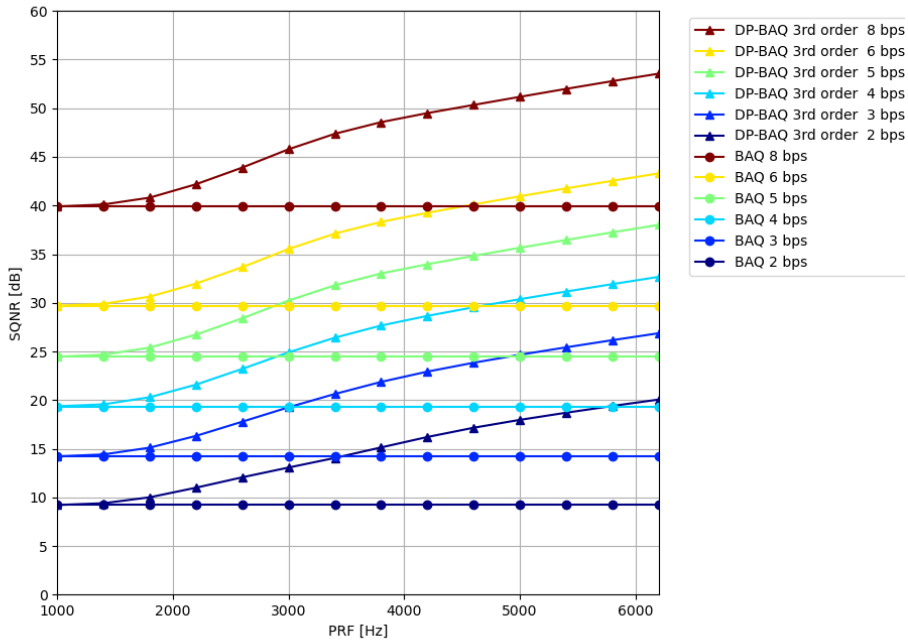

Figure 5.5 SQNR plot in dB of the third-order DP-BAQ and the corresponding BAQ for every bit-rate over different sampling rates (PRF).

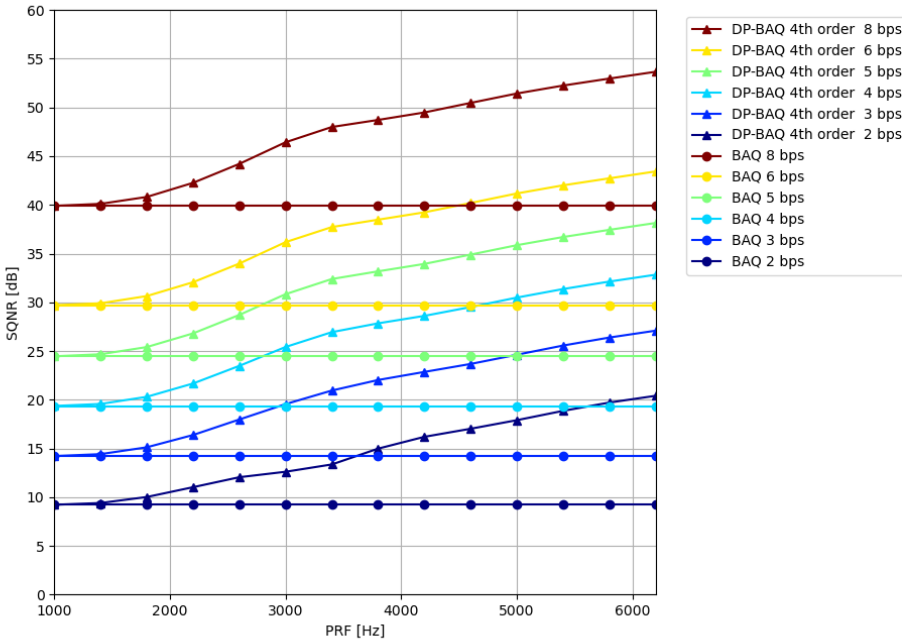

Figure 5.6 SQNR plot in dB of the fourth-order DP-BAQ and the corresponding BAQ for every bit-rate over different sampling rates (PRF).

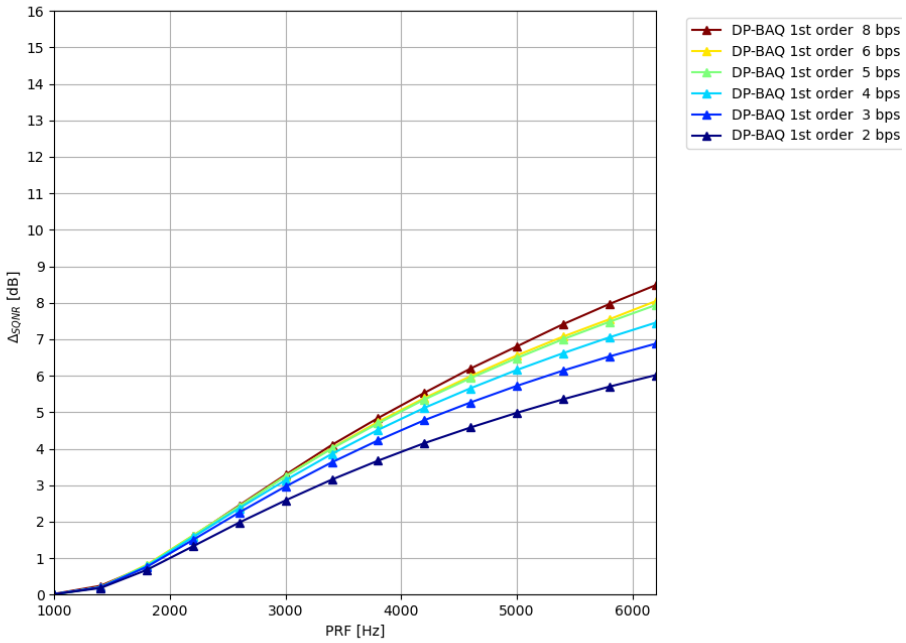

Figure 5.7 Absolute gain Δ_{SQNR} in dB of the first-order DP-BAQ and the corresponding BAQ for every bit-rate over different sampling rates (PRF).

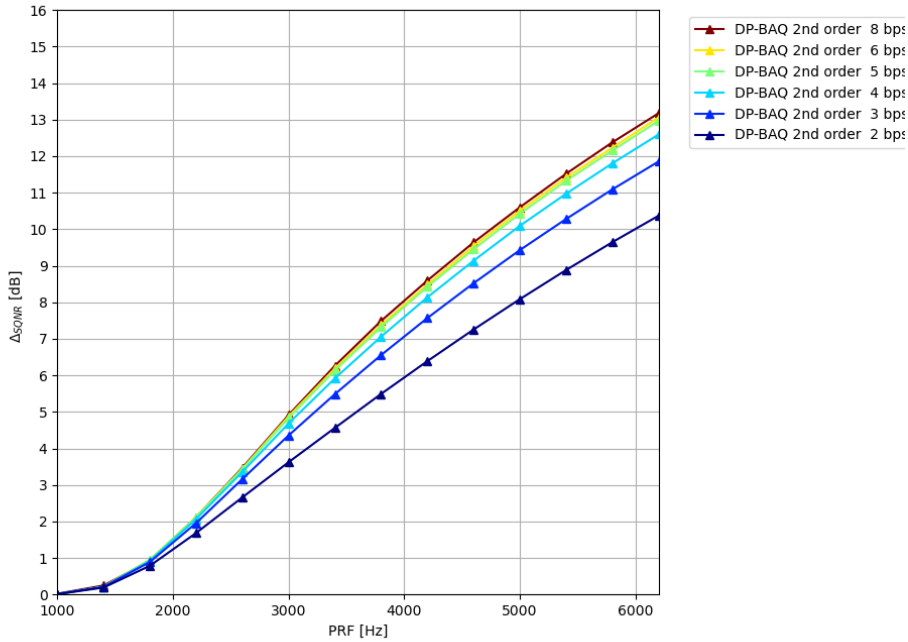

Figure 5.8 Absolute gain Δ_{SQNR} in dB of the second-order DP-BAQ and the corresponding BAQ for every bit-rate over different sampling rates (PRF).

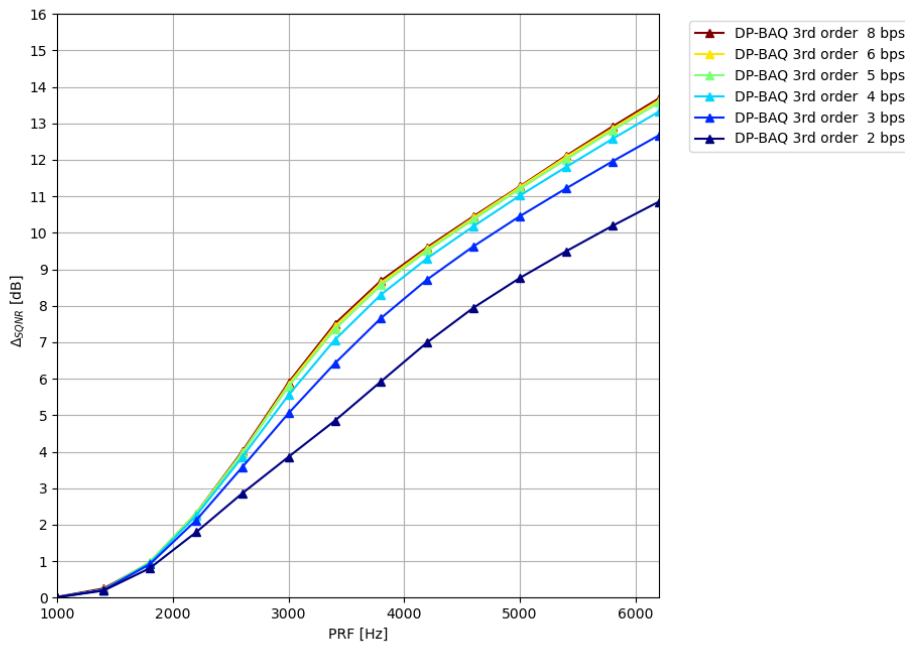

Figure 5.9 Absolute gain Δ_{SQNR} in dB of the third-order DP-BAQ and the corresponding BAQ for every bit-rate over different sampling rates (PRF).

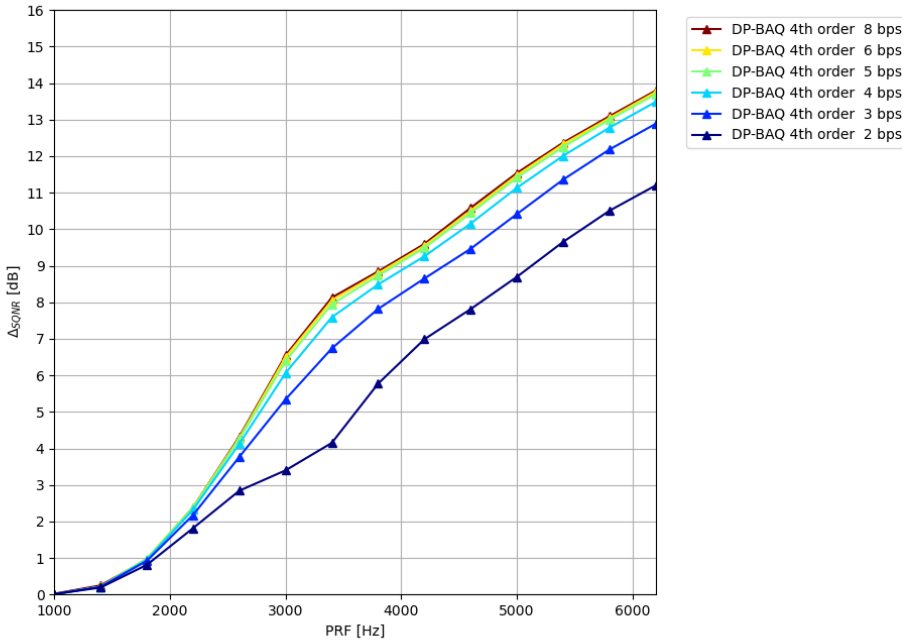

Figure 5.10 Absolute gain Δ_{SQNR} in dB of the fourth-order DP-BAQ and the corresponding BAQ for every bit-rate over different sampling rates (PRF).

5.2 Direct application on oversampled real F-SAR data

Since the functionality of the DP-BAQ was shown for synthetic data in the previous section, this section describes the first implementation of the DP-BAQ on real SAR data, as preparation for the final analysis on the spaceborne system. The F-SAR system generates highly oversampled SAR images in azimuth direction, due to its comparably low velocity. Thus, it provides ideal properties to test the predictive coding and the gain achieved by the DP-BAQ on F-SAR data was expected to be extremely high. The F-SAR image, processed in the following analysis, was acquired over the test site in Kaufbeuren in south Germany. The land site was chosen, due to its varying surface properties, including lakes, urban areas, forest and grass land, which made it ideal for testing the performance on different backscatter properties.
The image was provided as a range focused SAR signal, sampled at a PRF of 2500 Hz in azimuth direction at a processed Doppler Bandwidth B_D of 132.21 Hz, providing an azimuth oversampling factor σ_f calculated as

$$\sigma_f = \frac{PRF}{B_D}, \tag{5.3}$$

of ~ 18.91. For comparison the same factor for the Tandem-L scenario is only 2.39.

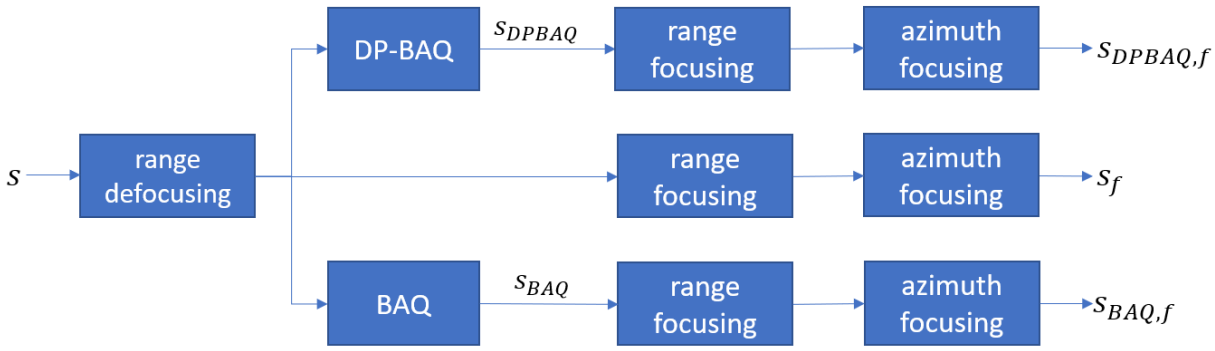

Figure 5.11 Processing chain for F-SAR quantization test.

An overview of the required processing steps for the analysis can be seen in Figure 5.11. Since the quantization is always applied on raw data, the SAR image had to be at first range de-focused, which was done by convolving the focused image by the complex conjugate of the time reversed range chirp, generated according to (2.14) and the F-SAR acquisition parameters in Table 5.2.
The autocorrelation for the LPC was calculated on the provided antenna pattern according to the equations in section 3.5.2, by convolving the squared pattern with a Gaussian noise and calculating the correlation values from the inverse Fourier transformation of the power spectral density. Unlike the calculations for the synthetic data, the pattern was already pre-calculated as a three-dimensional pattern in order to properly consider each scatterer, with axes for the squint angle, i.e. the azimuth angle, the off-nadir angle, i.e. the elevation and the center frequency f_0. The resulting autocorrelation for a center frequency $f_0 = 1.325$ GHz and a mid range antenna pattern can be seen, sampled at a PRF of 2500 Hz in Figure 5.12.
The correlation value between two subsequent samples is again marked in red and is, by comparing it to the Tandem-L correlation in Figure 5.1 significantly higher, which was already expected, due to the high oversampling.
In order to sufficiently consider the different signal statistics, which were varying over the range, the

Parameter	F-SAR
Orbit height	3 km
Carrier frequency, f_c	1.325 GHz (L band)
Range bandwidth	150 MHz
Mean (staggered) PRF	2500 Hz
Processed Doppler bandwidth, PBW	132 Hz
Reflector diameter	0.65 m
looking angle	15-90 °
sensor velocity	$90.1\mathrm{m/s}$

Table 5.2 F-SAR system parameters

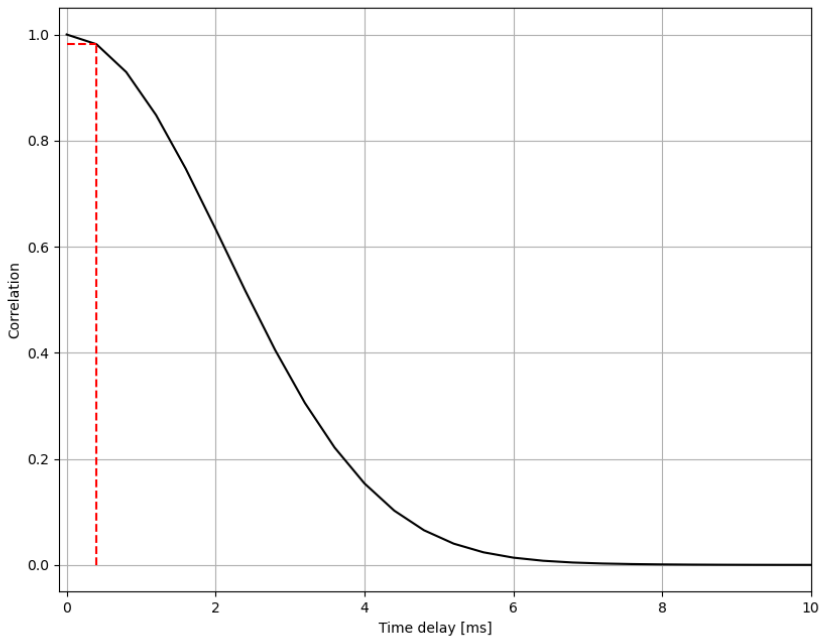

Figure 5.12 Autocorrelation for the FSAR system with an sampling rate of 2500 Hz.The value for the correlation between two subsequent samples ρ_1 is marked in red and corresponds to 0.982.

original image was split into blocks of 128 consecutive azimuth lines and the correlation calculated on the center azimuth line of each block. In this way the predictor was able to consider the individual signal statistics properly, without increasing the complexity of the quantization process too much. A plot of the different correlation for each range block can be seen in Figure 5.13. The difference between the correlation values might not seem significant, especially at small time delays, but due to the inversion of the C matrix during the weights derivation even such small differences have a significant impact on the calculated values for β_i.

After the de-focusing of the SAR image and preparation of the prediction parameters, the DP-BAQ was applied on the raw SAR data. The performance was again investigated for the first four orders of the DP-BAQ at different bitrates as well as a BAQ for reference. Subsequently the quantized images were reconstructed and focused according to section 2.1.2. The performance was again evaluated by means of the SQNR, which was calculated according to 5.1, and the absolute gain according to (5.2).

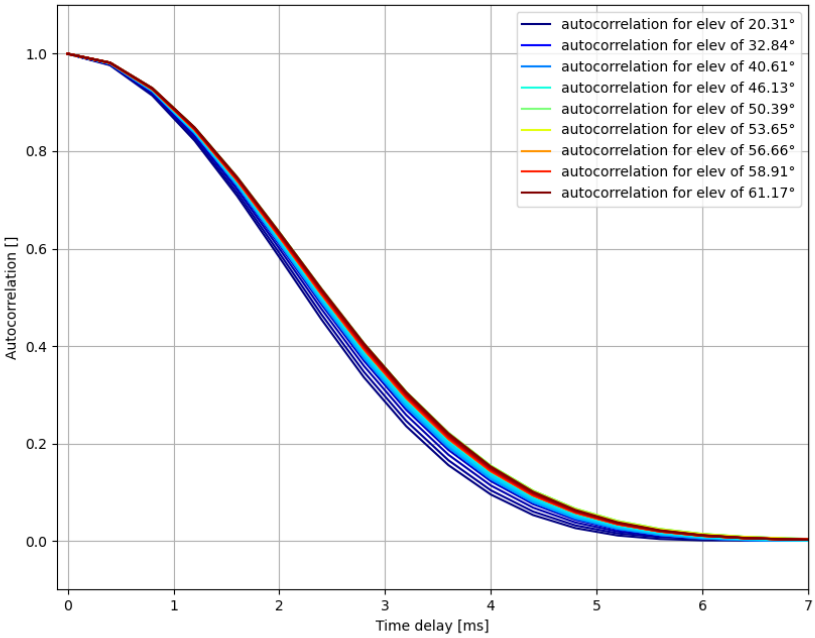

Figure 5.13 Autocorrelation of F-SAR signal at different elevation angles.

The corresponding plots for SQNR and absolute Gain Δ_{SQNR} of all orders, calculated on the range-focused data can be seen in Figure 5.14 and 5.15. The values for the first two orders grow constantly and show the expected behaviour of gaining 6 dB for each additional bit in the quantization and high absolute gain of up to 22 dB. Compared to the BAQ the second order predctor perform at 3 bit already better than the BAQ at 4 bit, providing a data reduction rate of over 70%. Additionally, the calculated absolute gain of the first two orders, shows matching results with the theoretical gain in Figure 3.10. The results of the 3rd and 4th order, on the other hand, show strong variations in the SQNR plots, or instability during the quantization, which corresponds to the non-existend SQNR values in the plot.

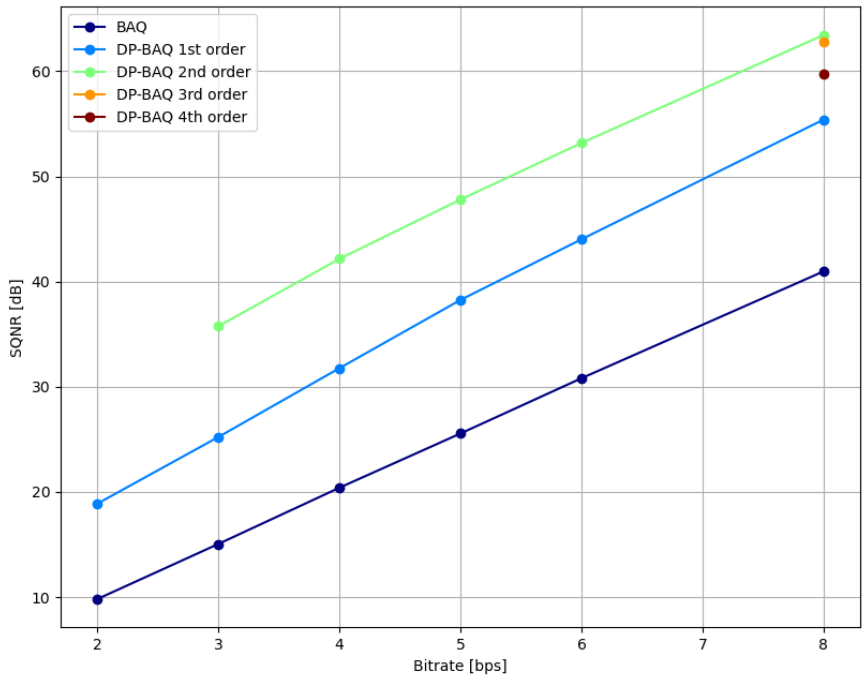

Figure 5.14 SQNR in dB for all prediction orders of the DP-BAQ on raw data after range focusing.

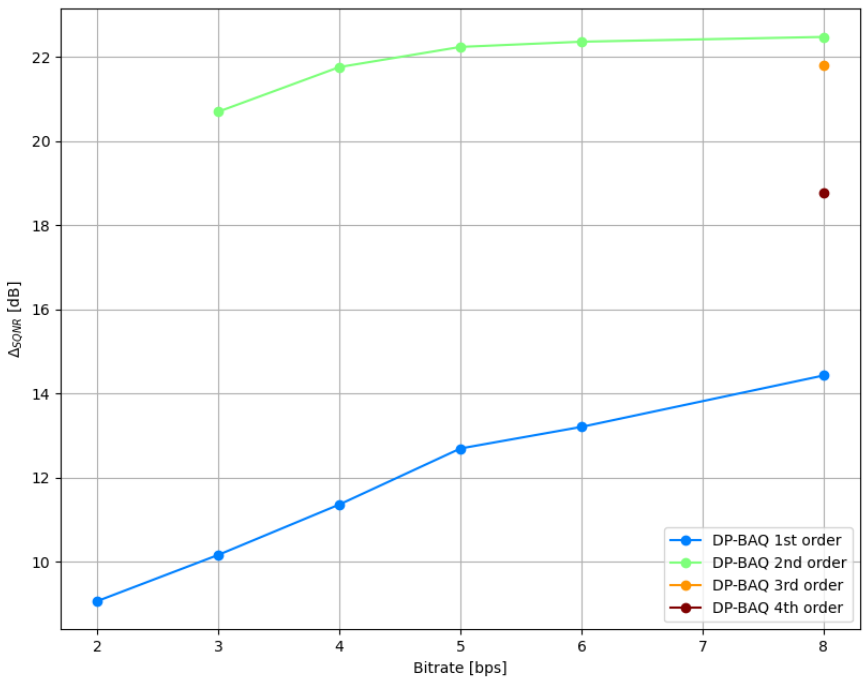

Figure 5.15 Absolute gain Δ_{SQNR} in dB for all prediction orders of the DP-BAQ on raw data after range focusing.

The corresponding plots for the SQNR values and absolute Gain of the fully focused SAR images can be seen in the Figures 5.16 and 5.17. As it becomes apparent, the performance of the DP-BAQ does not change much and shows constantly better performance for the stable cases. The main difference can be seen in the absolute gain plot after full SAR focusing, where the azimuth focusing limits the maximum performance of higher bit rates. Despite that, the resulting image quality is still at performance levels far higher than direct quantizer.
The instabilities for higher prediction orders can be explained by the high oversampling of the data

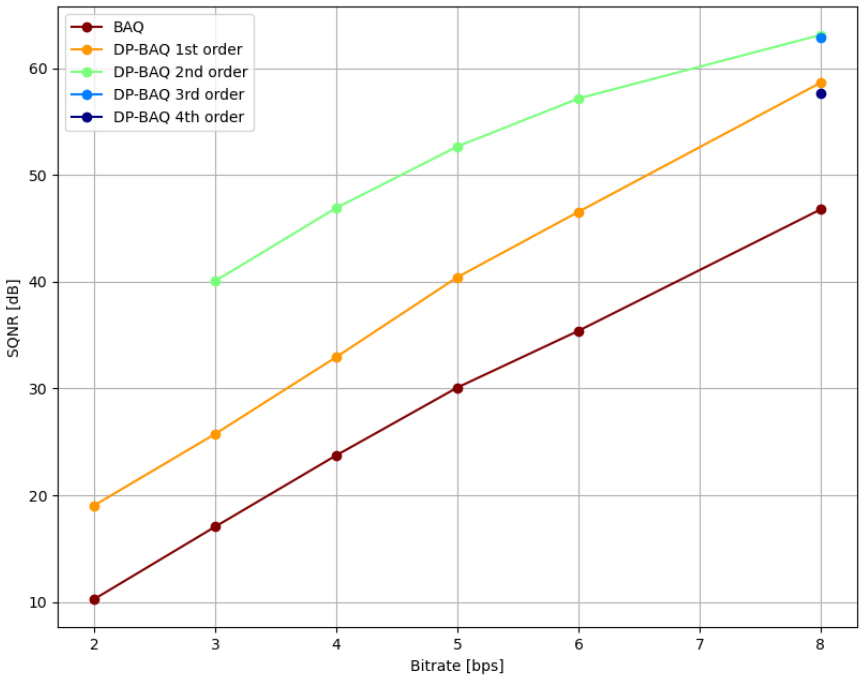

Figure 5.16 SQNR in dB for all prediction orders of the DP-BAQ on raw data after full focusing.

in azimuth direction. Due to the high correlation between subsequent samples in the F-SAR data, the predictor manages to estimate the signals with a high accuracy, resulting in a extremely low dynamic of the prediction error. At a given point the prediction is so precise, that the contribution of the quantization error changes the quantized prediction error significantly. The direct consequence is that the predictor starts to calculate wrong predictions, which lead to the constant decrease in performance of the DP-BAQ. The error keeps growing until it reaches a size where the scaling factor α reaches zero, which automatically results in a mathematical error, i.e. division by zero, in the calculation.
The effects described above were visualized by the error ratio Δ_{error} between the prediction error power σ^2_{pred} and the quantization error power σ^2_{quant} according to

$$\Delta_{error} = 10 \cdot \log_{10}\left(\frac{\sigma^2_{pred}}{\sigma^2_{quant}}\right). \tag{5.4}$$

The ratio was analyzed at different sampling rates (PRF) in order to investigate the behaviour of the DP-BAQ at lower correlated signals and to find the ratio, where the signal starts degrading. The resulting plots for the first four orders can be seen in the Figures 5.18, 5.19, 5.20 and 5.21. When comparing the plots of the first two orders with the plots of the last two orders one can clearly see that the first order ratio falls much slower: Even though the first order ratio is slightly worsening for

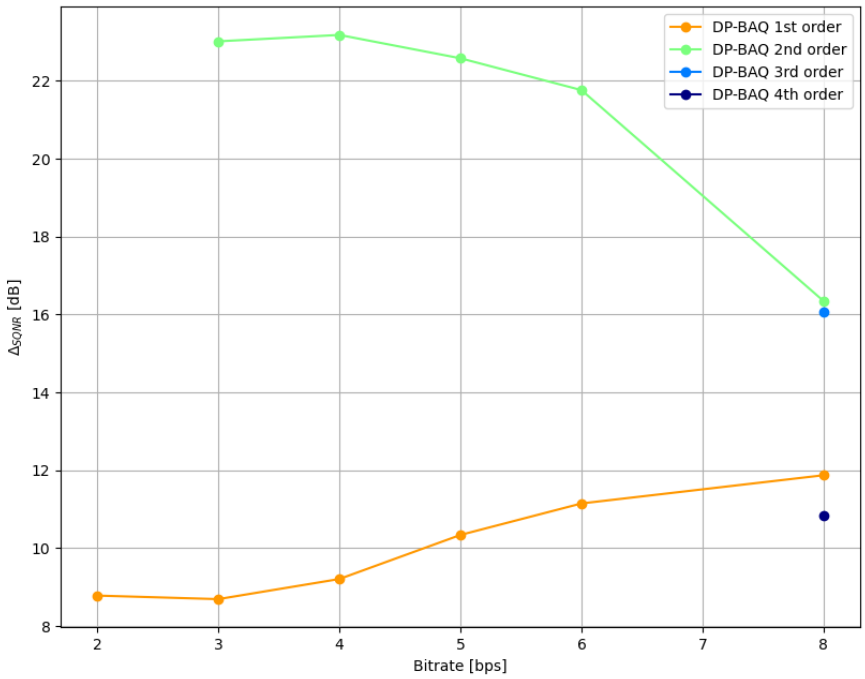

Figure 5.17 Absolute gain Δ_{SQNR} in dB for all prediction orders of the DP-BAQ on raw data after full focusing.

higher correlation, i.e. PRF, it stays stable over the whole PRF range and never reaches the point, where the quantization error exceeds its critical value. The same can be said for the 2nd order ratio, the values stay mostly in a reasonable range and the results are not corrupted too severely, which can be also seen in the SQNR plots. For the last two plots on the other hand the ratio decreases very quickly and results into strongly corrupted files after a PRF of 1 kHz at most, with the exception of the 8 bps cases which were able to cope the low signal dynamic due to their high resolution in the quantization space.

The results show that the DP-BAQ works in general for real SAR data. The unstable results at higher prediction orders are acceptable for the F-SAR scenario, since the DP-BAQ was originally designed for spaceborne systems, where the correlation, i.e. oversampling, is much smaller. A more realistic configuration of a SAR system, considering future applications of the DP-BAQ is presented in the following section.

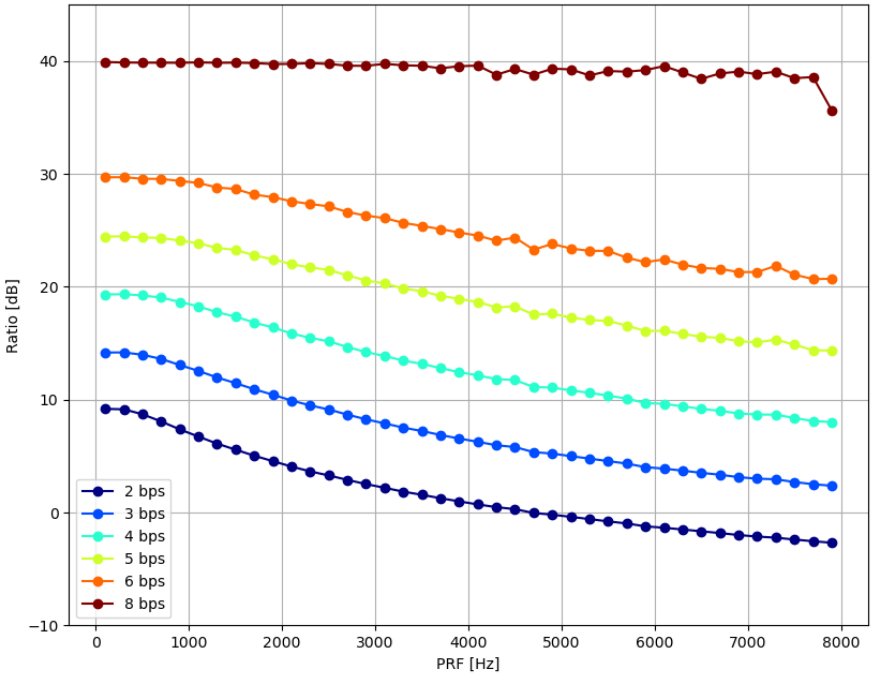

Figure 5.18 Ratio between the power of the prediction error σ^2_{pred} and the quantization error power σ^2_{quant} of the first order DP-BAQ for different PRF.

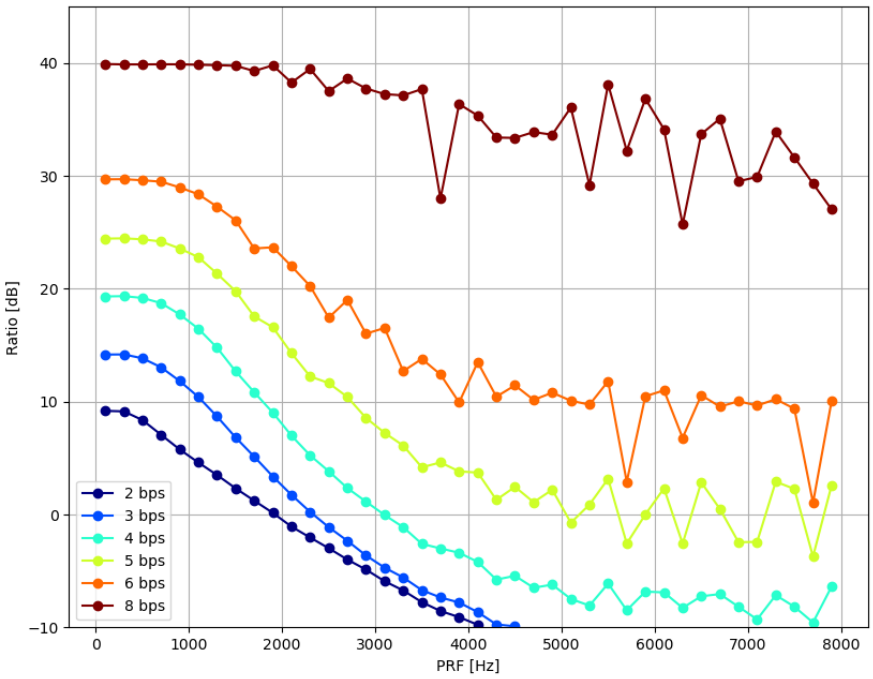

Figure 5.19 Ratio between the power of the prediction error σ^2_{pred} and the quantization error power σ^2_{quant} of the second order DP-BAQ for different PRF.

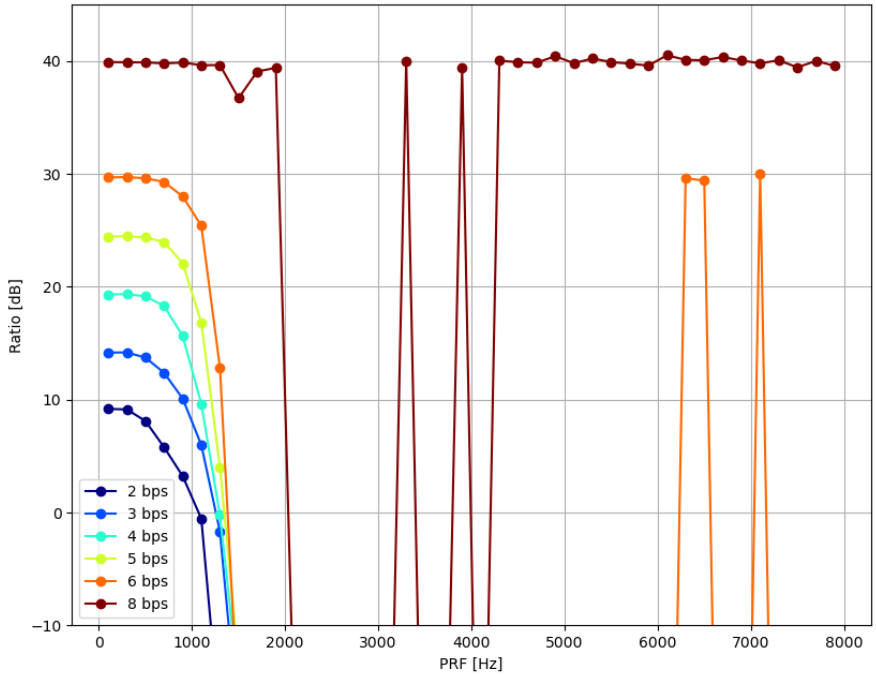

Figure 5.20 Ratio between the power of the prediction error σ^2_{pred} and the quantization error power σ^2_{quant} of the third order DP-BAQ for different PRF.

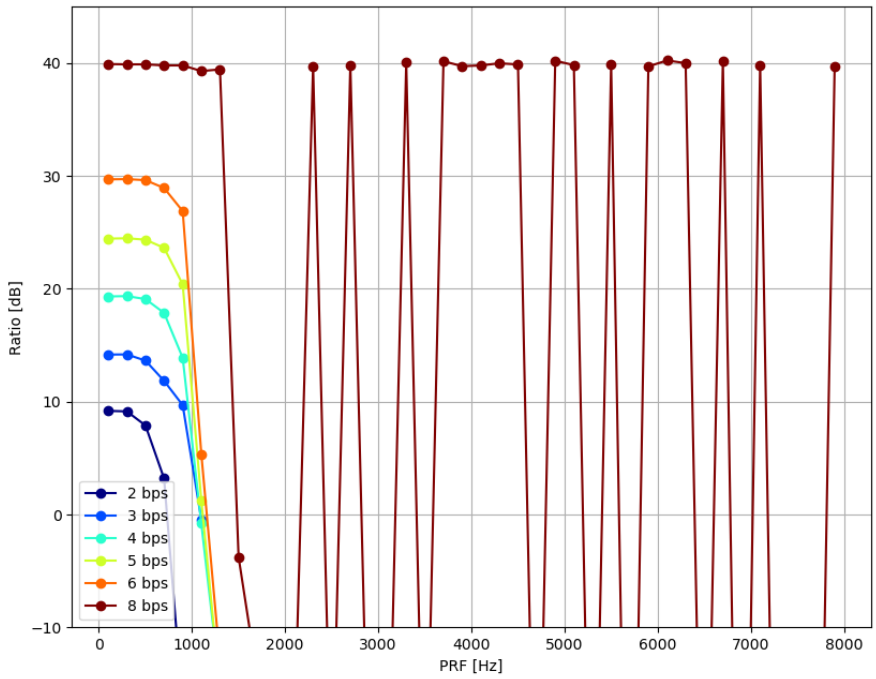

Figure 5.21 Ratio between the power of the prediction error σ^2_{pred} and the quantization error power σ^2_{quant} of the fourth order DP-BAQ for different PRF.

5.3 Equivalent spaceborne simulation with real F-SAR data

After verifying the functionality of the DP-BAQ applied on real SAR data, the performance could be investigated for its initial purpose, the application on staggered SAR. The simulation of a spaceborne Staggered SAR like scenario with proper signal statistics required the downsampling of the original F-SAR data to a lower PRF. In order to ensure full functionality for the more complicated Staggered SAR case, the analysis was split in two separate processing steps. In a preliminary analysis, an ordinary downsampling process and full functionality of the DP-BAQ under spaceborne conditions with real SAR data should be developed. The following analysis consequently included the full implementation and analysis of the DP-BAQ applied on spaceborne Staggered SAR data.

5.3.1 Constant PRI

To ensure the full functionality of the DP-BAQ on real spaceborne SAR data, as well as to validate the signal generation steps, which were necessary to generate a Staggered SAR set, the DP-BAQ was tested on an uniformly sampled set it advance.

PRI selection

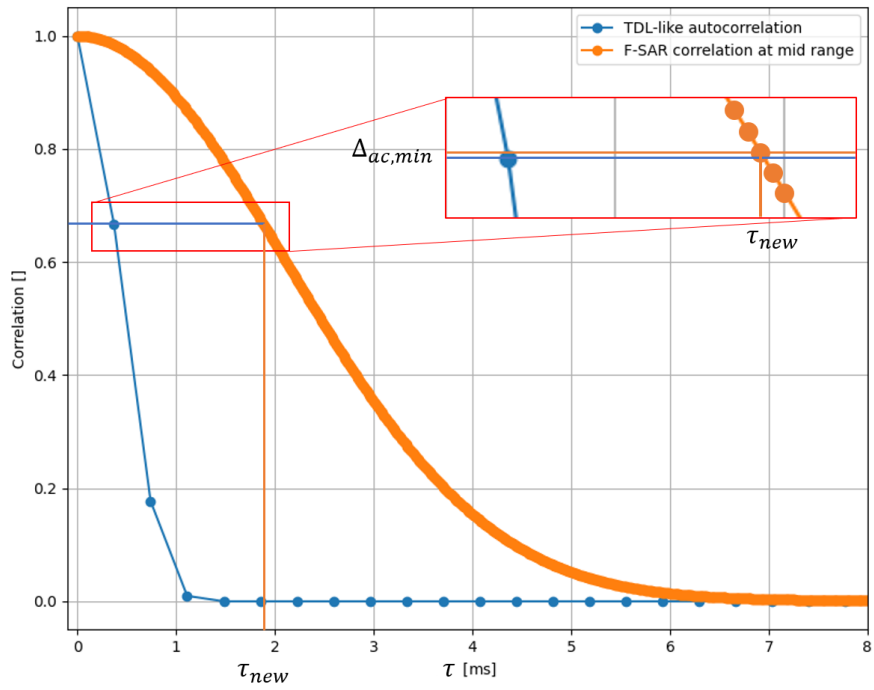

Figure 5.22 Comparison of the Tandem-L correlation (blue), sampled at 2700 Hz and the oversampled F-SAR correlation (orange) at a PRF of 100 kHz.

In order to generate a SAR acquisition with spaceborne SAR signal properties, the F-SAR data required further processing. As already stated in previous chapter, F-SAR data is much higher correlated, i.e. oversampled, in azimuth direction, which exceeds the possible correlation observed between spaceborne samples by far. A possible way to reduce correlation is to increase the time steps between subsequent samples, or equally said, to resample the original data at a lower PRF. In order to get a signal as close as possible to that of a spaceborne SAR, the sampling rate was selected with reference to the Tandem-L correlation. Thereby, the correlation between two subsequent

samples ρ_1 of Tandem-L at a selected PRF was compared to the values of an oversampled F-SAR correlation, which can be seen as exemplary plot in Figure 5.22. The plot shows the Tandem-L correlation for the system parameters according to Table 5.1 and its mean staggered PRF of 2700 Hz ($\rho_1 \sim 0.667$), as well as the oversampled F-SAR correlation. For the calculation of the new sampling rate, the value with the smallest difference to the Tandem-L correlation was chosen and the related time delay used for the definition of the PRI. In doing so, the oversampled autocorrelation ensured high precision in the adjustment of the resampled autocorrelation.

Analysis and results

The processing steps, which were necessary to generate and process a spaceborne-like signal are shown in Figure 5.23. After the range defocusing of the F-SAR data the F-SAR image was

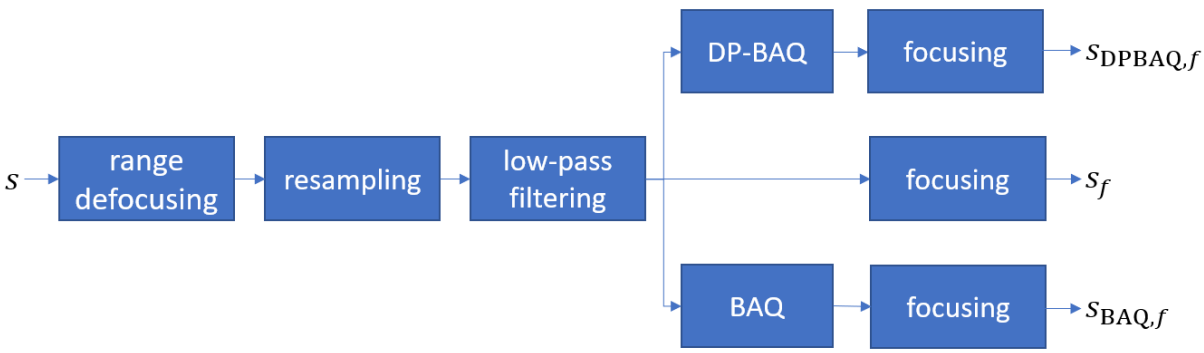

Figure 5.23 Process chain for spaceborne SAR quantization at a constant PRI.

resampled at a lower constant PRF, in order to generate a data set with similar correlation, i.e. performance, to a non-staggered spaceborne SAR. The new PRI for resampling the F-SAR data was calculated according to the processing steps in the first subsection of 5.3.1. Thereby, the calculation was based on the Tandem-L system parameters of Table 5.1 and a sampling rate of 2700 Hz, which corresponds to the mean PRF of the staggered case for the main analysis. Figure 5.24 shows the resulting F-SAR correlation for the calculated sampling rate of ~ 532 Hz (PRI = 1.88 ms) and the Tandem-L correlation. To avoid an interpolation, the sampling frequency was chosen as the next higher fraction of the original PRF of 2500 Hz, which corresponded for 532 Hz to 625 Hz. The reason to round to the next higher value was to ensure full functionality of the staggered SAR, since the higher correlations proved to be more critical than the lower ones in the previous analysis with the direct implementation. After the downsampling of the SAR image, a low-pass filter was applied at the new PRF, to remove further noise sources.
Subsequently, the resulting SAR image was quantized by the DP-BAQ and the BAQ for reference. The resulting plots for the SQNR and absolute Gain Δ_{SQNR} of the quantized signals after range focusing can be seen in Figure 5.25 and 5.26.

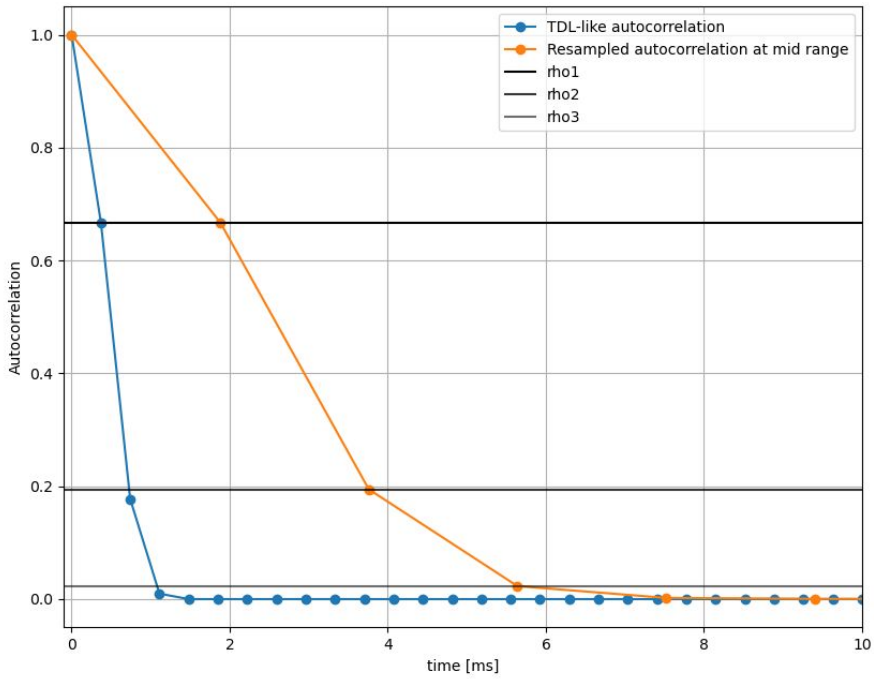

Figure 5.24 Comparison of the Tandem-L correlation (blue), sampled at 2700 Hz and the F-SAR correlation (orange), sampled at the chosen PRI of 1.88 ms (~ 532 Hz).

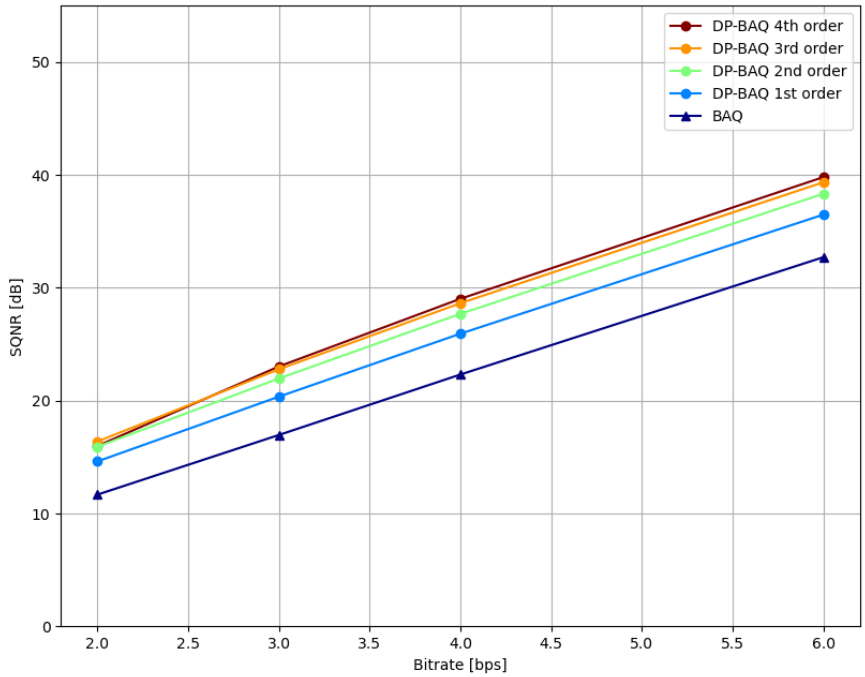

Figure 5.25 SQNR for the Tandem-L-like data set based on real F-SAR data after range focusing.

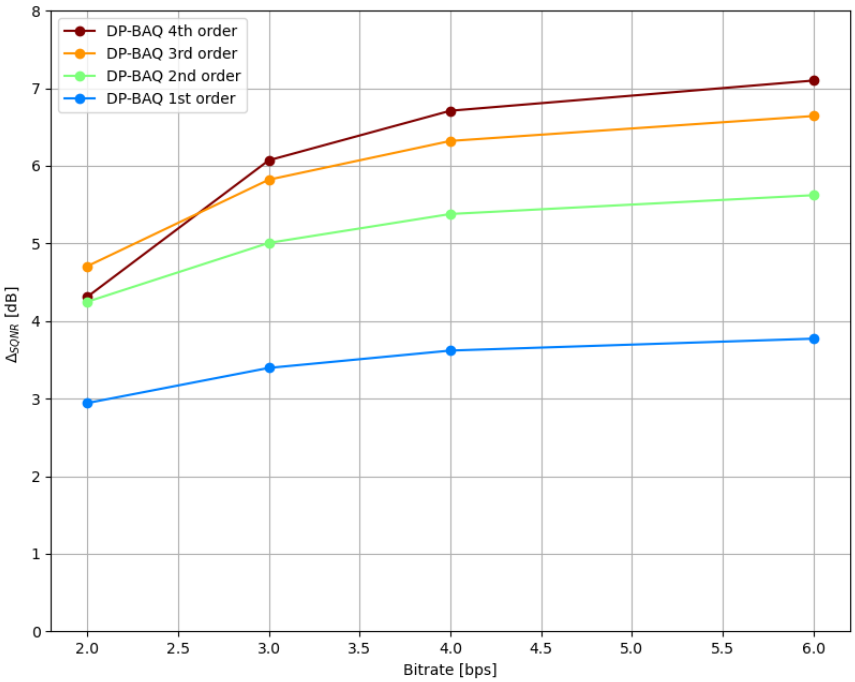

Figure 5.26 Absolute gain Δ_{SQNR} for the Tandem-L-like data set based on real F-SAR data and constant PRI after range focusing.

When comparing the results of the DP-BAQ with the BAQ, it becomes apparent, that the 3 bps quantization from the second order on performs already as good as a 4 bps BAQ. The third order 3 bps case performs even better than the corresponding BAQ at 4 bits. Furthermore, the BAQ as well as the DP-BAQ show the average gain of about 6 dB per additional bit. In total, the quantizer shows a little better performance compared to the results in [10], thanks to the higher correlation caused by the increased sampling rate. The direct impacts can be seen in the better performance of the 3 bit predictive case compared to the 4 bit case of the BAQ, as well as the increased gain compared to the BAQ which reached around 6 dB instead of 4 dB for a third order predictor. The observed results do not change for the fully focused results of the DP-BAQ in Figure 5.27. The final

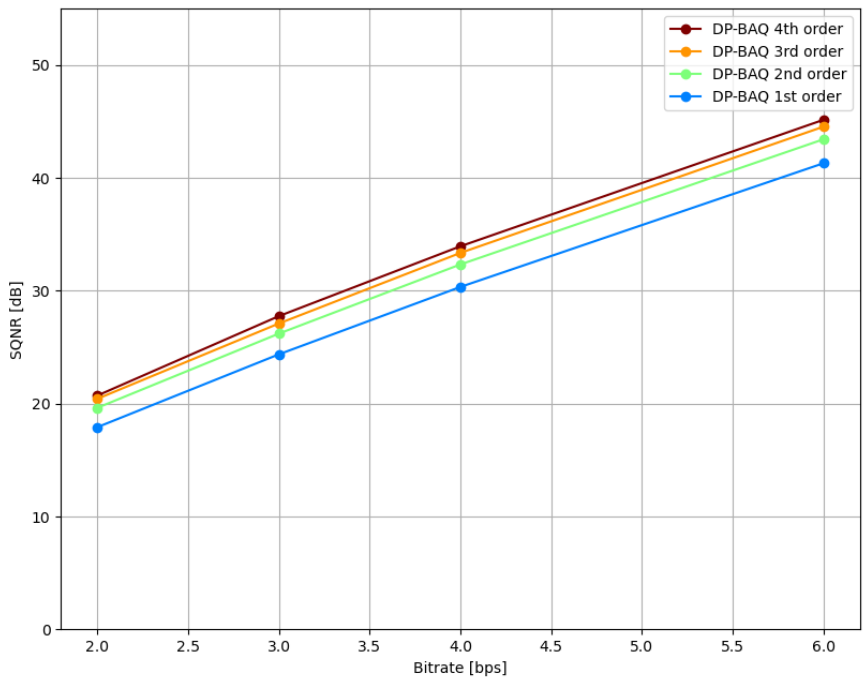

Figure 5.27 SQNR for the Tandem-L-like data set based on real F-SAR data and constant PRI after full SAR focusing.

plots of this section show the histograms for the SQNR values of each pixel calculated on the fourth order predictor at all available bit rates. The average gain of 6 dB per additional bit is clearly visible in the plots as well as the constant shape of the distribution, which suggests similar performance of the different regions over time. The consistent performance as well as the matching with the expected behaviour proved, that the DP-BAQ is applicable on a spaceborne system with a constant PRI similar to the mean PRI of a staggered SAR system. Furthermore, it confirmed the results from the prior section that the DP-BAQ only degenerates at high correlation values, since the new sampling rate of the F-SAR at 625 Hz, which was well below the critical frequency ranges, showed normal performance at all prediction orders. To ensure the full functionality an additional analysis was conducted by repeating the test set of section 5.1. The resulting plots can be seen in Figure 5.32 and show consistent results with exception of the 2 bit case of the fourth order, which overlaps with the error ratio analysis in section 5.2. Furthermore, the plots proof the results of the synthetic analysis, as they show the same performance results.

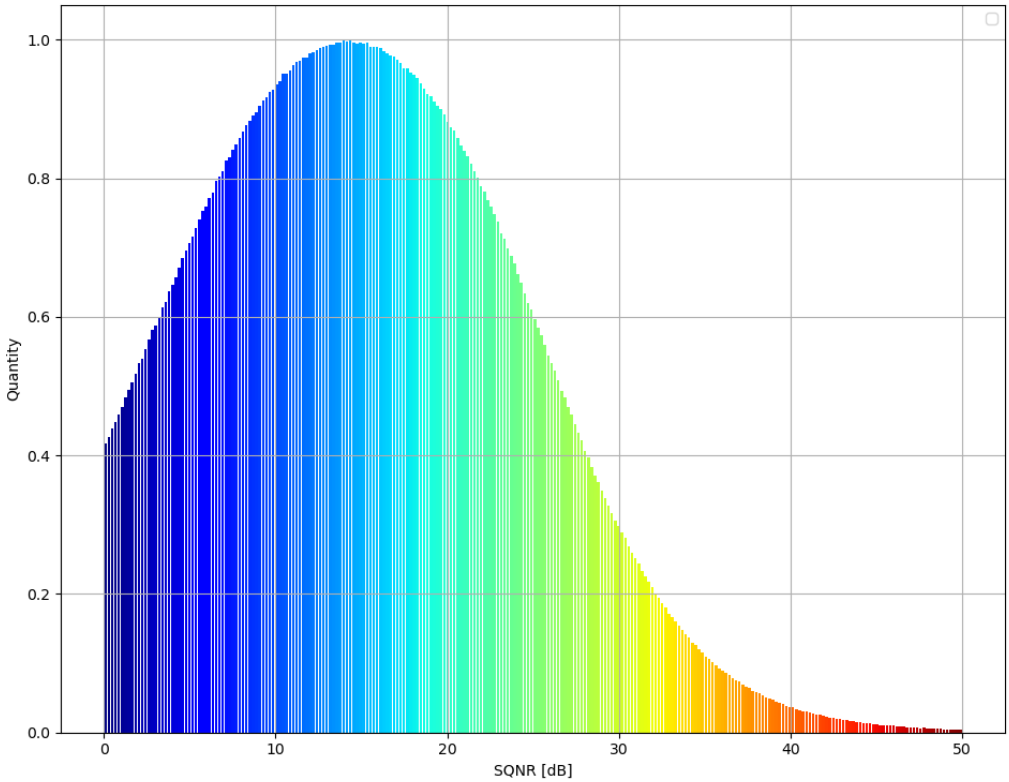

Figure 5.28 Histogram of SQNR values calculated on each pixel of the Tandem-L-like data set at constant PRI for the fourth order and 2 bps after full focusing.

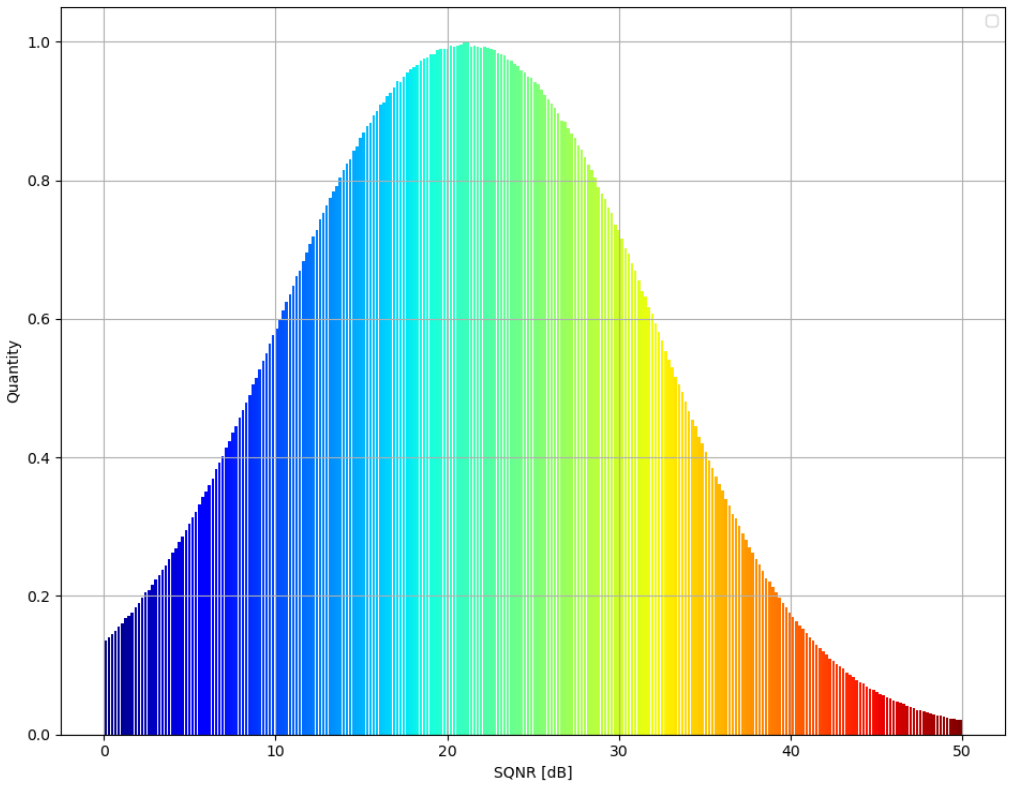

Figure 5.29 Histogram of SQNR values calculated on each pixel of the Tandem-L-like data set at constant PRI for the fourth order and 3 bps after full focusing.

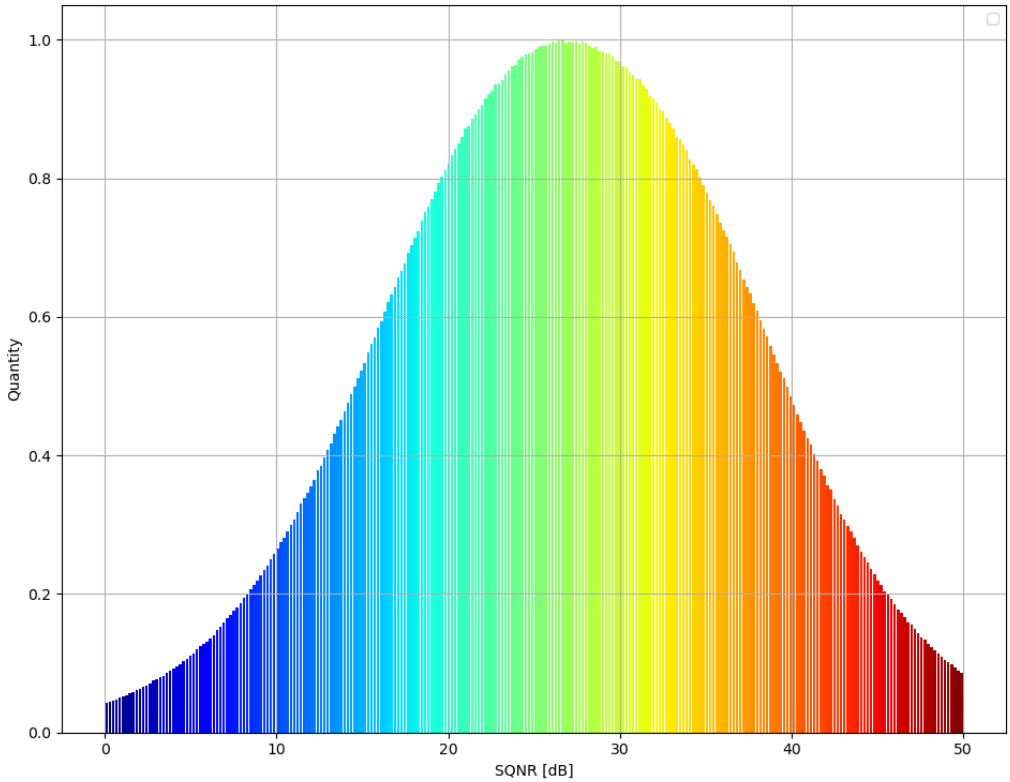

Figure 5.30 Histogram of SQNR values calculated on each pixel of the Tandem-L-like data set at constant PRI for the fourth order and 4 bps after full focusing.

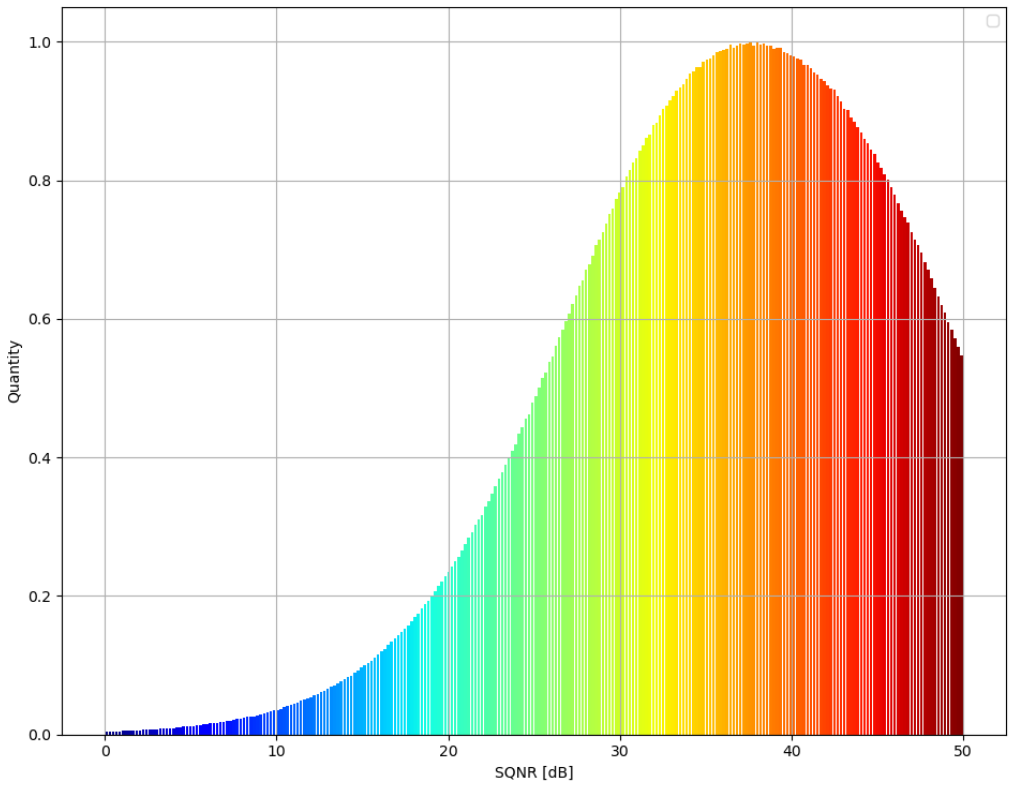

Figure 5.31 Histogram of SQNR values calculated on each pixel of the Tandem-L-like data set at constant PRI for the fourth order and 6 bps after full focusing.

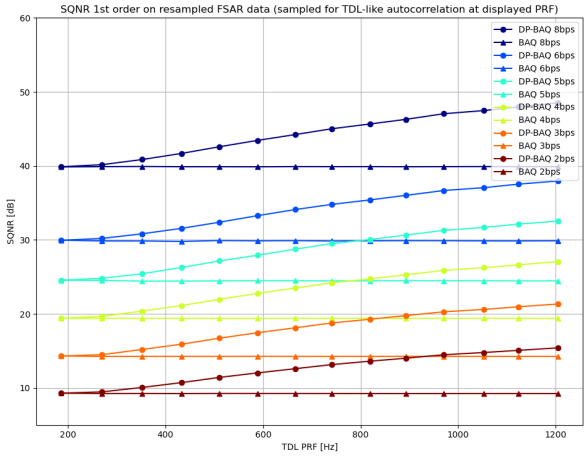

(a) SQNR plot for first order DP-BAQ on resampled F-SAR data.

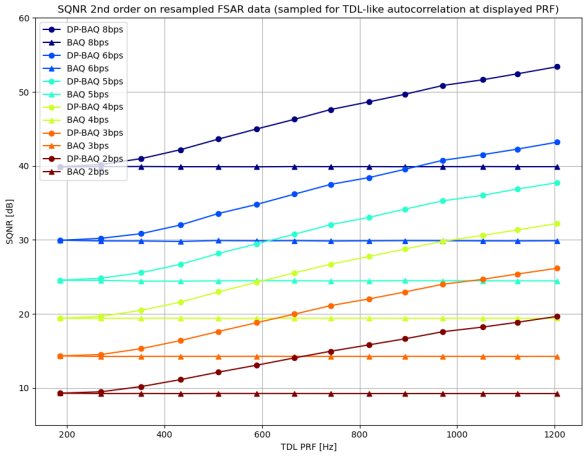

(b) SQNR plot for second order DP-BAQ on resampled F-SAR data.

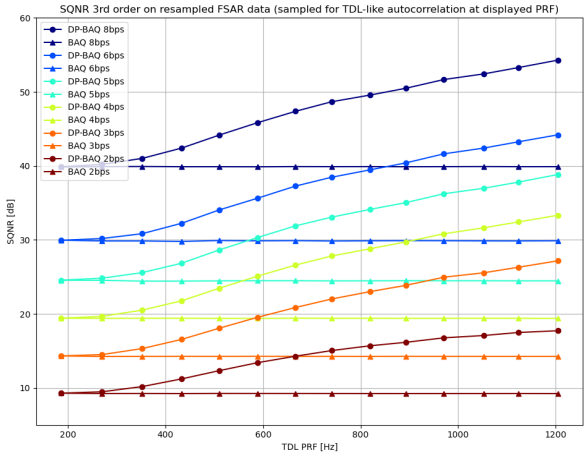

(c) SQNR plot for third order DP-BAQ on resampled F-SAR data.

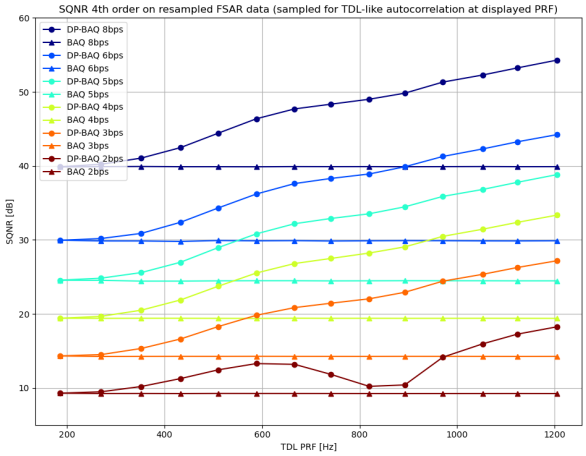

(d) SQNR plot for fourth order DP-BAQ on resampled F-SAR data.

Figure 5.32 SQNR plot for all order of the DP-BAQ on resampled F-SAR data.

5.3.2 Staggered PRI

The results of prior sections proved the full functionality of the DP-BAQ on real raw SAR data in a spaceborne scenario, as well as the full functionality of the downsampling method. This leads to the analysis of the DP-BAQ on staggered SAR data, which also represents the main analysis of this thesis.
The data for the performance analysis were generated, as in the previous section based on real F-SAR data. The main difference between the preceding analysis and this one was the the presence of gaps in the raw data matrix, as well as a non-constant PRI, due to the system properties of Staggered SAR. Therefore, the DP-BAQ had to be adjusted to the gaps accordingly, as described in section 3.5.4. After the quantization Best Linear Unbiased (BLU) interpolation was used to resample the staggered signal at a uniform PRI [32], [30]. This interpolation method exploits the correlation between subsequent samples to reconstruct the values at the interpolation steps. BLU interpolation requires a certain correlation of the data samples, like in Tandem-L or F-SAR data, to be able to reconstruct the missing data in a gap position, which would lead to significant errors in common interpolation methods.
In addition to the signal reconstruction by the BLU interpolator the signal needed to be resampled at a fractional PRF of the original sampling rate of F-SAR for a proper azimuth focusing. An overview over the processing steps to generate the signal can be seen in Figure 5.33 and for the quantization and reconstruction in Figure 5.34.
In the first step the signal needed to be resampled at a PRF, which provided a correlation between

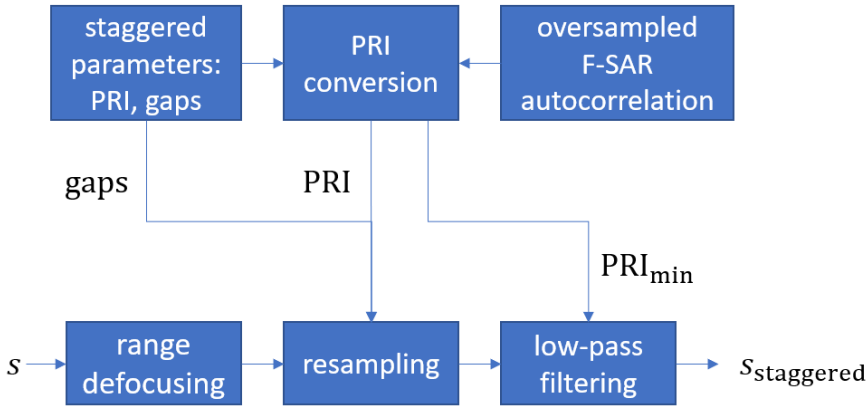

Figure 5.33 Process chain for staggered SAR signal generation.

subsequent azimuth samples similar to a real spaceborn SAR, like Tandem-L. The corresponding time vector for the resampling of the F-SAR data was again calculated by comparing the correlation of the Tandem-L system for a given PRF with an oversampled correlation of F-SAR. In opposition to the resampling in the previous section, the PRI for the staggered SAR were changing, which required the separate calculation of each PRI separately. Thus, the staggered PRI vector for the exemplary Tandem-L system was calculated for a mean PRF of 2700 Hz and subsequently transformed, sample by sample, into a corresponding PRI vector for the F-SAR system. The new values were calculated according to the steps in section 5.3.1 with the Tandem-L system parameters and a PRF according to the transformed PRI, as well as an oversampled F-SAR correlation at 100 kHz.
For the resampling of the F-SAR data at the Staggered PRI Subsequently the original signal could be simply resampled by a linear interpolation, which was possible, thanks to the high oversampling of the F-SAR data. Adjacent to the resampling, a low-pass filter was applied on the generated image at the smallest PRI to remove noise introduced by higher frequencies. In the final step of the signal

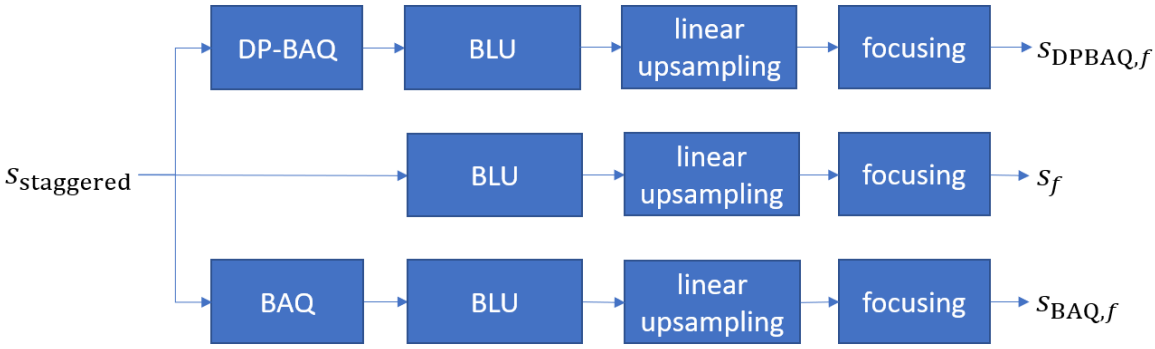

Figure 5.34 Process chain for quantization steps on staggered SAR with signal reconstruction.

generation, the gaps were introduced in the resampled signal. The translated PRI sequence, as well as the position of the gaps can be seen in Figure 5.35.

For the quantization, the DP-BAQ with gap mitigation implemented, as described in section 3.5.4,

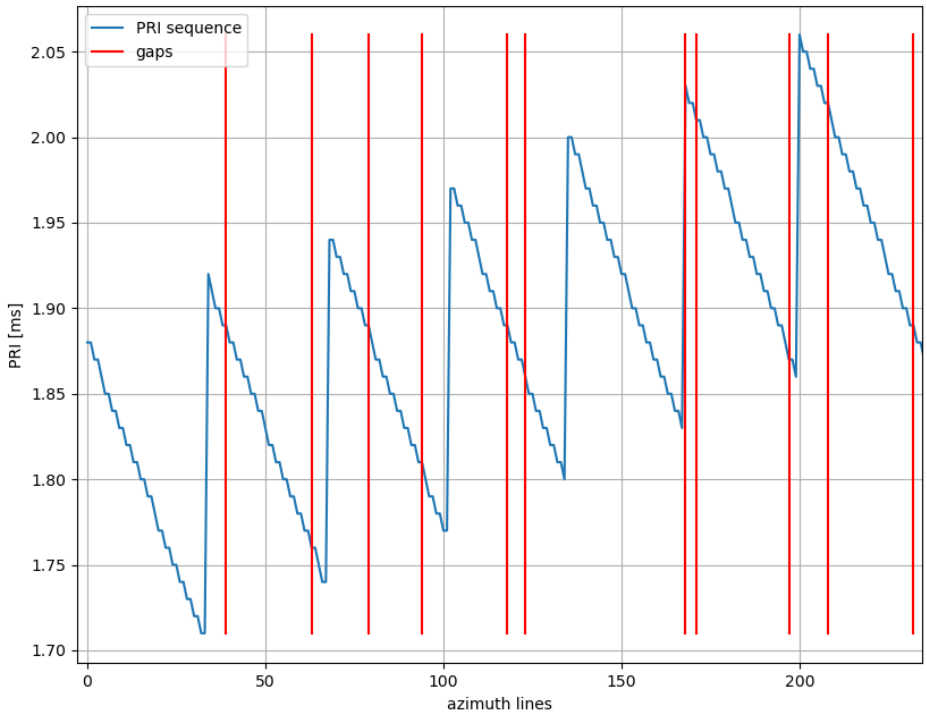

Figure 5.35 Translated F-SAR PRI sequence for a single staggered SAR sequence of the Tandem-L system at a mean PRF of 2700 Hz, with the gap position marked in red.

and applied on the staggered signal. The F-SAR autocorrelation, which was used for the calculation of the prediction weights, was calculated from the antenna pattern for each 128 bit range block and sampled at the mean staggered PRI of 1.88 ms, i.e. 532 Hz. Subsequently, the resulting quantized

signals for the first four prediction orders and different bit rates, as well as the un-quantized ”original´´ signal and the corresponding results of the BAQ for reference, were reconstructed with the BLU interpolation at the mean staggered PRI.
The resulting SQNR plots of the first four prediction orders as well as the BAQ quantized samples after the BLU reconstruction can be seen in Figure 5.36 and the absolute Gain for the predictors in Figure 5.37. The plots show, that the 3 bps DP-BAQ at the third and fourth order almost matches the performance of the 4 bps BAQ, which is equal to the reduction of a fourth of the originally used data. Furthermore, a 20% reduction of data reduction could be achieved by using a DP-BAQ at a bitrate of 4 bps instead of a BAQ at 5 bps. Furthermore, the calculation of the prediction weights at the exact staggered PRI showed no visible gain, as can be seen in Figure 5.38, thus the prediction weights were calculated for simplicity on the mean PRI.

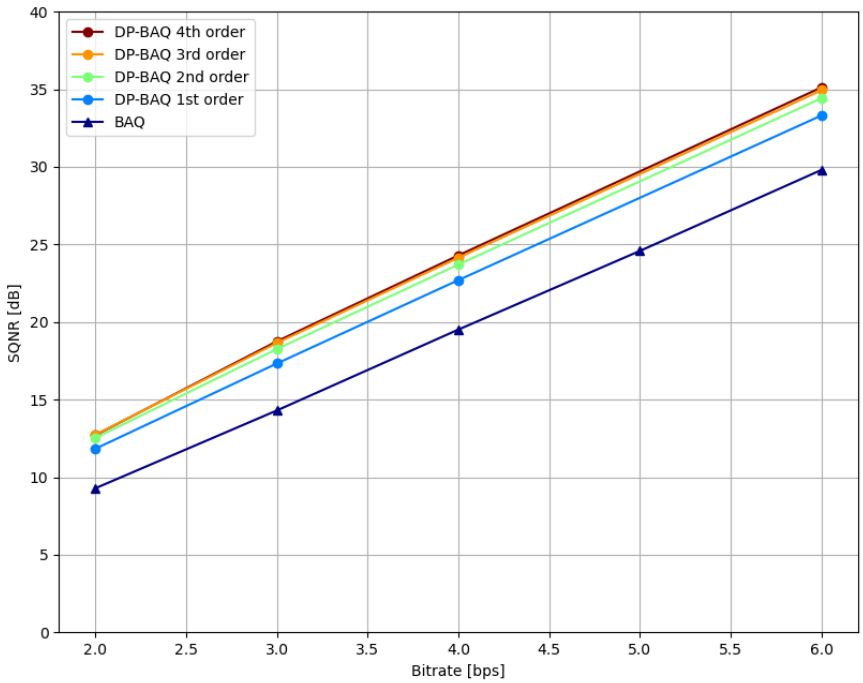

Figure 5.36 SQNR for the staggered SAR data set based on real F-SAR data after BLU reconstruction.

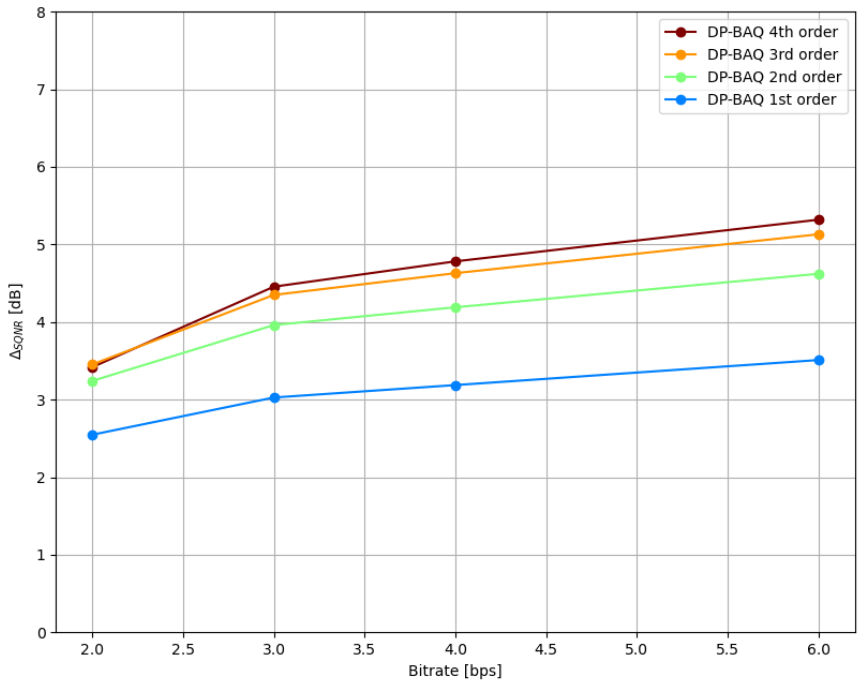

Figure 5.37 Absolute gain Δ_{SQNR} for the staggered SAR data set based on real F-SAR data after BLU reconstruction.

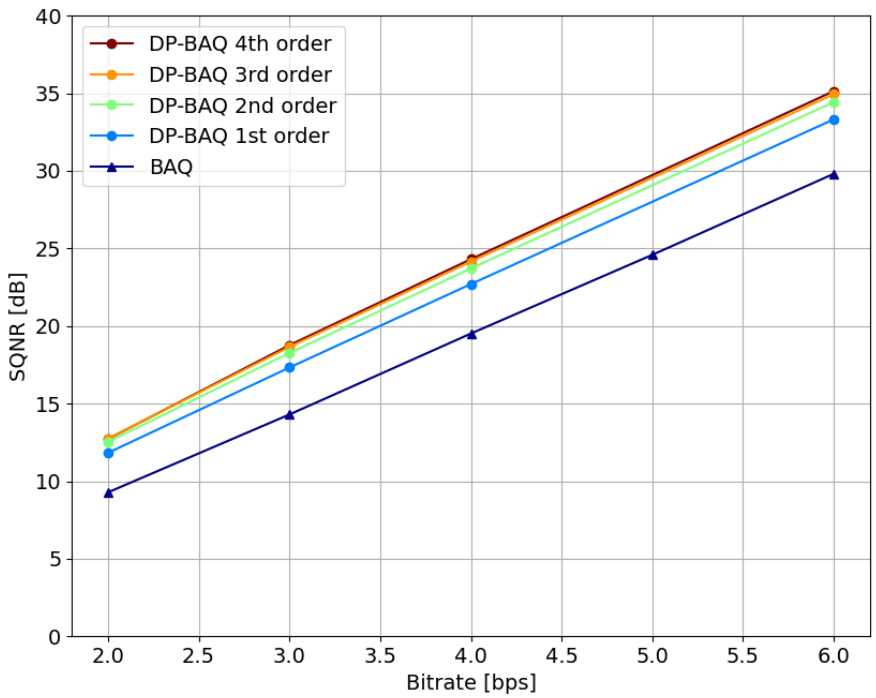

Figure 5.38 SQNR for the staggered SAR data set based on real F-SAR data after BLU reconstruction with prediction weights, calculated at the Staggered PRI.

In preparation for the SAR focusing, all resulting signal-sets were upsampled to the next higher fractional PRF of the original F-SAR system, which corresponds to one fourth of the original frequency, or equally said, 625 Hz.
The subsequent SAR focusing in range and azimuth resulted in an additional 3 dB gain to the SQNR plots, which can be seen in Figure 5.39, whereas the the changes in the corresponding absolute gain in Figure 5.40 are negligible. The exact SQNR distributions for all bit rates of the fourth order DP-

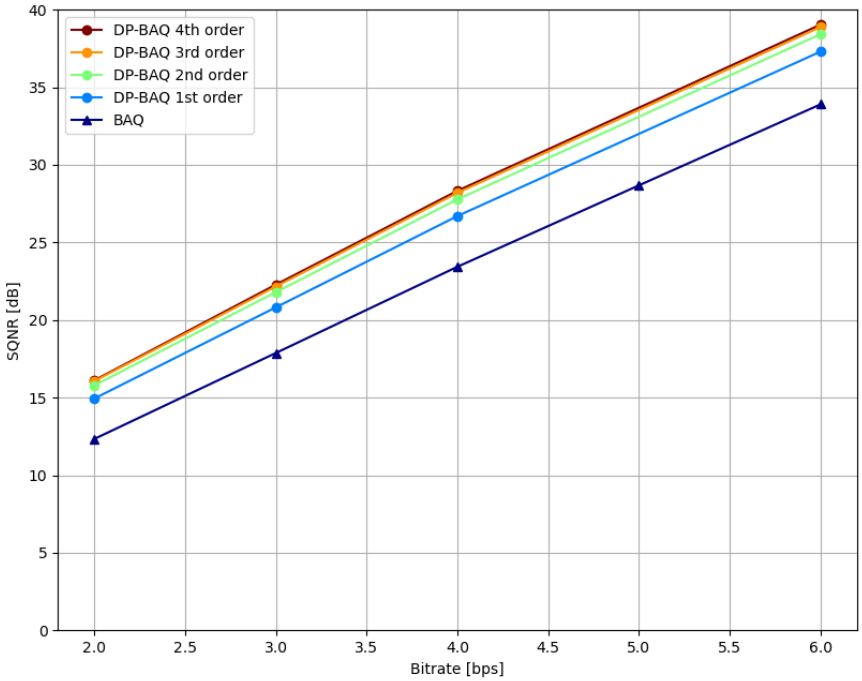

Figure 5.39 SQNR for the staggered SAR data set based on real F-SAR data after full SAR focusing.

BAQ can be seen in the histograms in Figure 5.41, 5.42, 5.43 and 5.44, and show the achieved gain for each bit rate, ranging like in the previous analysis around 6 dB, as well as the equal distribution of the SQNR values as indication for equal performance of the bitrates.

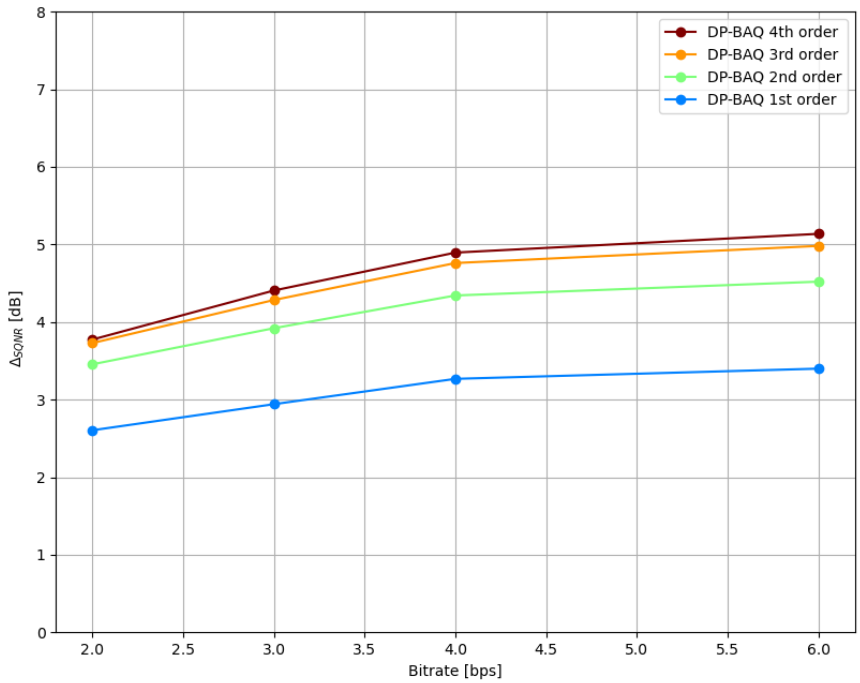

Figure 5.40 Gain for the staggered SAR data set based on real F-SAR data after full SAR focusing.

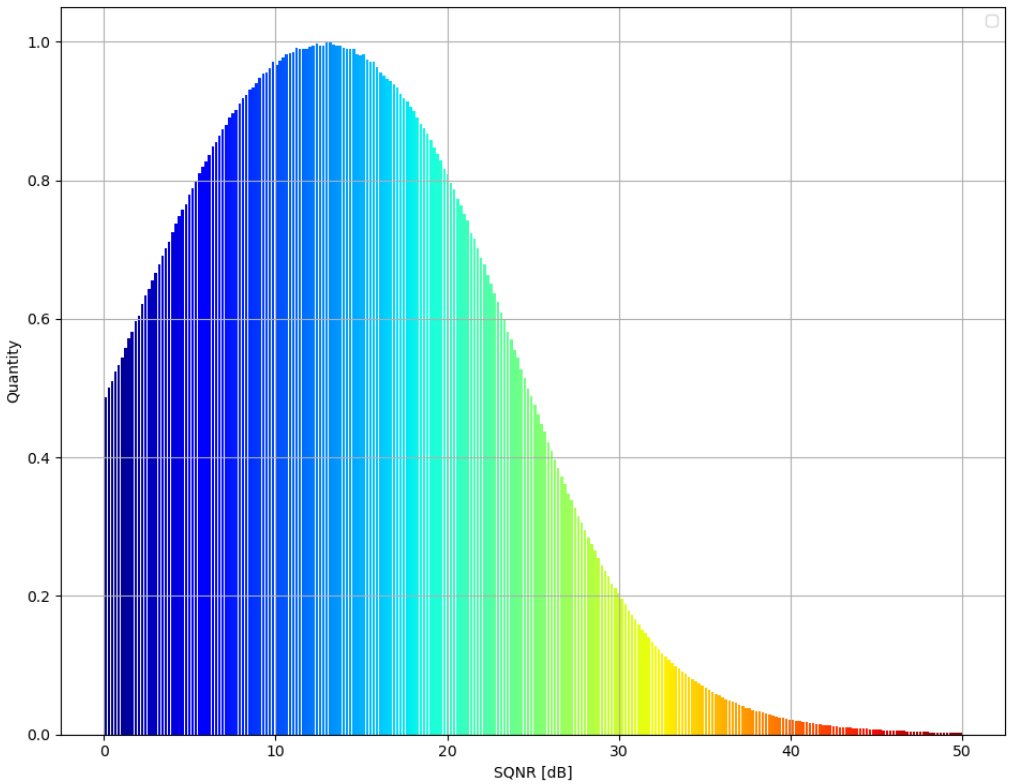

Figure 5.41 SQNR histogram of all pixels for the fourth order predictor at 2bps.

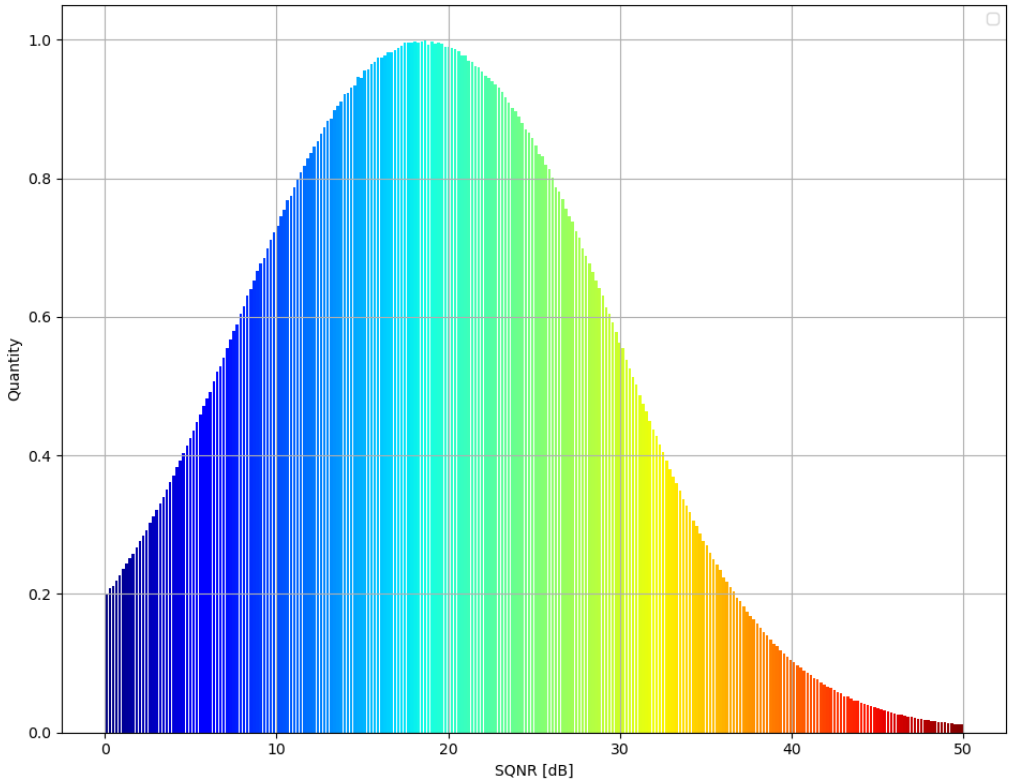

Figure 5.42 SQNR histogram of all pixels for the fourth order predictor at 3bps.

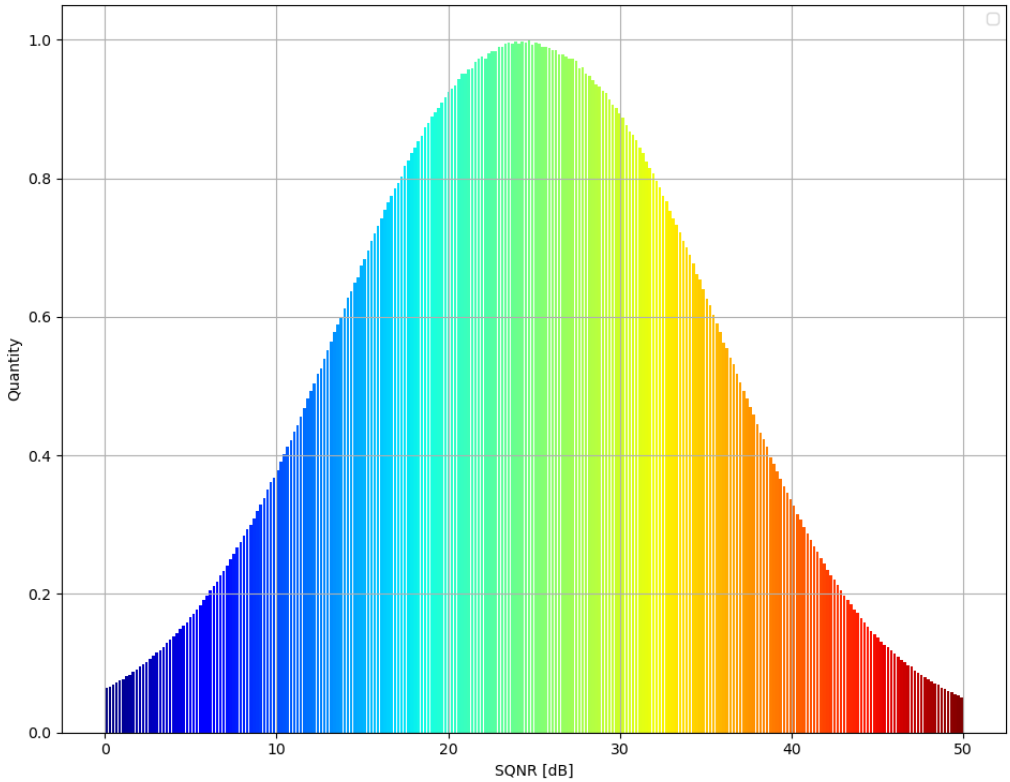

Figure 5.43 SQNR histogram of all pixels for the fourth order predictor at 4bps.

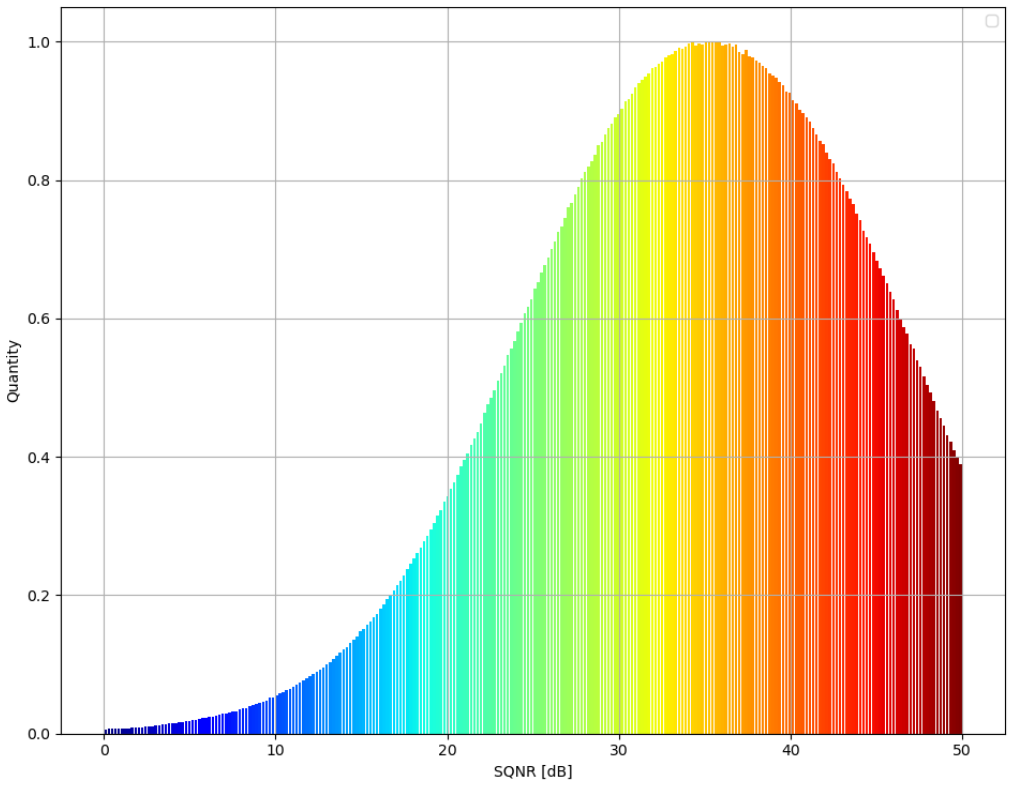

Figure 5.44 SQNR histogram of all pixels for the fourth order predictor at 6bps.

As already stated in the analysis after the BLU, the results of the BAQ at 4 bps and 5 bps were showing similar results as the fourth order DP-BAQ at 3 bps and 4 bps respectively. Thus, these BAQ cases represent possible candidates of being replaced by the DP-BAQ for data reduction and will be further investigated in the following plots.
Figure 5.45 shows the SQNR values of the fourth order predictor at a bitrate of 3 bps. The values for the SQNR are calculated and displayed on each pixel as well the histogram of all SQNR values. When comparing to the corresponding plot for the four bit BAQ in Figure 5.46, the histograms of both plots are almost identical with the BAQ shifted by ~ 1.2 dB to the higher SQNR values, which equals a data reduction of 25% at the cost of a 5% worse image quality. The same shift applies for the two dimensional representation of the SQNR, where the DP-BAQ mainly lacks performance in low backscattering areas like grass land and fields, while the areas with higher intensities and SQNR values are represented in a comparable quality. The corresponding plots for the 4 bit fourth order DP-BAQ (Figure 5.47) and the 5 bit BAQ (Figure 5.48) show similar outcomes, with a smaller difference in the performance of only ~ 0.4 dB, i.e. a data reduction of 20% at the cost of only 1.6% worse image quality.

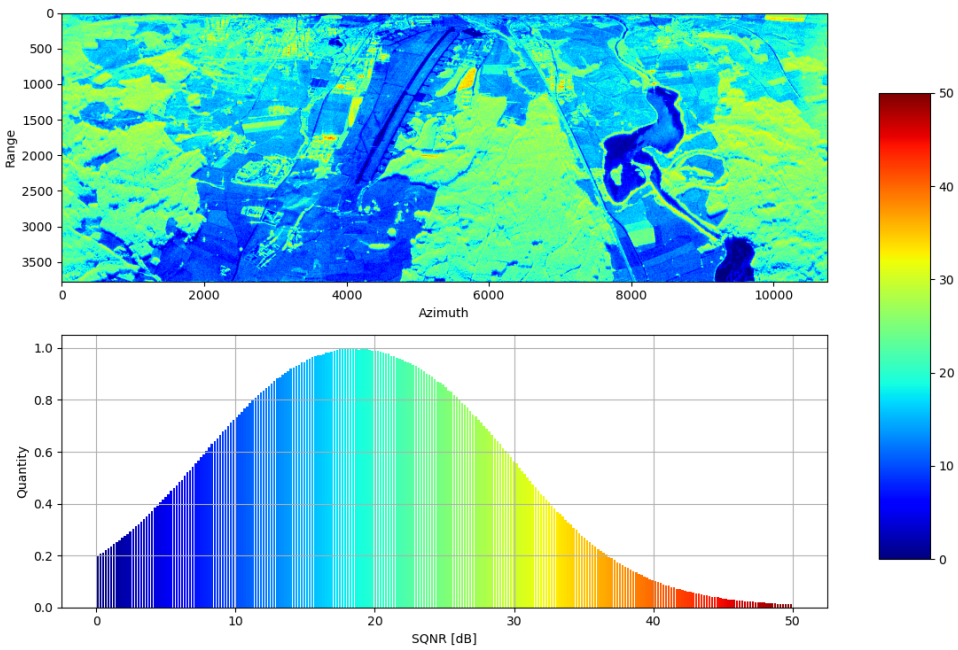

Figure 5.45 SQNR calculated on each pixel of the fully focused SAR image with corresponding histogram of all pixels for the fourth order predictor at 3bps.

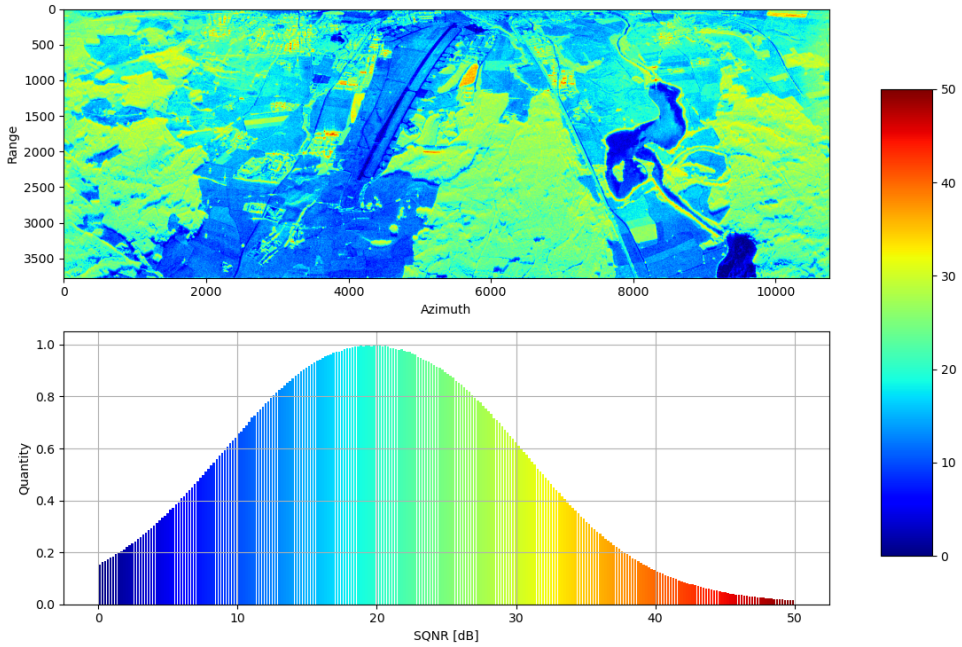

Figure 5.46 SQNR calculated on each pixel of the fully focused SAR image with corresponding histogram of all pixels for the 4bps BAQ.

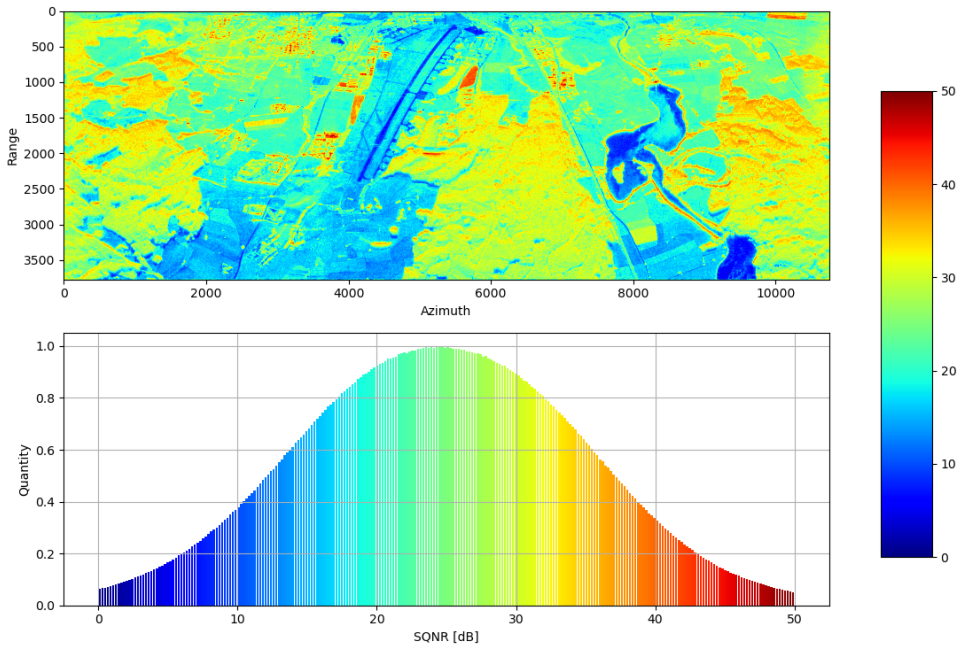

Figure 5.47 SQNR calculated on each pixel of the fully focused SAR image with corresponding histogram of all pixels for the fourth order predictor at 4bps.

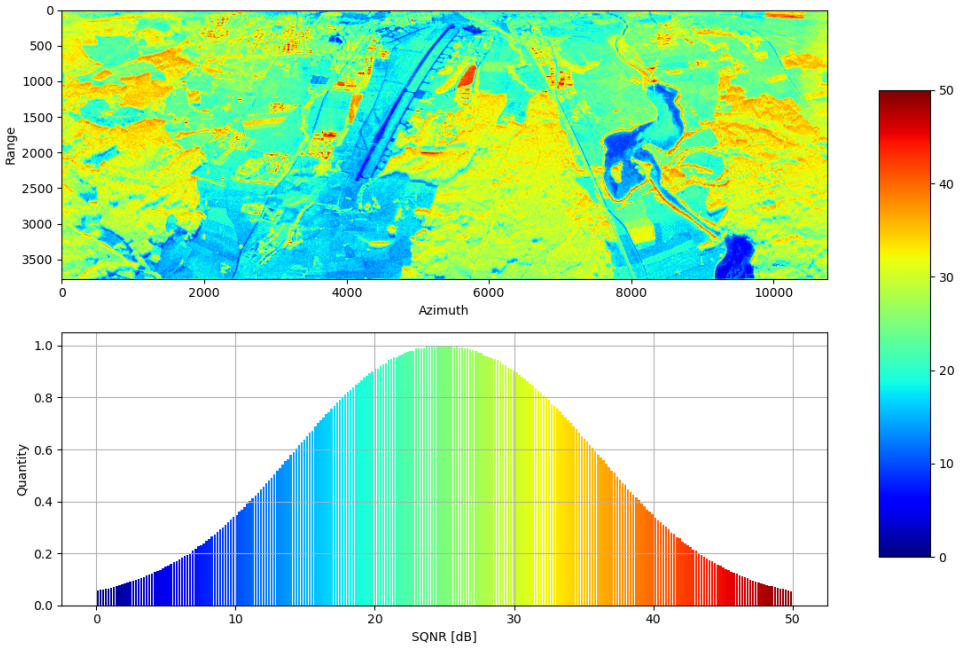

Figure 5.48 SQNR calculated on each pixel of the fully focused SAR image with corresponding histogram of all pixels for the 5bps BAQ.

The phase error, which was introduced by the quantization, can be seen in representative form for each pixel in the histograms of Figures 5.49, 5.50, 5.51 and 5.52 . The phase error was calculated according to

$$\Delta_{\Phi_n} = \Phi_n - \Phi_{n,q} \quad \text{with} \quad \Delta_{\Phi_n} \in [-\pi, +\pi], \tag{5.5}$$

where Φ_n corresponds to the phase of the nth pixel for the non-quantized signal and $\Phi_{n,q}$ the corresponding phase of the quantized signal. All values exceeding the maximum value for the phase error of $+/-\pi$ are wrapped around the interval borders. The effect of adding an additional bit to the quantization process can be seen, when comparing the histogram of the phase error to the 2 bps case (Figure 5.53) of the same order. By comparing the results for the phase errors of the two similar performing cases visually, the difference is negligible for both cases.

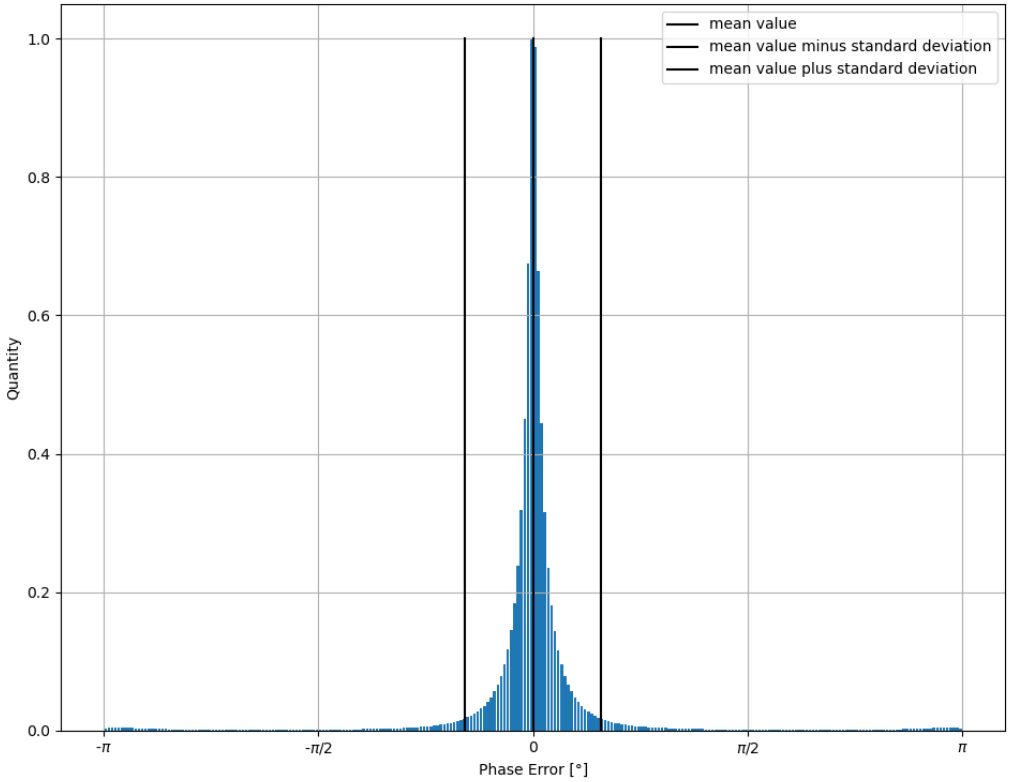

Figure 5.49 Phase error calculated on each pixel of the fully focused SAR image with corresponding histogram of all pixels for the fourth order predictor at 3bps.

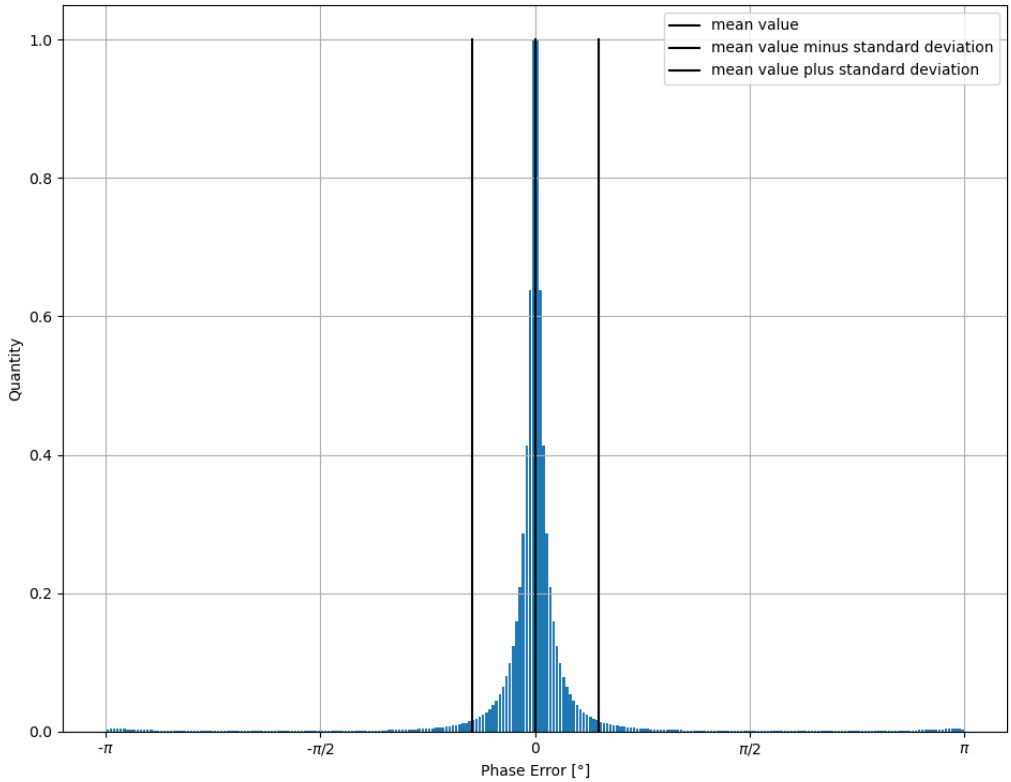

Figure 5.50 Phase error calculated on each pixel of the fully focused SAR image with corresponding histogram of all pixels for the 4bps BAQ.

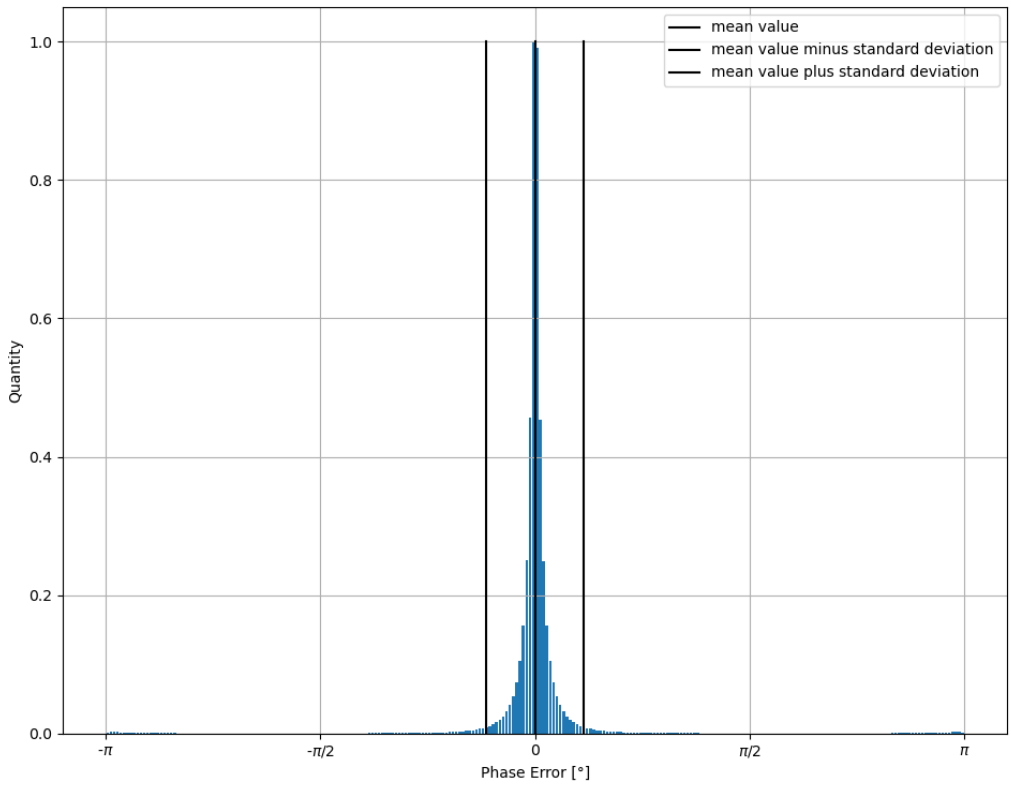

Figure 5.51 Phase error calculated on each pixel of the fully focused SAR image with corresponding histogram of all pixels for the fourth order predictor at 4bps.

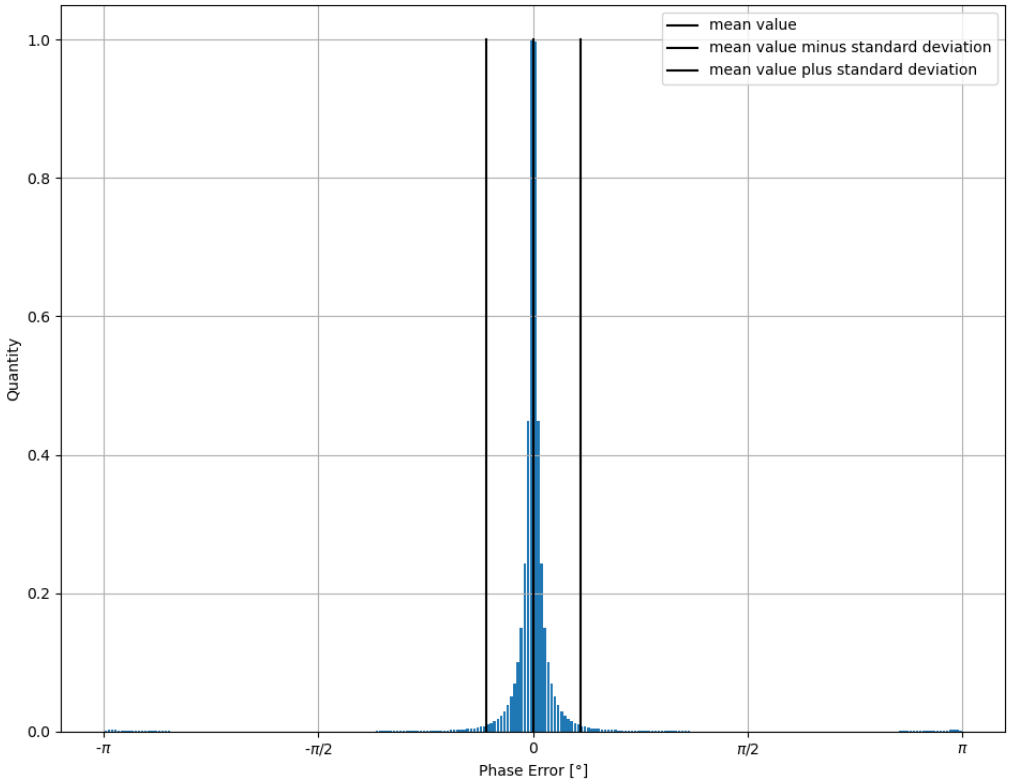

Figure 5.52 Phase error calculated on each pixel of the fully focused SAR image with corresponding histogram of all pixels for the 5bps BAQ.

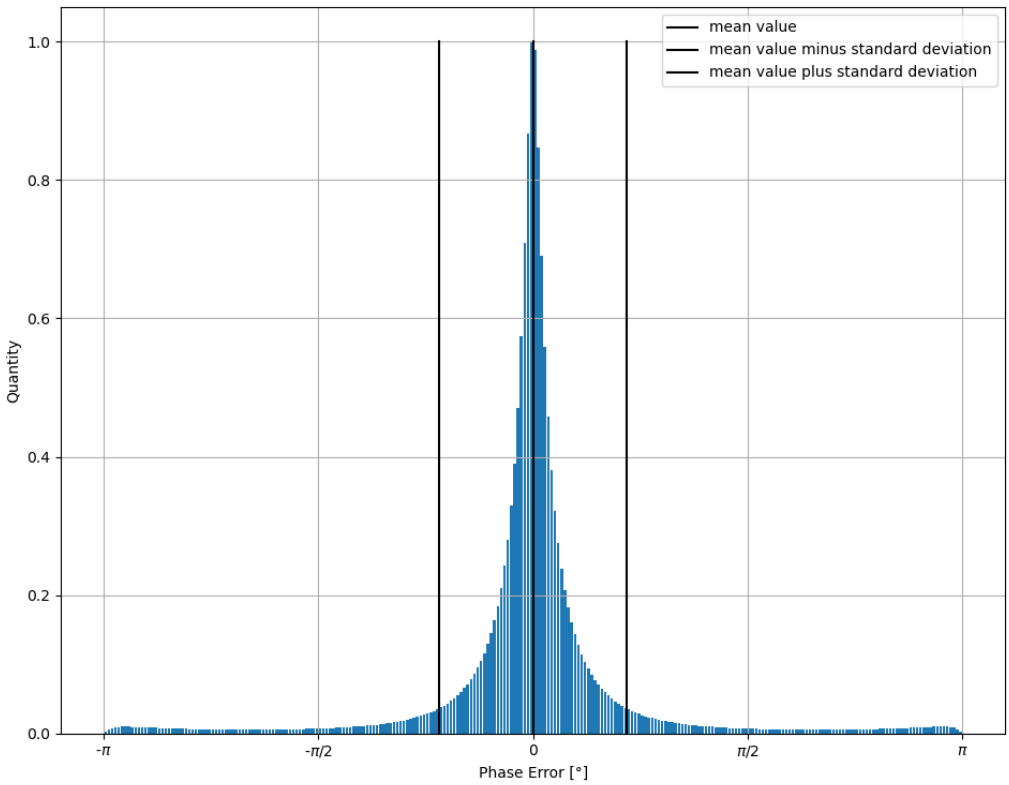

Figure 5.53 Phase error calculated on each pixel of the fully focused SAR image with corresponding histogram of all pixels for the fourth order predictor at 2bps.

The intensity plots of both combinations can be seen in Figure 5.54, 5.55, 5.56 and 5.57. The comparison between the plots of the BAQ and the corresponding plots of the DP-BAQ show no visible differences thanks to the similar performance. The biggest change can be seen between different bitrates, where low backscattering areas like lakes and runways are visibly better represented for higher bitrates.
The effects of the quantization on low backscatter regions are also visible in the last plots of this analysis, which show the Noise Equivalent Sigma Zero (NESZ) estimated on the two lakes in the SAR image (Figure 5.58) , according to

$$NESZ_{\text{range}} = \frac{1}{N} \cdot \sum_{i=k}^{k+N} \sigma_0[i], \tag{5.6}$$

with $NESZ_{\text{range}}$ corresponding to the NESZ value of a single range line, k to the azimuth coordinate, where the lake starts, N corresponding to the number of samples in azimuth direction and $\sigma_0[i]$ to the pixel specific value for σ_0. The NESZ for the DP-BAQ and BAQ quantized signals can be seen in Figure 5.59 and 5.60. As for the Intensity plots, the comparison between the corresponding results of the different quantizer shows similar noise levels for both lake sites. When comparing the bitrates on the other hand, it becomes clear that most of the introduced noise is resulting from reduced bitrates in the quantization.
Concluding to all results, this section showed, that the implementation of the DP-BAQ on real Staggered SAR data is possible. Furthermore, the Results show consistent performance and a maximum gain compared to the BAQ of ~ 5 dB. In addition the DP-BAQ allows for a data reduction of $20-25\%$ with minimal to none losses in the image quality, which are mostly present in low backscattering areas.

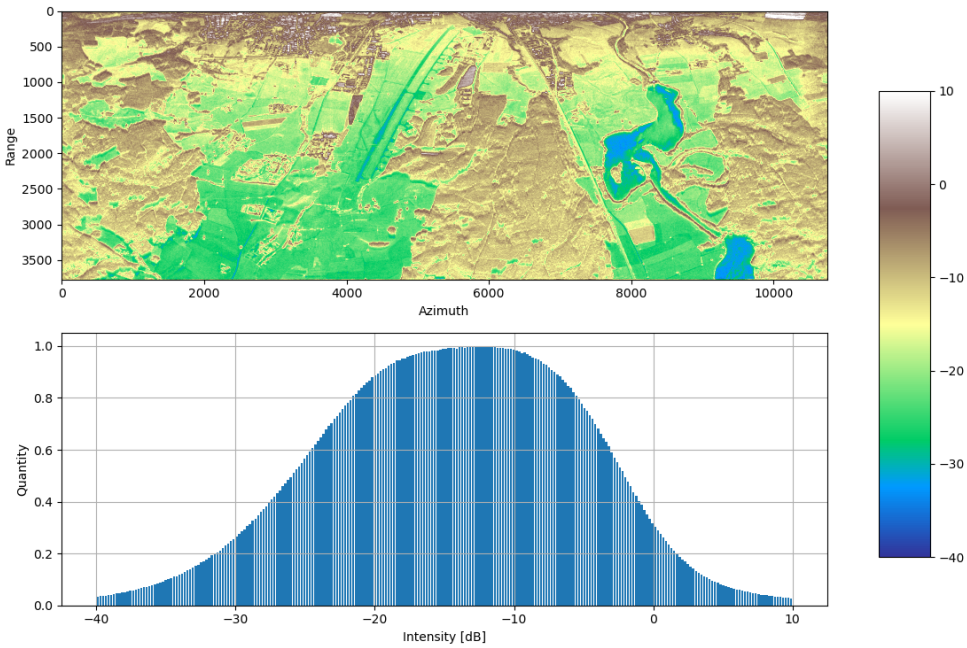

Figure 5.54 Intensity calculated on each pixel of the fully focused SAR image with corresponding histogram of all pixels for the fourth order predictor at 3bps.

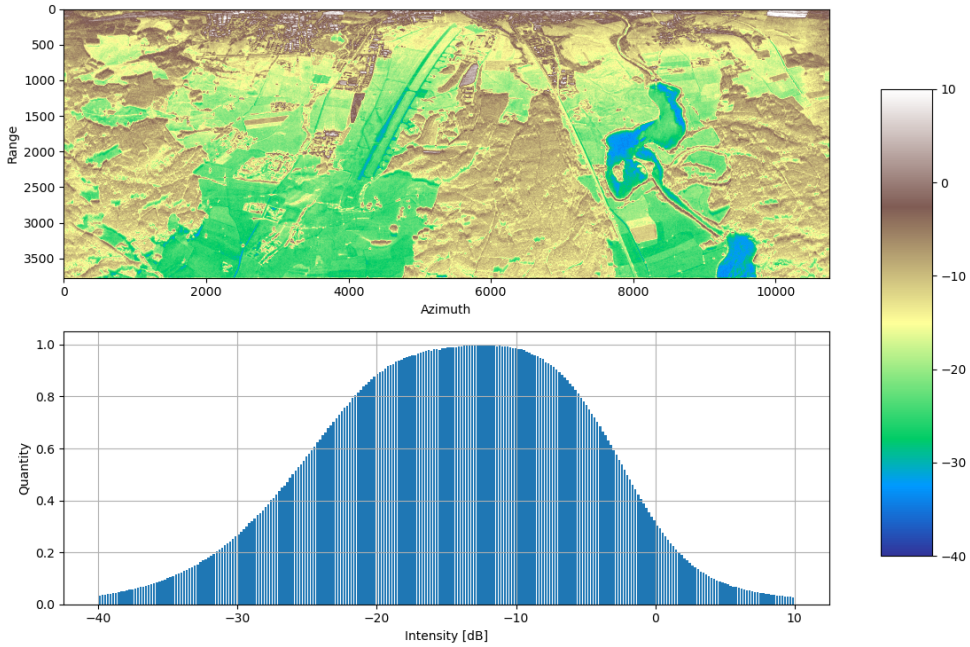

Figure 5.55 Intensity calculated on each pixel of the fully focused SAR image with corresponding histogram of all pixels for the 4bps BAQ.

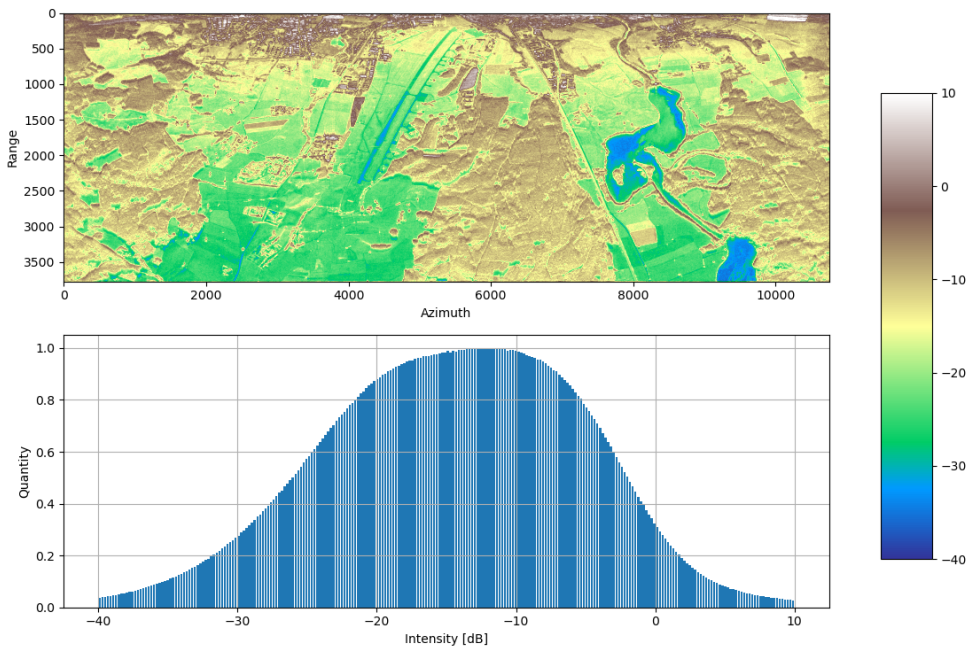

Figure 5.56 Intensity calculated on each pixel of the fully focused SAR image with corresponding histogram of all pixels for the fourth order predictor at 4bps.

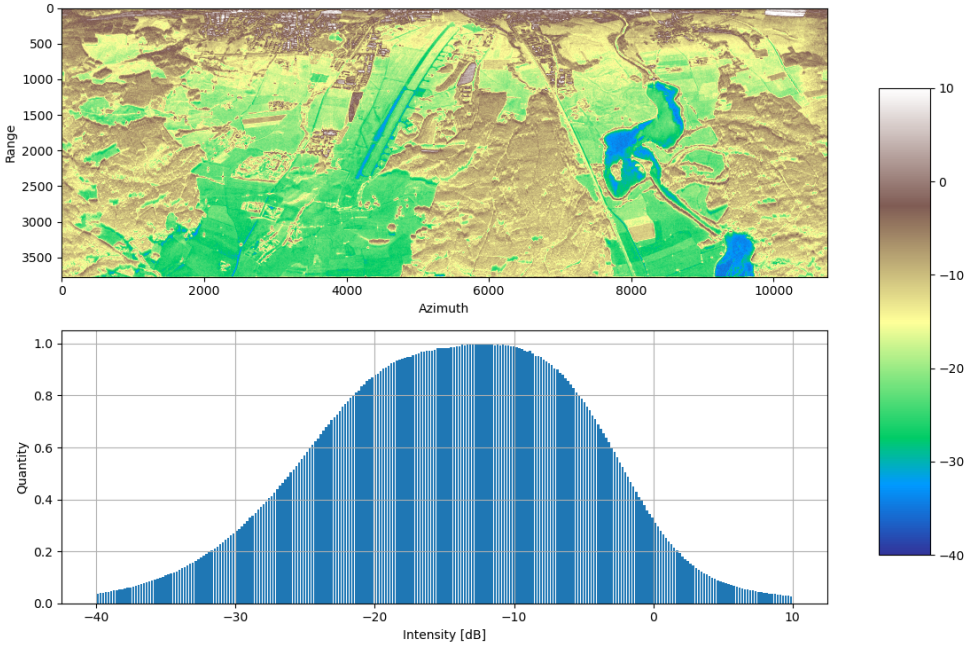

Figure 5.57 Intensity calculated on each pixel of the fully focused SAR image with corresponding histogram of all pixels for the 5bps BAQ.

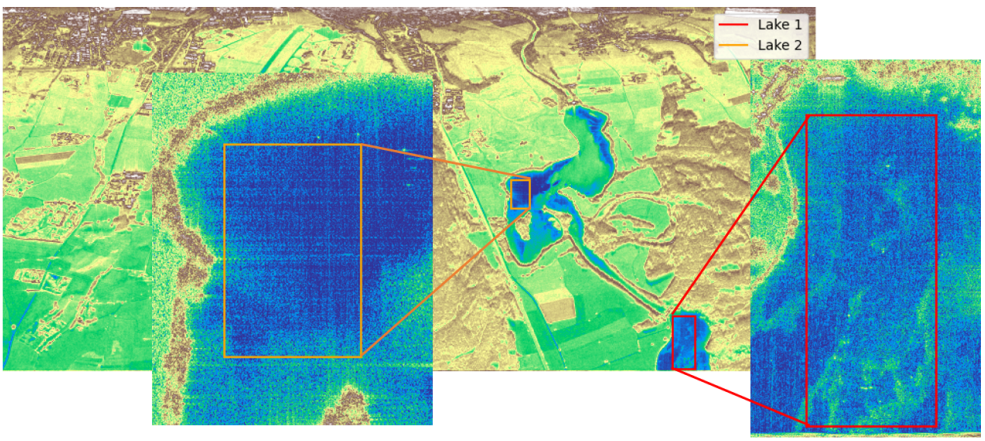

Figure 5.58 Positions of the two lakes used for the calculation of the Noise equivalent sigma zero.

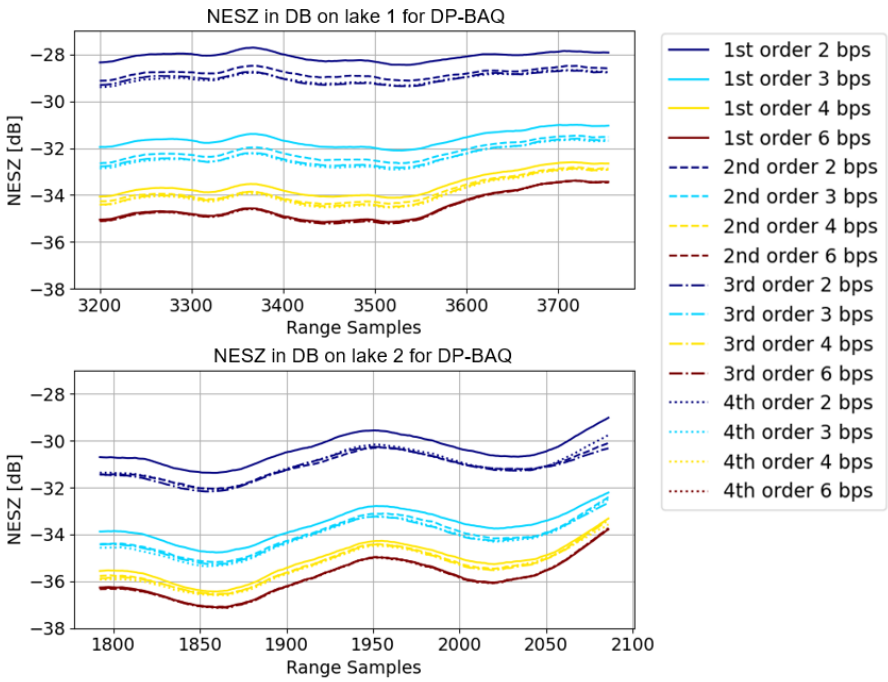

Figure 5.59 Noise equivalent sigma zero calculated on all orders and bit rates of the DP-BAQ for the staggered SAR data set.

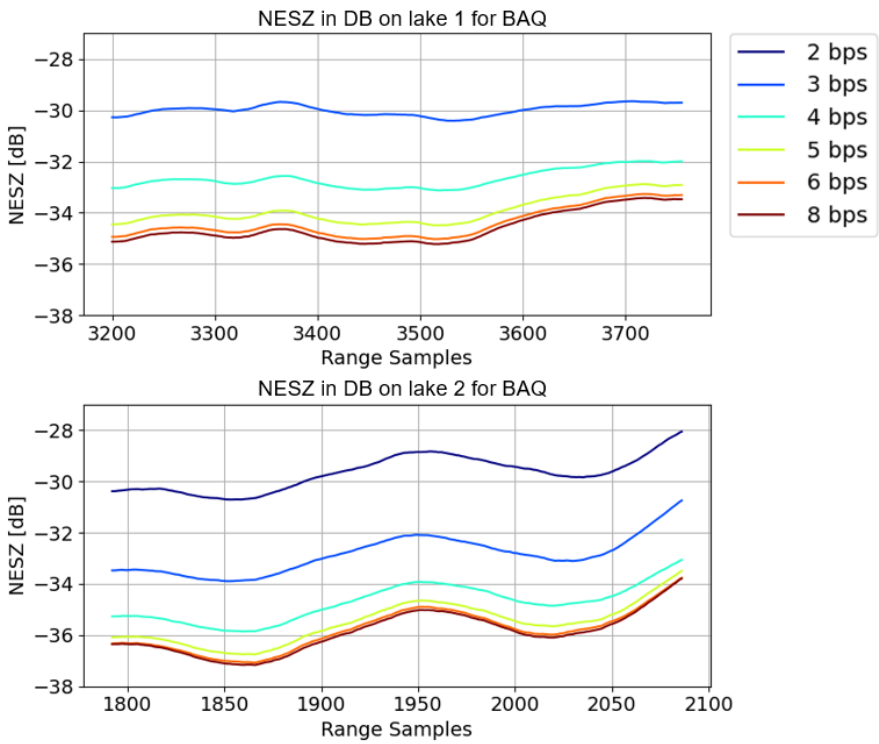

Figure 5.60 Noise equivalent sigma zero calculated on all bit rates of the BAQ for the staggered SAR data set.

6 Conclusion and outlook

The constant development of SAR acquisition methods and the design of new SAR systems, which are capable of wider swath widths and higher spatial resolutions, result in the generation of huge amount of data onboard the SAR systems. As an example, the Tandem-L SAR system, which was proposed by DLR, generates approximately 8 Terrabyte of data per day. Under consideration of the restricted computational power and onboard data storage capacity of a spaceborne SAR system, this requires the development of new methods for effective onboard data reduction. The method, called *Dynamic Predictive BAQ* (DP-BAQ), which was analyzed in this thesis work provides a good data reduction at a low computational cost while maintaining a high image quality compared to alternate approaches. The new method exploits the correlation between subsequent samples along the azimuth direction by using Linear Predictive Coding (LPC) to generate a signal with lower signal dynamic, which means less bits for a proper representation after a quantization. The new signal for quantization is hereby calculated as the difference between the original sample and its prediction and a BAQ was used for the quantization.
The goal of this thesis was to verify prior simulations of this quantizer based on synthetic data and to prove the full functionality for the first time on real Staggered SAR data under spaceborne conditions. Since no SAR system is capable of producing Staggered SAR data yet, real airborne SAR data was used to generate the data sets according to the system parameters of Tandem-L, which is capable of Staggered SAR acquisitions thanks to its azimuth oversampling. The SAR images were provided by the F-SAR system of DLR in range compressed form and targeted the well known test site in Kaufbeuren, south Germany. The airborne system, which is specially designed for testing new acquisition methods, provides a much higher oversampling of SAR data in azimuth direction than Tandem-L. Thus, represents ideal properties to generate the required data sets. In preparation for the final analysis the predictive quantizer was tested under different conditions to ensure the full functionality on synthetic data, as well as real SAR data in general and under Staggered SAR-like conditions with a constant sampling rate.
The performance was evaluated considering the achievable image quality in form of the Signal to Quantization Noise Ratio (SQNR) for a given bit rate. The results were analysed for the DP-BAQ of the first four prediction orders, using the a priori knowledge on the signal statistics from the antenna pattern, and compared to a direct quantizer in form of a BAQ for reference.
The analysis on the synthetic data verified the results of preceding tests and the functionality of the algorithms in general. The tests included Monte Carlo simulations of the DP-BAQ on synthetic data, which were generated based on the Tandem-L system parameters. The analysis showed the expected average gain of 6 dB per additional bit in the quantization. Furthermore, an additional gain of approximate 4 dB could be observed for a third order predictor at a Pulse Repetition Frequncy (PRF) of 2.7 kHz, which matches with prior results on synthetic data.
The remaining tests analyzed the functionality of predictive coding with real SAR data and were all based on the F-SAR acquisition. The general functionality of the DP-BAQ on real data was investigated by the direct application of the DP-BAQ on the airborne data. Thanks to the high oversampling, the results showed a gain of the DP-BAQ with respect to a normal BAQ of up to $22\mathrm{dB}$, as well as possible data reduction of up to 70% for a second order predictor. Nevertheless, the results also showed limitations of the quantizer for strongly correlated signals at higher prediction orders, which were caused by the dynamic reduction of the LPC that could not be handled by the quantizer. Despite these irregularities, which represent a special case with correlation values far higher than for a spaceborne system, the direct implementation proved that the predictive quantizer is applicable on real SAR data.

In order to analyse the predictive coder in a scenario, which represents a more realistic field of application, the F-SAR data was adapted to the parameters of the Tandem-L system. The analysis showed consistent results for all prediction orders and similar performance to the results from the synthetic simulations on the DP-BAQ, with small improvements in the gain. The quantizer was able to achieve an absolute gain compared to the BAQ of approximate 6 dB for a third order DP-BAQ. Those results proved that the DP-BAQ is applicable for its intentional purpose of reducing data for a spaceborne satellite system with azimuth oversampling.
The main analysis of this thesis was conducted on Staggered SAR data, which included non-uniform PRI sequences and the presence of gaps for a Tandem-L-like scenario. In order to achieve maximum performance, the DP-BAQ was implemented with full gap mitigation, i.e. dynamic bit allocation and variable prediction orders. Subsequent to the quantization the signal was reconstructed to a constant time vector and SAR focused. The results showed equal performances of a 3 bit DP-BAQ and a 4 bit BAQ, corresponding to a data reduction rate of 25%, which is matching with the results in the synthetic simulations. Additionally, the predictor was able to achieve data reduction rates of over 20% for the 4 bit DP-BAQ. Further analysis on the completely focused SAR image showed, that the quantizer is capable of representing high amplitude variations and did not introduce visible corruptions, or a significant rise in the noise-floor.
As a conclusion, the analysis proved the outcomes of preceding analysis on synthetic staggered data. Furthermore the new predictive quantizer was succesfully implemented for real SAR data and showed, in combination with the precalculated signal statistics, good performance on the oversampled F-SAR data. In addition, the analysis demonstrated that the predictive quantizer performs stable for lower prediction orders, even far off reasonable correlation values. On the other hand, the analysis was able to reveal possible limitations for the DP-BAQ, which can be investigated in further analysis. As the most important outcome of this thesis, the DP-BAQ could be succesfully implemented and tested on real spaceborne SAR data, which showed good performance and stability for a uniformly sampled SAR image, but more importantly also the expected performance on staggered SAR data in the presence of gaps. The implemented DP-BAQ was able to achieve data reduction rates of over 20%, which is validating the results of the synthetic simulation. Additionally, the predictor did not corrupt the image, or introduced further noise.
Considering further development of predictive coding in combination with SAR quantization, there are still many open points that need to be investigated. Since this thesis showed the behaviour of predictive coding in combination with highly oversampled data, as well as the resulting limitations for quantization, it would be of great interest to investigate the performance on very low oversampled data, like for TanDEM-X. Another field of interest is represented by the design of the predictor. The samples that have been used for prediction so far were all previously recorded samples, providing a processing of the recorded data in real time, since all data samples required for the prediction are available at the time of recording. This prediction structure is called a causal predictor. Further investigations could as example include the effects of a non-causal predictor on the system performance, which is not capable of real time prediction, since its usage of samples before and after the predicted sample requires the predictor to wait for upcoming samples. This new approach would introduce increased complexity of the system during the decoding of the signal, due to inconsistencies in the available data during the encoding and decoding, but since the decoding is performed on ground, the increased computational effort is tolerable.

A Appendix

A.1 First Order Predictor

The first order predictor uses only one, i.e. the preceding, sample for the prediction process. As already mentioned in the previous section, both variables depend on the same process and have therefore the same base variance σ_x. During the prediction process the sample is weighted by β_1, which also applies to $\sigma_y = \beta_1 \sigma_x$ and therefore leads to the total variance of the differential signal in (3.53) of

$$\sigma_{d1}^2 = \sigma_x^2 + \sigma_y^2 - 2\sigma_x\sigma_y\rho_{xy} = \sigma_x^2 + \beta_1^2\sigma_x^2 - 2\sigma_x^2\beta_1\rho_{xy}. \tag{A.1}$$

The value for β_1 can be derived from (3.42) as

$$\boldsymbol{\beta} = \beta_1 = \boldsymbol{C}^{-1}\boldsymbol{\rho} = [1]^{-1}\rho_{xy} = \rho_{xy}, \tag{A.2}$$

, with ρ_{xy} referring to the correlation at a time lag of $|t_x - t_y|$. By substituting (A.2) into (A.1) this leads to the exact calculation of σ_{d1}^2

$$\sigma_{d1}^2 = \sigma_x^2 + \rho_{xy}^2\sigma_x^2 - 2\sigma_x^2\rho_{xy}^2 = \sigma_x^2(1 - \rho_{xy}^2). \tag{A.3}$$

The coding gain can then be calculated by substituting (A.3) into (3.49) and deriving the first order coding gain G_1

$$G_1 = \frac{\sigma_x^2}{\sigma_x^2(1 - \rho_{xy}^2)} = \frac{1}{(1 - \rho_{xy}^2)}. \tag{A.4}$$

By analyzing (A.3) and (A.4) it is visible that the variance and therefore the Coding gain is reduced for any value of $\rho > 1$.

A.2 Second order Predictor

For the second order predictor the variances can be calculated the same way. This time the prediction is dependent on the last two prior samples, extending the closed form expression of the variance for the difference for one additional parameter to

$$\mathcal{D} \triangleq \mathcal{X} - \mathcal{Y} - \mathcal{Z} \sim \mathcal{N}(0, \sigma_x^2 + \sigma_y^2 + \sigma_z^2 - 2\sigma_{xy} - 2\sigma_{xz} + 2\sigma_{yz}). \tag{A.5}$$

Under the assumption that all normal distributed variables are based on the same random process, they can be defined as

$$\mathcal{X} \sim \mathcal{N}(0, \sigma_x^2) \quad \mathcal{Y} \sim \mathcal{N}(0, \sigma_y^2) = \mathcal{N}(0, \beta_1^2\sigma_x^2) \quad \mathcal{Z} \sim \mathcal{N}(0, \sigma_z^2) = \mathcal{N}(0, \beta_2^2\sigma_x^2). \tag{A.6}$$

The covariances can be derived as in the preceding chapters by multiplication of the variances of the concerning two random processes and the corresponding correlation, resulting in

$$\sigma_{xy} = \sigma_x\sigma_y\rho_{xy} \quad \sigma_{xz} = \sigma_x\sigma_z\rho_{xz} \quad \sigma_{yz} = \sigma_y\sigma_z\rho_{yz}. \tag{A.7}$$

The corresponding prediction weights can be calculated according to 3.42

$$\begin{bmatrix} \beta[1] \\ \beta[2] \end{bmatrix} = \begin{bmatrix} 1 & \rho_{yz} \\ \rho_{yz} & 1 \end{bmatrix}^{-1} \begin{bmatrix} \rho_{xy} \\ \rho_{xz} \end{bmatrix}. \tag{A.8}$$

By using the definitions in (A.6) and (A.7) and substituting them into (A.5) the variance of the prediction error can be reformulated to

$$\sigma_{d2}^2 = \sigma_x^2(1 + \beta_1^2 + \beta_2^2 - 2\beta_1\rho_{xy} - 2\beta_2\rho_{xz} + 2\beta_1\beta_2\rho_{yz}). \tag{A.9}$$

Finally leading to the definition of the second-order coding gain as

$$G_2 = \frac{1}{\sigma_x^2(1 + \beta_1^2 + \beta_2^2 - 2\beta_1\rho_{xy} - 2\beta_2\rho_{xz} + 2\beta_1\beta_2\rho_{yz})}. \tag{A.10}$$

The above equation can be further simplified under the assumption, that the time lags between the samples are of equal length ($\rho_{xy} = \rho_{yz} = \rho_1$ and $\rho_{xz} = \rho_2$), to

$$G_2 = \frac{1}{\sigma_x^2(1 + \beta_1^2 + \beta_2^2 + 2\rho_1(\beta_1\beta_2 - \beta_1) - \rho_2\beta_2}. \tag{A.11}$$

A.3 Third order Predictor

The closed form representation for the variance of the 3rd order prediction difference is now defined as

$$\mathcal{D} \triangleq \mathcal{X} - \mathcal{Y} - \mathcal{Z} - \mathcal{W} \sim \mathcal{N}(0, \sigma_x^2 + \sigma_y^2 + \sigma_z^2 + \sigma_w^2 - 2\sigma_{xy} - 2\sigma_{xz} - 2\sigma_{xw} + 2\sigma_{yz} + 2\sigma_{yw} + 2\sigma_{zw}), \tag{A.12}$$

with the random variables according to

$$\begin{array}{cc} \mathcal{X} \sim \mathcal{N}(0, \sigma_x^2) & \mathcal{Y} \sim \mathcal{N}(0, \sigma_y^2) = \mathcal{N}(0, \beta_1^2\sigma_x^2) \\ \mathcal{Z} \sim \mathcal{N}(0, \sigma_z^2) = \mathcal{N}(0, \beta_2^2\sigma_x^2) & \mathcal{W} \sim \mathcal{N}(0, \sigma_w^2) = \mathcal{N}(0, \beta_3^2\sigma_x^2). \end{array} \tag{A.13}$$

The according weights can be calculated from (3.42) by considering now three preceding samples

$$\begin{bmatrix} \beta[1] \\ \beta[2] \\ \beta[3] \end{bmatrix} = \begin{bmatrix} 1 & \rho_{yz} & \rho_{yw} \\ \rho_{yz} & 1 & \rho_{zw} \\ \rho_{yw} & \rho_{zw} & 1 \end{bmatrix}^{-1} \begin{bmatrix} \rho_{xy} \\ \rho_{xz} \\ \rho_{xw} \end{bmatrix}. \tag{A.14}$$

Subsequently, the covariances can be calculated from

$$\begin{array}{ccc} \sigma_{xy} = \sigma_x\sigma_y\rho_{xy} & \sigma_{xz} = \sigma_x\sigma_z\rho_{xz} & \sigma_{xw} = \sigma_x\sigma_w\rho_{xw} \\ \sigma_{yz} = \sigma_y\sigma_z\rho_{yz} & \sigma_{yw} = \sigma_y\sigma_w\rho_{yw} & \sigma_{zw} = \sigma_z\sigma_w\rho_{zw}, \end{array} \tag{A.15}$$

leading to a variance σ_{d3}^2 for the prediction error of

$$\sigma_{d3}^2 = \sigma_x^2(1 + \beta_1^2 + \beta_2^2 + \beta_3^2 + 2\beta_1(\beta_2\rho_{yz} + \beta_3\rho_{yw} - \rho_{xy}) + 2\beta_2(\beta_3\rho_{zw} - \rho_{xz}) - 2\beta_3\rho xw), \tag{A.16}$$

which simplifies under the assumption ($\rho_{xy} = \rho_{yz} = \rho_{zw} = \rho_1$ and $\rho_{xz} = \rho_{yw} = \rho_2$ and $\rho_{xw} = \rho_3$) to

$$\begin{array}{c} \sigma_{d3}^2 = \sigma_x^2(1 + \beta_1^2 + \beta_2^2 + \beta_3^2 + 2\rho_1(\beta_1\beta_2 + \beta_2\beta_3 - \beta_1) + \\ 2\rho_2(\beta_1\beta_3 - \beta_2) - 2\rho_3\beta_3). \end{array} \tag{A.17}$$

The gain can then be calculated from

$$G_3 = [(1 + \beta_1^2 + \beta_2^2 + \beta_3^2 + 2\rho_1(\beta_1\beta_2 + \beta_2\beta_3 - \beta_1) + 2\rho_2(\beta_1\beta_3 - \beta_2) - 2\rho_3\beta_3)]^{-1}. \tag{A.18}$$

A.4 Fourth order Predictor

The corresponding closed form representation for the 4th order variance is defined as

$$\begin{aligned}\mathcal{D} &\triangleq \mathcal{X} - \mathcal{Y} - \mathcal{Z} - \mathcal{W} - \mathcal{V} \\ &\sim \mathcal{N}(0, \sigma_x^2 + \sigma_y^2 + \sigma_z^2 + \sigma_w^2 + \sigma_v^2 - 2\sigma_{xy} - 2\sigma_{xz} - 2\sigma_{xw} \ , \\ &-2\sigma_{xv} + 2\sigma_{yz} + 2\sigma_{yw} + 2\sigma_{yv} + 2\sigma_{zw} + 2\sigma_{zv} + 2\sigma_{wv})\end{aligned} \tag{A.19}$$

with the according random variables defined according to (3.53)

$$\begin{aligned}&\mathcal{X} \sim \mathcal{N}(0, \sigma_x^2) && \mathcal{Y} \sim \mathcal{N}(0, \sigma_y^2) = \mathcal{N}(0, \beta_1^2\sigma_x^2) \\ &\mathcal{Z} \sim \mathcal{N}(0, \sigma_z^2) = \mathcal{N}(0, \beta_2^2\sigma_x^2) && \mathcal{W} \sim \mathcal{N}(0, \sigma_w^2) = \mathcal{N}(0, \beta_3^2\sigma_x^2) \\ &\mathcal{V} \sim \mathcal{N}(0, \sigma_v^2) = \mathcal{N}(0, \beta_4^2\sigma_x^2).\end{aligned} \tag{A.20}$$

By calculating the weights

$$\begin{bmatrix}\beta[1] \\ \beta[2] \\ \beta[3] \\ \beta[4]\end{bmatrix} = \begin{bmatrix}1 & \rho_{yz} & \rho_{yw} & \rho_{yv} \\ \rho_{yz} & 1 & \rho_{zw} & \rho_{zv} \\ \rho_{yw} & \rho_{zw} & 1 & \rho_{zv} \\ \rho_{yv} & \rho_{zv} & \rho_{wv} & 1\end{bmatrix}^{-1} \begin{bmatrix}\rho_{xy} \\ \rho_{xz} \\ \rho_{xw} \\ \rho_{xv}\end{bmatrix}, \tag{A.21}$$

and the required covariances

$$\begin{aligned}&\sigma_{xy} = \sigma_x\sigma_y\rho_{xy} \quad \sigma_{xz} = \sigma_x\sigma_z\rho_{xz} \quad \sigma_{xw} = \sigma_x\sigma_w\rho_{xw} \quad \sigma_{xv} = \sigma_x\sigma_v\rho_{xv} \quad \sigma_{yz} = \sigma_y\sigma_z\rho_{yz} \\ &\sigma_{yw} = \sigma_y\sigma_w\rho_{yw} \quad \sigma_{yv} = \sigma_y\sigma_v\rho_{yv} \quad \sigma_{zw} = \sigma_z\sigma_w\rho_{zw} \quad \sigma_{zv} = \sigma_z\sigma_v\rho_{zv} \quad \sigma_{wv} = \sigma_w\sigma_v\rho_{wv},\end{aligned} \tag{A.22}$$

the variance σ_{d4}^2 for the 4th prediction error can be calculated from

$$\begin{aligned}\sigma_{d4}^2 = \sigma_x^2(1 + \beta_1^2 + \beta_2^2 + \beta_3^2 + \beta_4^2 + 2\beta_1(\beta_2\rho_{yz} + \beta_3\rho_{yw} + \beta_4\rho_{yv} - \rho_{xy}) + \\ 2\beta_2(\beta_3\rho_{zw} + \beta_4\rho_{zv} - \rho_{xz}) + 2\beta_3(\beta_4\rho_{wv} - \rho xw) - 2\beta_4\rho_{xv}).\end{aligned} \tag{A.23}$$

The above equation simplifies under the assumption ($\rho_{xy} = \rho_{yz} = \rho_{zw} = \rho_{wv} = \rho_1$ and $\rho_{xz} = \rho_{yw} = \rho_{zv} = \rho_2$ and $\rho_{xw} = \rho_{yv} = \rho_3$ and $\rho_{xv} = \rho_4$) to

$$\begin{aligned}\sigma_{d3}^2 = \sigma_x^2(1 + \beta_1^2 + \beta_2^2 + \beta_3^2 + \beta_4^2 + 2\rho_1(\beta_1\beta_2 + \beta_2\beta_3 + \beta_3\beta_4 - \beta_1) + \\ 2\rho_2(\beta_1\beta_3 + \beta_2\beta_4 - \beta_2) + 2\rho_3(\beta_1\beta_4 - \beta_3) - 2\rho_4\beta_4),\end{aligned} \tag{A.24}$$

and a coding gain of

$$\begin{aligned}G_4 = [(1 + \beta_1^2 + \beta_2^2 + \beta_3^2 + \beta_4^2 + 2\rho_1(\beta_1\beta_2 + \beta_2\beta_3 + \beta_3\beta_4 - \beta_1) + \\ 2\rho_2(\beta_1\beta_3 + \beta_2\beta_4 - \beta_2) + 2\rho_3(\beta_1\beta_4 - \beta_3) - 2\rho_4\beta_4)]^{-1}.\end{aligned} \tag{A.25}$$

Bibliography

[1] U. Benz, K. Strodl, and A. Moreira. A comparison of several algorithms for sar raw data compression. *IEEE Transactions on Geoscience and Remote Sensing*, 33(5):1266–1276, 1995.

[2] Ian G Cumming and Frank H Wong. Digital processing of synthetic aperture radar data. *Artech house*, 1(3):108–110, 2005.

[3] John C Curlander and Robert N McDonough. *Synthetic aperture radar*, volume 11. Wiley, New York, 1991.

[4] Charles Elachi. Spaceborne radar remote sensing: applications and techniques. *New York*, 1988.

[5] Giorgio Franceschetti and Riccardo Lanari. *Synthetic aperture radar processing*. CRC press, 2018.

[6] Anthony Freeman. Sar calibration: An overview. *IEEE Transactions on Geoscience and Remote Sensing*, 30(6):1107–1121, 1992.

[7] Nicolas Gebert, Felipe Almeida, and Gerhard Krieger. Advanced multi-channel sar imaging - measured data demonstration. In German Institute of Navigation Deutsche Gesellschaft für Ortun, editor, *International Radar Symposium (IRS)*, International Radar Symposium (IRS) Proceedings, pages 525–529, September 2009.

[8] Nicolas Gebert, Michelangelo Villano, Gerhard Krieger, and Alberto Moreira. Errata: Digital beamforming on receive: Techniques and optimization strategies for high-resolution wide-swath sar imaging. *IEEE Transactions on Aerospace and Electronic Systems*, 49(3):2110–2110, Juli 2013.

[9] Allen Gersho and Robert M Gray. *Vector quantization and signal compression*, volume 159. Springer Science & Business Media, 2012.

[10] Nicola Gollin. Predictive quantization for staggered synthetic aperture radar systems. Master's thesis, University of Trento, Oktober 2018.

[11] Bernhard Grafmueller and Christoph Schaefer. High-resolution synthetic aperture radar device and antenna for one such radar, September 6 2011. US Patent 8,013,778.

[12] Ralf Horn, Anton Nottensteiner, and Rolf Scheiber. F-sar – dlr's advanced airborne sar system onboard do228. In *European Conference on Synthetic Aperture Radar (EUSAR)*, volume 4, pages 195–198. VDE Verlag GmbH, Juni 2008.

[13] Takeshi Ikuma, Mort Naraghi-Pour, and Thomas Lewis. Predictive quantization of range-focused sar raw data. *IEEE Transactions on Geoscience and Remote Sensing*, 50(4):1340–1348, 2012.

[14] N. S. Jayant and Peter Noll. *Digital Coding of Waveforms, Principles and Applications to Speech and Video*, page 688. Prentice-Hall, Englewood Cliffs NJ, USA, 1984. N. S. Jayant: Bell Laboratories; ISBN 0-13-211913-7.

[15] Marc Jäger, Andreas Reigber, and Rolf Scheiber. Accurate consideration of sensor parameters in the calibration and focusing of f-sar data. In *EUSAR 2012; 9th European Conference on Synthetic Aperture Radar*, pages 20–23, 2012.

[16] Gerhard Krieger, Nicolas Gebert, Marwan Younis, Federica Bordoni, Anton Patyuchenko, and Alberto Moreira. Advanced concepts for ultra-wide-swath sar imaging. In *European Conference on Synthetic Aperture Radar (EUSAR)*, volume 2, pages 31–34. VDE, Juni 2008.

[17] Gerhard Krieger, Marwan Younis, Nicolas Gebert, Federica Bordoni, Sigurd Huber, Anton Patyuchenko, and Alberto Moreira. Advanced digital beamforming concepts for high performance synthetic aperture radar (sar) imaging. In *Advanced RF Sensors and Remote Sensing Instruments (ARSI)*, November 2009.

[18] R. Kwok and W.T.K. Johnson. Block adaptive quantization of magellan sar data. *IEEE Transactions on Geoscience and Remote Sensing*, 27(4):375–383, 1989.

[19] D Lancashire, B Barnes, and S Udall. Block adaptive quantization. *3rd Jul*, 2001.

[20] Markus Limbach, Bernd Gabler, Alberto Di Maria, Ralf Horn, and Andreas Reigber. Dlr-compact test range facility. In *European Conference on Antennas and Propagation (EuCAP)*, pages 1–4. Institute of Electrical and Electronics Engineers, März 2012.

[21] E. Magli and G. Olmo. Lossy predictive coding of sar raw data. *IEEE Transactions on Geoscience and Remote Sensing*, 41(5):977–987, 2003.

[22] Michele Martone, Benjamin Bräutigam, and Gerhard Krieger. Quantization effects in tandem-x data. *IEEE Transactions on Geoscience and Remote Sensing*, 53(2):583–597, Februar 2015.

[23] Michele Martone, Nicola Gollin, Michelangelo Villano, Paola Rizzoli, and Gerhard Krieger. Predictive quantization for data volume reduction in staggered sar systems. *IEEE Transactions on Geoscience and Remote Sensing*, pages 1–13, Februar 2020.

[24] J. Max. Quantizing for minimum distortion. *IRE Transactions on Information Theory*, 6(1):7–12, 1960.

[25] Alberto Moreira, Gerhard Krieger, Irena Hajnsek, Konstantinos Papathanassiou, Marwan Younis, Paco Lopez-Dekker, Sigurd Huber, Michelangelo Villano, Matteo Pardini, Michael Eineder, Francesco De Zan, and Alessandro Parizzi. Tandem-l: A highly innovative bistatic sar mission for global observation of dynamic processes on the earth's surface. *IEEE Geoscience and Remote Sensing Magazine*, 3(2):8–23, 2015.

[26] Alberto Moreira, Pau Prats-Iraola, Marwan Younis, Gerhard Krieger, Irena Hajnsek, and Konstantinos Papathanassiou. A tutorial on synthetic aperture radar. *IEEE Geoscience and Remote Sensing Magazine (GRSM)*, 1(1):6–43, März 2013. ©2013 IEEE.

[27] Chris Oliver and Shaun Quegan. *Understanding synthetic aperture radar images*. SciTech Publishing, 2004.

[28] Muriel Pinheiro and Marc Rodriguez-Cassola. Reconstruction methods of missing sar data: analysis in the frame of tandem-x synchronization link. In *European Conference on Synthetic Apeture Radar (EUSAR)*, pages 742–745. IEEE explorer, April 2012.

[29] Mehrdad Soumekh. *Synthetic aperture radar signal processing*, volume 7. New York: Wiley, 1999.

[30] Michelangelo Villano. *Staggered Synthetic Aperture Radar*. PhD thesis, German Aerospace Center, Februar 2016.

[31] Michelangelo Villano, Gerhard Krieger, and Alberto Moreira. Staggered sar: High-resolution wide-swath imaging by continuous pri variation. *IEEE Transactions on Geoscience and Remote Sensing*, 52(7):4462–4479, 2014.

[32] Michelangelo Villano, Gerhard Krieger, and Alberto Moreira. Staggered sar: High-resolution wide-swath imaging by continuous pri variation. *IEEE Transactions on Geoscience and Remote Sensing*, 52(7):4462–4479, Juli 2014.

[33] Rolf Werninghaus and Stefan Buckreuss. The terrasar-x mission and system design. *IEEE Transactions on Geoscience and Remote Sensing*, 48(2):606–614, 2010.

[34] Bernard Widrow and Istvá Kollár. Quantization noise: roundoff error in digital computation, signal processing, control, and communications.(2008), 2008.

[35] Howard A Zebker, John Villasenor, et al. Decorrelation in interferometric radar echoes. *IEEE Transactions on geoscience and remote sensing*, 30(5):950–959, 1992.

[36] Manfred Zink, Gerhard Krieger, and Hauke Fiedler. The tandem-x mission concept. In *Advanced SAR Workshop (ASAR)*, September 2007.